

Microstructure in powders

Spin-echo small-angle neutron scattering measurements

The research described in this thesis was performed at the department of Radiation, Radionuclides & Reactors in the research group: Neutron and Positron Methods in Materials at the Delft University of Technology, Mekelweg 15, 2629 JB Delft, The Netherlands. This work is part of the research programme of the ‘Stichting voor Fundamenteel Onderzoek der Materie (FOM)’, which is financially supported by the ‘Nederlandse Organisatie voor Wetenschappelijk Onderzoek (NWO)’.

Microstructure in powders

Spin-echo small-angle neutron scattering measurements

Proefschrift

ter verkrijging van de graad van doctor
aan de Technische Universiteit Delft,
op gezag van de Rector Magnificus Prof. dr. ir. J.T. Fokkema,
voorzitter van het College voor Promoties,
in het openbaar te verdedigen op dinsdag 9 september 2008 om 10.00 uur

door

Robert Anders ANDERSSON

Master of Science in Chemistry
University of Gothenburg, Sweden
geboren te Askim, Zweden

Dit proefschrift is goedgekeurd door de promotor:

Prof.dr. I.M. de Schepper

Samenstelling promotiecommissie:

Rector Magnificus, voorzitter

Prof.dr. I.M. de Schepper	Technische Universiteit Delft, promotor
Dr. W.G. Bouwman	Technische Universiteit Delft, copromotor
Prof.dr. S. Luding	Universiteit Twente
Prof.dr. A. Schmidt-Ott	Technische Universiteit Delft
Prof.dr.ir. S. van der Zwaag	Technische Universiteit Delft
Dr. M. Blaauw	Technische Universiteit Delft
Dr. D. van der Meer	Universiteit Twente

© 2008 Robert Andersson and IOS Press

All rights reserved. No part of this book may be reproduced, stored in a retrieval system, or transmitted, in any form by any means, without prior permission from the publisher.

ISBN 978-1-58603-906-6

Keywords: Granular Materials, Powders, Microstructure, SANS, SESANS

Published and distributed by IOS Press under the imprint of Delft University Press

Publisher

IOS Press

Nieuwe Hemweg 6b

1013 BG Amsterdam

The Netherlands

tel: +31-20-688 3355, fax: +31-20-687 0019

email: info@iospress.nl

www.iospress.nl

www.dupress.nl

LEGAL NOTICE

The publisher is not responsible for the use which might be made of the following information

PRINTED IN THE NETHERLANDS

Till mamma

Contents

Foreword	3
Introduction	5
1 Analysis of Spin-echo small-angle neutron scattering measurements	23
1.1 Introduction	24
1.2 The density distribution and its autocorrelation, Fourier transform and projection	26
1.3 Basic principle of the SESANS technique	29
1.4 SESANS measured quantities and standard data interpretation	29
1.5 Power-law scattering and the dimensionality of $\rho(r)$	37
1.6 Form factor and the correlation function of isolated shapes	43
1.7 Packings of Hard-Spheres	53
1.8 Oriented anisotropic samples	57
1.9 Grating, oriented periodic beams	60
1.10 Summary and concluding remarks	61
1.11 Acknowledgements	62
2 Stress, strain and bulk microstructure in a cohesive powder	63
2.1 Introduction	64
2.2 Microstructure and SESANS	66
2.3 Experiments and sample properties	68
2.4 Results	70
2.5 Discussion and conclusions	75
3 Structure, anisotropy and fractals in compressed cohesive powders	79
3.1 Introduction	80
3.2 Theory and method	81
3.3 Samples and experiments	89
3.4 Results and discussion	91

3.5	Conclusions	96
3.6	Acknowledgments	98
4	Structure in cohesive powders studied with Spin-Echo Small Angle Neutron Scattering	99
4.1	Introduction	100
4.2	Experiment, the sample and measured quantities	101
4.3	Molecular Dynamics: Method and model	103
4.4	Results	106
4.5	Conclusions	110
	Summary	114
	Sammanfattning	116
	Samenvatting	119
	References	123
	Acknowledgements	130
	About the author	131

Foreword

The men of experiment are like the ant, they only collect and use; the reasoners resemble spiders, who make cobwebs out of their own substance. But the bee takes the middle course: it gathers its material from the flowers of the garden and field, but transforms and digests it by a power of its own
-Francis Bacon.

Powders are poorly understood due to the dissipative nature of the grain-grain interactions. History dependence and non-linearity create plenty of phenomenology and puzzles for the scientists. Although so similar, the knowledge we have about solids, gases and liquids does not seem to capture the physics of powders. In order to explain the macroscopic dynamics of these materials there has to be established relationships between the microscopic nature and macroscopic behaviour of these systems. An important piece in this micro-macro transition are microstructural –real experiments.

The *raison d'être* of an instrument is really established when the instrument is shown to be applicable for the study of nature. Establishing only *how* and *what* it measures should indeed not be motivation enough [24]. A Spin-Echo Small Angle Scattering (SESANS) instrument is capable of studying samples containing large inhomogeneities, large in a sense that they extend across the mesoscopic and microscopic domains. Thus, being applicable to samples of polymers, colloids, dairy products, powders, clays etc. All this in simple and more direct way than existing small angle neutron scattering instruments. In essence, we are confident enough to start exploring the real samples –samples that SESANS is made for.

I believe that the SESANS experiments conducted during my thesis work and presented in this book is capable of bringing insight in the relationship between micro and macroscopics of fine cohesive powders. I also hope to have inspired for future research on samples made up of large disordered heterogeneities in a sense that I discuss many of the correlation functions expected in these systems.

After an introductory text, which serves to introduce the reader to the physics and methods used in greater lines, follows a number of self contained chapters, these are the scientific articles prepared and published during this thesis work.

Introduction

Granular Materials

Imagine taking a piece of rock, shatter it into many smaller pieces, grinding and breaking the rock so much that the graininess finally becomes hidden in the bulk of the material. What type of material does that represent? A practical answer would be a granulated material maybe a powder or just simply –Granular Matter. A strict classification does not seem to exist for what we just made. Although ubiquitous, we lack a physical theory and framework answering the many questions arising about its behaviour. In the end there are the laws of nature governing the system. There is no need for magic but what we need are answers and explanations to the measurable quantities and phenomenologies.

The grain must play a similar role as the molecules and atoms in solids, liquids and gases. We may observe that the powder sits solidly in the form of a pile, flows in a hourglass or blows in the sandstorm. The behaviour of the solid, liquid and gas is seemingly mimicked by granular materials. But it is clear that it is none of these common states, the granular matter is rather a class in its own right.

Clearly, the notion of temperature lacks relevance for the granular material. The relatively large mass of the grains makes the gravitational and kinetic energies exceed the thermal energy by orders of magnitude. When the grains interact they will do that in an irreversible way due to the many internal degrees of freedom contained in the grain. Energy will be dissipated via friction and sound-waves, some grains will be part of force networks and some not, all together making the theories of classical statistical mechanics difficult to apply.

Thus, there is a great deal of fundamental challenges for the study of these materials. Granular materials seem to share many of the properties of other non-equilibrium systems such as gels and glassy systems. The macroscopic nature of the granular media makes it an easy accessible model-system both computationally and experimentally. Usually one chooses N -identical spherical beads as the model system. Easily bought and computationally convenient.

A set of tapping experiments on such samples was conducted in Chicago

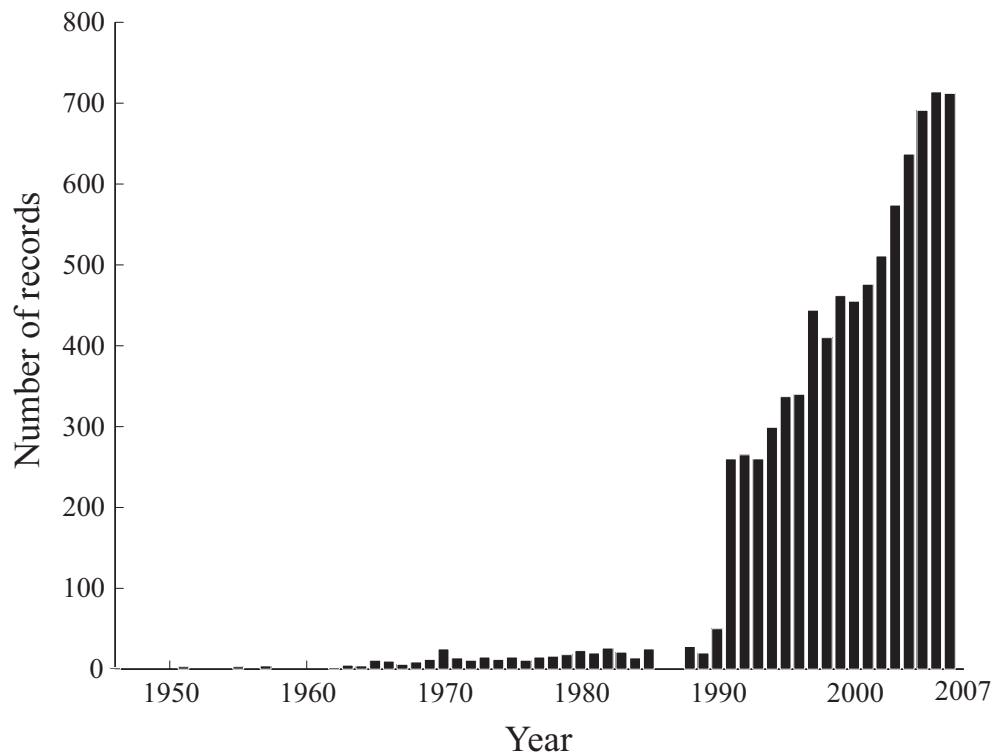


Figure 1: Number of records (scientific publications) found by Web of Science when conducting a boolean search that finds the word ‘Granular’ together with either ‘Material(s)’ or ‘Matter’ in the topic of articles. Searching by topic means a search in the abstract, title, and keyword fields of a record.

[57, 56, 42], in the years 1995-1997. The authors noted that there is a so called “reversible branch” on the sphere packing fraction versus tapping acceleration curve. In essence this experiment showed that the granular matter (depending on initial conditions) can exist in a reversible steady state. This observation makes a statistical mechanics approach more realistic. In fact, these experiments were inspired by such a statistical mechanics approach proposed by theoretical work [22] published in 1989 by Edwards *et.al*. These experiments and the theoretical work inspired scientists and physicists in particular to conduct research in the framework of granular materials, and the area saw a boom in interest, see Fig. 1.

Fig. 1 is an analysis of the number of records found by Web of Science based on a search that finds the word ‘Granular’ together with either ‘Material(s)’ or ‘Matter’ in the topic (abstract, title and keywords) of articles. The number of records found is plotted as a function of year. Note the increase of publications around the time of [22] 1989 and [42] 1995.

The ultimate goal for the physicist dealing with granular media is to find a continuum mechanics description that satisfactory explains the macroscopical

mechanical response of the material, i.e., being able to relating force and motion. For this to be achieved the physicist has to link the microscopic –grain-level statistics and dynamics to the macroscopic behaviour. The creation of such theory and model would ultimately lead to better understanding about natural phenomena such as avalanches, landslides, earthquakes and erosion in general, better engineered dams and dykes and more effective handling of particulate materials in industry. This thesis deals with experimental work on the bulk microstructure of fine powders.

Cohesive Granular Materials (Powders)

Further processing and grinding our rock discussed in the previous section creates finer granular material made up of smaller particles. The grains are barely contrasted and there is now the notion of a powder or –cohesive granular materials. In essence the idea of inter-grain cohesion in powders is a matter of size. The interactions between the grains in a non-cohesive granular material are mainly driven by friction and the hard core exclusion between constituent grains. There are no long range forces and no attractive forces in the dry classical granular material, and if they would be present they would be irrelevant as compared to body forces acting on these large grains.

In nature one finds the action of van der Waals interaction induced by fluctuating dipoles acting between neighbouring molecules. It is possible to sum all these interactions between the individual molecules [32] so that the interaction can be generalised to mesoscopic and macroscopic objects. The attractive van der Waals force between two identical spherical grains can be approximated with:

$$F_{vdW} \simeq \frac{hD}{6\sigma^2} \quad (1)$$

Here D is the sphere diameter, σ is the distance separating the two spheres and h is the so called Hamaker constant, which is in the order of 10^{-20} to 10^{-19} J depending on the chemistry making up the grain. We remind ourselves that the force due to gravity acting on a sphere is given by:

$$F_{grav} = \frac{\pi D^3 \rho g}{6}, \quad (2)$$

where ρ is the density and g is the earth's gravitational acceleration.

Capillary force is another origin for adhesion among grains. Capillary forces arise due to the overlap between the liquid meniscus surrounding two particles. The strength of this interaction depends on the curvature and the surface tension,

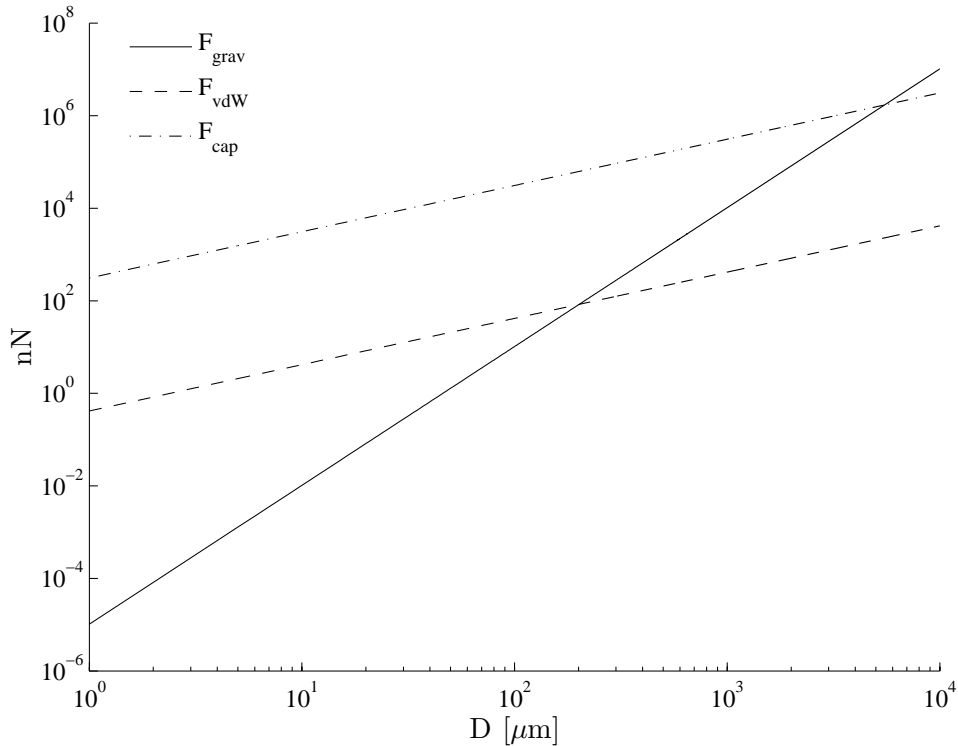


Figure 2: The solid line is the force due to gravity F_{grav} acting on a sphere plotted versus the sphere diameter. The dashed line is the van der Waals force F_{vdW} acting between two spheres separated a distance $\sigma=10\text{\AA}$ and characterised by a Hamaker constant $h = 10^{-20}\text{J}$. Finally, on the dot-dashed line we plot the capillary force acting between two wet spheres.

it is a fairly difficult task to accurately calculate this force, but an approximation could at least give us the order of magnitude:

$$F_{cap} \simeq 2\pi\Gamma D \cos(\vartheta) \quad (3)$$

where Γ is the surface tension of the gas-liquid interface and ϑ is the wetting angle.

Using these three expressions (Eq. (1), Eq. (2) and Eq. (3)) for forces acting on a grain makes it possible to set up a very simple calculation that relates the force acting on a grain to the size of the grain. By doing so we will obtain some orders of magnitude defining the physics regarding powders and granular matter. Fig. 2 shows the plots of the van der Waals force, gravity force, and capillary force acting on or between spherical grains versus the grain diameter.

In terms of the grain size, we see that there is a cross over between two domains, one for small particles where mutual van der Waals attraction between grains dominates over gravity and a second domain for larger grains, say $>200\mu\text{m}$, where gravity dominates. Thus, a powder becomes cohesive when the grain size

is below a few hundred microns. In Fig. 2 we show that the interaction between grains due to humidity induced capillary forces can be major up to millimeter sized grains (we use this when we build sand castles). For this calculation we used a surface tension Γ of 70mN and a wetting angle ϑ of 45 degrees.

Adhesive forces between grains in a powder may lead to difficulties in many industrial applications. Attractive forces create stable aggregates, channels, voids and arches which all leads to unstable mass flows in silos or bubbling fluidised beds [76]. Mining, pharmaceutical and chemical industries (just to name a few) are examples of industries that handle fine particulate materials on a large scale. The powder is either a raw material, byproduct or the desired end product. The demand for even finer granular materials is increasing due to market demands for nanostructured materials in pharmaceutical and electronic industries. The significance of adhesive forces for the macroscopic behaviour is illustrated in In Fig. 3. The top figure shows a powder made up of silica grains of $5\mu\text{m}$ in diameter. The bottom figure shows an assembly of spherical beads of 1mm in diameter that has been slightly wetted by adding water. Clearly, the action of adhesive forces can stabilise large clusters of particles.

Microstructure in granular materials: Correlation functions

As we have seen, there are both fundamental and applied reasons motivating the buildup of models and theory explaining the properties of powders and granular materials. The computer makes it possible to study many-particle systems using Monte-Carlo, molecular dynamics and similar approaches [61]. Such simulations give a complete insight in the relationship between grain scale properties and the macroscopic properties. Model building, simulations and theory development need the support and challenge from experimental observations. This calls for real experiments and observations on the grain level.

The grains making up a 3D granular material tend to organise themselves in a random fashion and, therefore, it is mainly the problem of random sphere-packing [7] that has been addressed. In particular, it is the structure in terms of the pair correlation function $g_2(r)$ (giving the probability of finding a neighbouring centre of mass next to another one) that is being studied. It is appropriate to give $g_2(r)$ some extra attention here, since it is a measurable quantity [5] and [4].

The pair correlation function is related to the inter particle interactions. For the hard-sphere case one observes clear transitions between gas/liquid/glass/crystal states in the form of excluded volume correlations and ordering. Concerning granular materials it is usually the topic of jamming that is studied, both by means of



Figure 3: Pictures illustrating the significance of adhesive forces among grains. The top figure shows a silica (SiO_2) powder containing primary grains of about $5\mu\text{m}$. The bottom picture shows a packing of spherical silica beads of 1mm in diameter. A small amount of water was added to create capillary forces among the beads. (the two pictures have the same scale)

computer simulations and experiments. Dense configurations of spheres are said to be jammed when all spheres are connected so that no more displacements are possible, precluding further exploration of phase space. Interestingly this seems to happen around a well defined sphere packing fraction $\phi_J \simeq 0.64$ (far from the maximum, but also jammed, sphere packing fraction of 0.74). Recall that

$$\phi = \frac{v}{V}, \quad (4)$$

where v is the volume taken up by a granular phase (the fraction of voids is $1-\phi$) contained in the volume V . The pair correlation function is for N number of spheres in a volume V

$$g_2(r) = \frac{V}{N^2 4\pi r^2} \left\langle \sum_{i=1}^{N-1} \sum_{j=i+1}^N \delta(r - r_{ij}) \right\rangle \quad (5)$$

Measurements (or simulation results) of the pair correlation function for packings of athermal identical spheres do not reveal any crystal ordering. That the structure appears to be in a frozen liquid like state, the structure is said to be jammed or in a glassy state. It is usually assumed that the packings are translational invariant (i.e., statistically homogeneous) and rotational invariant (i.e., isotropic). The pair correlation is therefor a spherical average over all the particles contained within some volume.

The pair correlation function $g_2(r)$ can easily be calculated numerically, provided that the centre of mass coordinates of the particles are known.

For a packing of hard spheres with diameter D this function will be zero for $r < D$, due to the impenetrability of hard spheres, and unity for $r \rightarrow \infty$, provided that there are no long range order (i.e., crystals). A peak will be present at $r = D$, this is the nearest neighbour peak, which will be followed by, special for jammed hard sphere packings, a split second peak at $\sqrt{3}D$ and $2D$. This split second peak in $g(r)$ is seen as a typical marker for the jamming transition. Fig. 4 shows the pair correlation function for one of the sphere packings reported in [5] and [4]. The 3D density distribution and the center of mass coordinates of the spheres was determined by a X-ray tomography experiment and the data was kindly provided by the authors. The packing fraction in this example is 0.64.

The pair correlation function is in principle accessible experimentally in, for example, wave diffraction experiments [23] and as have been seen from a tomographic scan. In order to extract $g_2(r)$ from a measurement one needs a model or a measurement that describes the structure of the isolated particle (i.e., the density distribution $\rho(r)$ surrounding its centre of mass), see Fig. 5 for some examples of density distributions. The density distribution contains all the information about

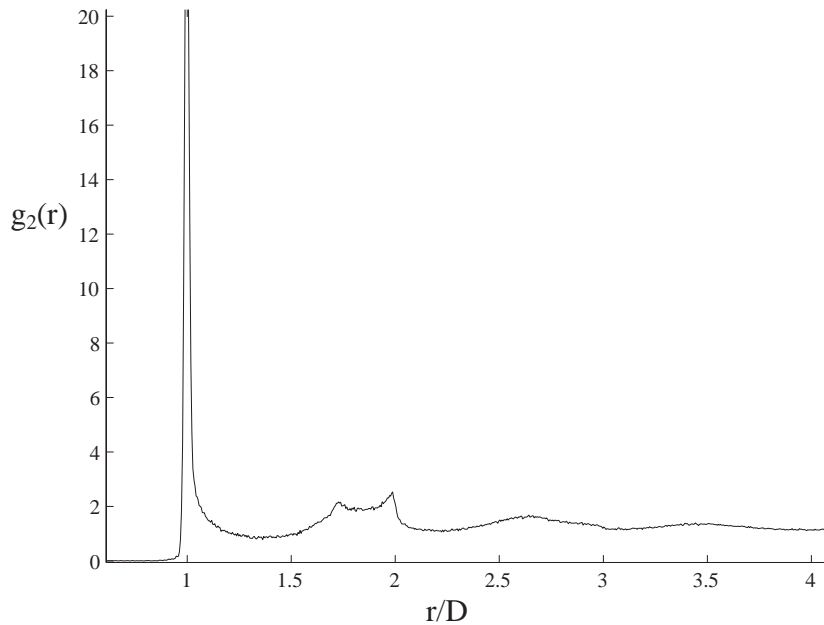


Figure 4: The pair correlation function $g_2(r)$ for a random packing of spheres. The packing fraction is here 0.64. The data (center of mass coordinates) was determined by a X-ray tomography experiment and kindly provided for this calculation by the authors of [5] and [4]

the structure of the material. Considering a phase i in a material, the density distribution can be (assuming an isotropic distribution)

$$\rho(\mathbf{r}) = \begin{cases} 1 & \text{if } \mathbf{r} \text{ is inside a grain,} \\ 0 & \text{if } \mathbf{r} \text{ is outside.} \end{cases} \quad (6)$$

The packing fraction of the grain phase is

$$\phi = \frac{1}{V} \int_V \rho(\mathbf{r}) d\mathbf{r} \quad (7)$$

so that $0 < \phi < 1$. The autocorrelation function of the density fluctuations for a two phase system becomes

$$\gamma(\mathbf{r}) = \frac{\int \Delta\rho(\mathbf{r}') \Delta\rho(\mathbf{r}' + \mathbf{r}) d\mathbf{r}'}{\phi(1 - \phi)}, \quad (8)$$

where $\Delta\rho(\mathbf{r}) = \rho(\mathbf{r}) - \phi$. $\gamma(\mathbf{r})$ gives the probability of observing the same density when looking at a position $(\mathbf{r}' + \mathbf{r})$ away from a point \mathbf{r}' in the density distribution. If the density distribution is isotropic, then the correlation function depends only on the modulus or \mathbf{r} and the angular and volume averaged correlation function is in short notation

$$\gamma(r) = \langle \Delta\rho(0) \Delta\rho(r) \rangle_V, \quad (9)$$

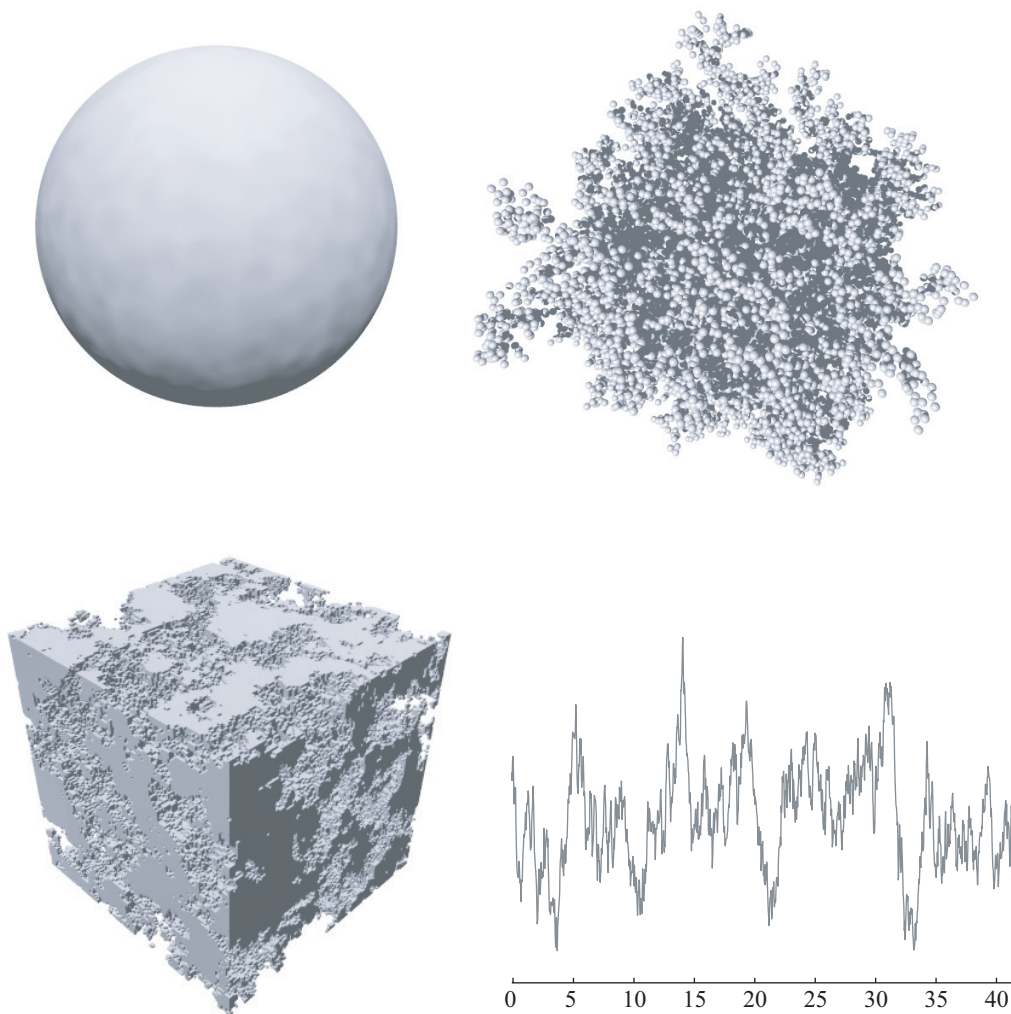


Figure 5: Examples of real-space density distributions. Clockwise from top left we have: Sphere, Diffusion Limited Aggregate, A random media and finally a 1D random graph.

where $\gamma(0) = 1$. A conceptual way of interpreting $\gamma(\mathbf{r})$ is that it corresponds to the average shared volume of the density and a copy of the density after shifting the copy some distance.

$\gamma(\mathbf{r})$ is in a sense the pair correlation function calculated from all points in the density distribution, rather than just the particle centre of masses. The autocorrelation function of the density distribution can be measured. A few examples of density distributions are shown in Fig. 5. For a single sphere the autocorrelation function is known analytically, but for the other cases it becomes necessary to calculate the correlation function numerically.

If one would cut out cross sections at random through a material, then one would find that the degree of independence between such sections depends on

the distance separating them; at certain distances the sections will be similar (correlated) and at others not. For disordered materials, like liquids, gases, powder materials etc. a certain degree of correlation is found within the correlation length of the material, i.e., $\gamma(r)$ is unity at $r = 0$ and decays depending on the density correlations. At some distance one would find that the cross sections are wholly independent, thus no correlations are expected and $\gamma(\infty) = 0$

The correlation length ξ of the density distribution is a size which is characteristic, and as will be seen also measurable, of the sample structure

$$\xi = \int_{-\infty}^{\infty} \gamma(r) dr. \quad (10)$$

Rather than decomposing the material into grains, pores, particles etc of certain size, this characteristic size offers a more general structural parameter in defining the size of a microstructure.

In this thesis it is the projection of $\gamma(r)$ that is of interest. It is the projection that is measured in a spin-echo small angle neutron scattering (SESANS) experiment. The projection along x in cartesian coordinates becomes

$$G(z) = \frac{2}{\xi} \int_0^{\infty} \gamma(x, 0, z) dx. \quad (11)$$

If $r = \sqrt{z^2 + x^2}$ and we substitute $x = \sqrt{r^2 - z^2}$ so that $dx = r(r^2 - z^2)^{-1/2}$ then we have that

$$G(z) = \frac{2}{\xi} \int_z^{\infty} \frac{r\gamma(r)}{\sqrt{r^2 - z^2}} dr, \quad (12)$$

where the prime denotes differentiation. The inverse transformation reads

$$\gamma(r) = -\frac{1}{\pi} \int_r^{\infty} \frac{G'(z)}{\sqrt{z^2 - r^2}} dz, \quad (13)$$

which is known as the Abel transformation [14] of circular symmetric functions.

Fig. 6 gives an idea of the relationship between the density distribution $\Delta\rho(x, y, z)$ (ray-traced top), its autocorrelation function $\gamma(r)$ (bottom left) and the projection $G(z)$ (bottom to the right). The calculations are based on the two distributions, the sphere and a star like geometry, shown on the top of the figure. More density distributions and their correlation functions are discussed in Chapter 1.

Wave diffraction and microstructure

The interference of waves that are scattered by an object is called diffraction. If the scattered waves are coherent then the measured intensity is found as the absolute square of the sum of the amplitudes. A neutron interacts with the nucleus

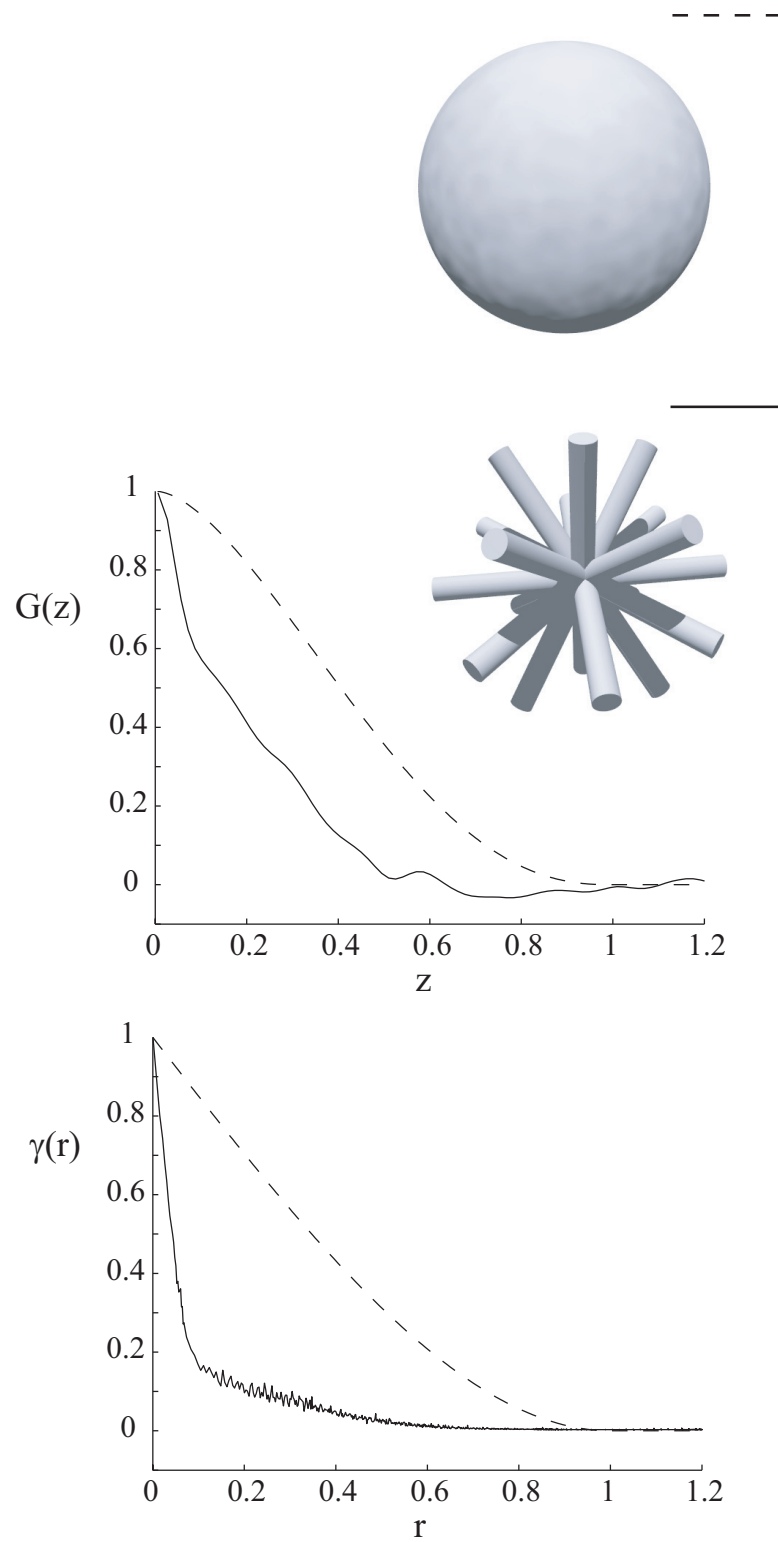


Figure 6: The autocorrelation function $\gamma(r)$ (left figure) and $G(z)$ (figure to the right) for a sphere (dashed line) and the *star* geometry (solid line)

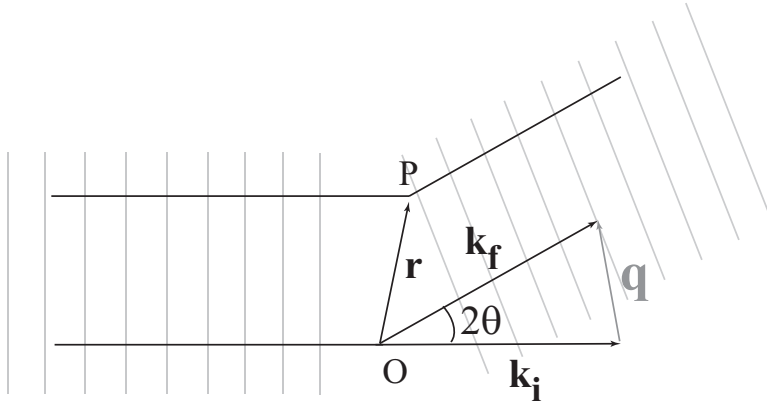


Figure 7: The geometry of scattering of waves. The wave, with incoming wave vector magnitude $k_i = 2\pi/\lambda$, scatters at an angle θ . The magnitude of the final wave vector is for elastic scattering $k_f = k_i$. The momentum transfer $\mathbf{q} = |\mathbf{k}_i - \mathbf{k}_f|$ is related to the scattered angle by $q = 4\pi\lambda^{-1} \sin(\theta)$.

of an element (the nuclei becomes the source of the secondary scattered waves). The scattered wave is expressed by the complex function $e^{i\eta}$, with η being the phase (i.e., the optical path difference between a point and a reference multiplied by the magnitude of the wave vector $k = 2\pi/\lambda$, where λ is the wavelength).

Considering Fig. 7, the path difference of Point P , given by vector \mathbf{r} , w.r.t. the origin O is $-\mathbf{r}(\mathbf{k}_f - \mathbf{k}_i)$. The scattering is taken to be elastic, meaning that the magnitude of the wave vector is unchanged, i.e., $k_f = k_i = 2\pi/\lambda$. The phase is expressed in terms of momentum transfer, so that $\eta = -\mathbf{q}\mathbf{r}$, where $\mathbf{q} = |\mathbf{k}_i - \mathbf{k}_f|$ is the momentum transfer. The magnitude of \mathbf{q} is

$$q = |k_i - k_f| = \frac{4\pi}{\lambda} \sin(\theta). \quad (14)$$

The resulting amplitude is, as mentioned, found by adding up all the secondary waves emerging from all the nuclei in the irradiated sample. The sum is written as an integral over the irradiated volume V

$$A(\mathbf{q}) = \int_V e^{-i\mathbf{q}\mathbf{r}} \Delta\rho_s(\mathbf{r}) d^3\mathbf{r}, \quad (15)$$

which is the mathematical operation of Fourier transformation [14]. In other words, the neutron interacts with a distribution of scatterers given by $\Delta\rho_s(\mathbf{r})$. $\Delta\rho_s(\mathbf{r})$ is the scattering length density (SLD) distribution of the object, thus the amplitude of the scattered waves is the Fourier image of the SLD distribution of the material. It is, however, the intensity that can be measured in an experiment. Multiplication with the complex conjugate A^* yields the so called differential scattering cross section

$$\frac{d\Sigma}{d\Omega}(\mathbf{q}) = AA^* = \int_{V_1} d^3\mathbf{r}_1 \int_{V_2} e^{-i\mathbf{q}(\mathbf{r}_1 - \mathbf{r}_2)} \Delta\rho_s(\mathbf{r}_1) \Delta\rho_s(\mathbf{r}_2) d^3\mathbf{r}_2. \quad (16)$$

Thus, this Fourier transformation is an integral over all pair of points in the irradiated volume. First an integral is calculated over the pairs of points that have equal relative distances, yielding after dividing with the volume V

$$S_s(\mathbf{r}) = \frac{1}{V} \int \Delta\rho_s(\mathbf{r}_1)\Delta\rho_s(\mathbf{r}_2)dV, \quad (17)$$

being is the autocorrelation function of the SLD distribution of the sample. Expressing the $d\Sigma/d\Omega(\mathbf{q})$ in terms of $S_s(\mathbf{r})$ gives

$$\frac{d\Sigma}{d\Omega}(\mathbf{q}) = \int e^{-i\mathbf{q}\mathbf{r}} S_s(\mathbf{r})d^3\mathbf{r}. \quad (18)$$

The inverse Fourier transformation is

$$S_s(\mathbf{r}) = (2\pi)^{-3} \int_V e^{i\mathbf{q}\mathbf{r}} \frac{d\Sigma}{d\Omega}(\mathbf{q})d^3\mathbf{q}. \quad (19)$$

For a two phase isotropic material we have that

$$S_s(r) = (\Delta\rho_0)^2\phi(1 - \phi)\gamma(r), \quad (20)$$

Thus, it can be said that the measured intensity in a scattering experiment is the Fourier transformation of the autocorrelation function $\gamma(r)$ of density distribution Eq. (17). $\Delta\rho_0$ is the difference in scattering length density between two phases ($\Delta\rho_0 = \rho_1 - \rho_2$).

The unit of $d\Sigma/d\Omega(q)$ is m^{-1} and the scattering length density $\Delta\rho_s$ has the dimension of m^{-2} so that $S_s(r)$ is in m^{-4} .

Small-angle neutron scattering

Distances in real and reciprocal space are mutually inverse, meaning that scattering from larger inhomogeneities will result in a scattering at low- q (small angles). The obvious way to technically enable the detection of such pattern is to create a narrow beam of neutrons that impinges on a sample and then detect the scattering at some 2D position sensitive detector far away from the sample. This is a so called pinhole SANS instrument [23] and [29] (see Fig. 8).

The small angle scattering can be expressed as a normalised probability distribution, with $q_x = 0$ for small angle scattering

$$\Sigma(q_y, q_z) = \frac{\frac{d\Sigma}{d\Omega}(q_y, q_z)}{\int \int \frac{d\Sigma}{d\Omega}(q_y, q_z)dq_y dq_z}, \quad (21)$$

so that

$$\int \int \Sigma(q_y, q_z)dq_y dq_z = 1. \quad (22)$$

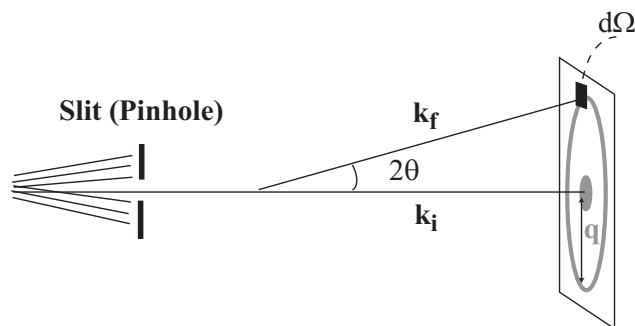


Figure 8: Principle of a small-angle neutron scattering instrument. The resolution of the instrument at the 2D detector will depend on the angular spread of the incoming beam. A slit creates a narrow pinhole beam so that the scattered intensities can be measured as a function of momentum transfer \mathbf{q} .

Note that

$$\frac{d\Sigma}{d\Omega}(q_y, q_z) = \int \int e^{-i(q_y y + q_z z)} \hat{S}_s(y, z) dy dz, \quad (23)$$

where the projection can be written as

$$\hat{S}_s(z) = \int S_s(x, 0, z) dx = (\Delta\rho_0)^2 \phi(1 - \phi) \xi G(z). \quad (24)$$

A SANS instrument measures the differential scattering cross section $d\Sigma/d\Omega(q_y, q_z)$, related to the sample structure according to Eq. (18) and Eq. (19).

Spin-echo small angle neutron scattering

The pinhole procedure creates an inverse relationship between q -resolution and measured intensity (a neutron beam is collimated by cutting out a section of the beam using slits). The resolution of such instrument is in the order of a few nanometer up to a few hundred in terms of real-space range.

The pinhole can, however, be made obsolete by using so called spin-echo techniques [54]. Neutrons undergo a Larmor precession in magnetic fields. The precession is expressed in terms of an angle

$$\varphi = c\lambda BL, \quad (25)$$

where B is the magnetic field, L is the path length through the field and the Larmor constant is $c = 4.6368 \times 10^{14} \text{T}^{-1} \text{m}^{-2}$. If the face of the magnetic field region is inclined, forming a parallelogram shaped region (see Fig. 9), then

$$\varphi_1 \simeq c\lambda BL(1 - \alpha \cot \theta_0), \quad (26)$$

where θ_0 is related to the inclination angle of the field region and α is the neutron transmission angle with the x -axis (see Fig. 9). Note that the path-length travelled for a un-scattered neutron will be the same in the two field regions.

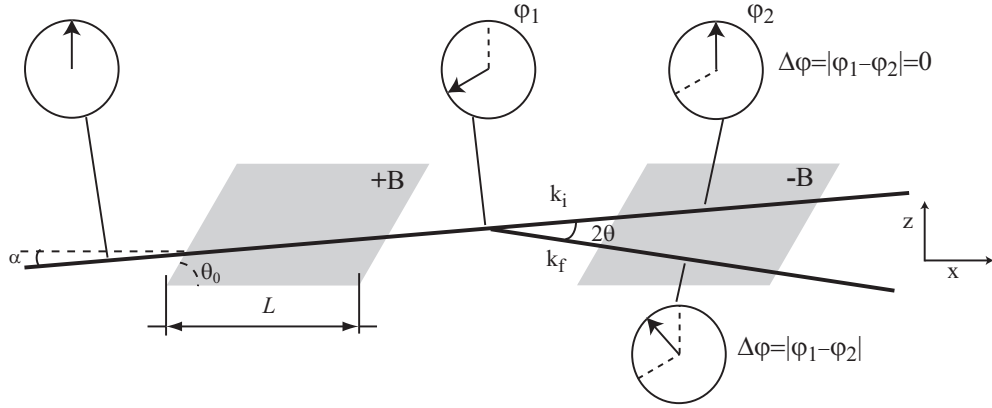


Figure 9: Principle of the spin-echo small angle neutron scattering instrument. Two parallelogram shaped magnetic field regions, with tilt angle θ_0 , form a symmetric setup around the sample position. The regions have opposite magnetic fields $B+$ and $B-$ meaning that the neutron is precessing in opposite directions in the two fields (φ_1 and φ_2). The incoming neutron enters the first field with an angle α and scatters by an angle 2θ from \mathbf{k}_i to \mathbf{k}_f at the sample position. The scattering leads to a net precession $\Delta\varphi$ due to the different path-lengths travelled in the second magnetic field.

Using polarised neutrons and combining two such field regions, but having one with opposite direction of the field, produces a spin-echo setup (the precession in the first field region is compensated/echoed in the second the precession). If there is no scattering then the net precession angle is $\Delta\varphi = \varphi_1 - \varphi_2 = 0$. If there is scattering then the symmetry is broken, giving rise to net precession due to the different path length in the last field region. The net-precession of a neutron scattered over a vertical angle θ is

$$\Delta\varphi = \varphi_1 - \varphi_2 \simeq c\lambda BL\theta \cot\theta_0, \quad (27)$$

In this way, the setup is said to encode the scattered angles.

Using Eq. (14) we can express the net precession in terms of the z -component momentum transfer q .

$$\Delta\varphi \simeq B \frac{c\lambda^2 L \cot(\theta_0)}{2\pi} q_z = q_z z, \quad (28)$$

where $q_z \simeq 4\pi\theta/\lambda$ for small angles. The spin-echo length z is defined as

$$z \equiv B \frac{c\lambda^2 L}{2\pi} \cot(\theta_0), \quad (29)$$

and has the dimension of length. The physical origin of z being a length can be understood from the quantum mechanical treatment of Larmor precession, where the two eigenstates of the neutron are separated over z in the field region [24] and [10].

The net precession cannot be measured directly, but is related to the polarisation of the neutron beam after the last field, i.e.,

$$P(q_z, z) = \cos(\Delta\varphi) = \cos(q_z z). \quad (30)$$

The spin-echo length z is varied by changing the magnetic field B according to Eq. (29). Thus, no scattering results in $P = \cos(0) = 1$ and in the case of scattering $P < 1$.

If there is a sample (a distribution of scatterers) present between the two field regions, then the measured polarisation will be the weighted sum of the polarisation of the scattered and un-scattered neutrons. Thus,

$$P(z) = (1 - \Sigma_t) + \Sigma_t \int \int \cos(q_z z) \Sigma(q_y, q_z) dq_y dq_z, \quad (31)$$

where the first term is the contribution from the un-scattered neutrons and the second term is the polarisation for the scattered part. Σ_t is the fraction of neutron that scatters once. Since $\Sigma(q_y, q_z)$ is real valued and even, we find that the polarisation of the neutron beam in the case of single scattering is [63]

$$P(z) = (1 - \Sigma_t) + \Sigma_t \int \int e^{i(q_y y + q_z z)} \Sigma(q_y, q_z) dq_y dq_z = (1 - \Sigma_t) + \Sigma_t G(z), \quad (32)$$

where $G(z)$ is the projection of $\gamma(r)$. Taking into account multiple scattering it can be shown that [65]

$$P(z) = e^{\Sigma_t(G(z)-1)}. \quad (33)$$

For a sample with thickness t

$$\Sigma_t = \lambda^2 t (\Delta\rho_0)^2 \phi(1 - \phi)\xi. \quad (34)$$

This shows that a SESANS measurement relates the measured polarisation of a neutron beam to the projection $G(z)$ of the autocorrelation function $\gamma(r)$ of the sample. SESANS can probe correlations in the range $20\text{nm} < z < 20\mu\text{m}$ without a significant need for beam collimation and multiple scattering is easily accounted for.

Technical details and experimental conditions

The setup is shown together with a schematic drawing of the key components in Fig. 10. A set of six pyrolytic graphite monochromators focuses a beam with a wavelength of $0.21\text{nm} \pm 1\%$ on the sample position. The beam is first polarised by a set of supermirrors (reflecting one spin state) and a similar set at the end of the

set-up acts as an polarisation analyser before the ^3He detector used for counting the neutrons. The polarisation P is found as

$$P = \frac{I_+ - I_-}{I_+ + I_-}, \quad (35)$$

where I_+ is the spin up intensity and I_- is the down intensity detected by the detector.

Two sets of slits, one after the polariser and one before the analyser, define the dimensions of the incoming and outgoing beam. The size of the beam is in the order of cm^2 . Four electromagnets are positioned on an aluminium table to avoid disturbance of the surroundings of the neutron path. The sign of the magnetic field changes from the second to third magnet and for this purpose a field stepper is installed just before the sample position. The field stepper makes a sharp transition between the two field regions. Samples are mounted on a translation stage capable of moving the sample in and out of the beam. The magnetic fields are set and controlled to values between 0.5 and $230 \times \text{mT}$. A key component in the set-up are the $3 \mu\text{m}$ thick perm alloy films deposited on silicon wafers placed between the pole faces of the electromagnets (see Fig. 10). The foils make the neutron spin undergo a π -flip, all together creating two parallelogram shaped precession regions. The foils are positioned with an angle of 5.5° to the central axis of the neutron beam in the centre of the electromagnets.

A measurement takes from a few hours up to days depending on the desired statistical accuracy of the measurement (the error is proportional to the square root of the neutron counts). The typical size of a sample is in the order of cm^2 and a few mm to a few cm:s thick along the beam, a good value for Σ_t in Eq. (34) would be about 0.1-1.

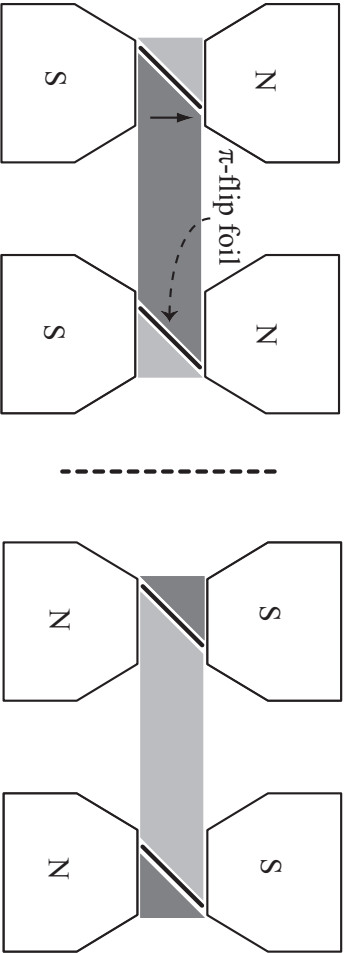
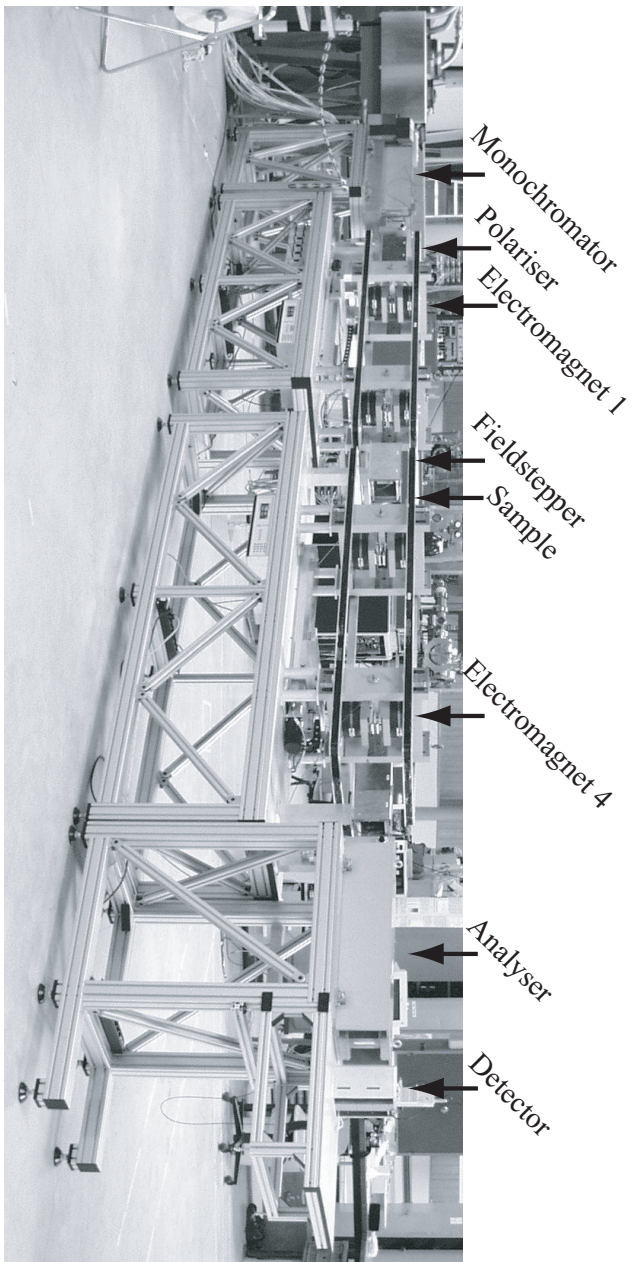


Figure 10: Picture of the SESANS setup at the Reactor Institute in Delft. The main components of the setup are pointed out in the picture. The bottom figure show schematically the realisation of the parallelogram shaped magnetic field regions. The grayscale shaded areas indicates the field direction with respect to the neutron spin orientation. The magnetised foil makes the neutron undergo a π -flip

Chapter 1

Analysis of Spin-echo small-angle neutron scattering measurements

This article, By Robert Andersson, Leon F. van Heijkamp, Ignatz M. de Schepper and Wim G. Bouwman, has been 'accepted if revised' for publication by the scientific journal: Journal of Applied Crystallography.

Abstract

Spin-echo small-angle neutron scattering (SESANS) is, in contrast to conventional small-angle neutron scattering (SANS), a real-space technique. SESANS measures the projection of the density-density correlation function of a sample, rather than, as in SANS, its Fourier transform. This paper introduces a toolkit for how to interpret and analyse a SESANS measurement. Models that are used in SANS are discussed and translated into a SESANS formalism. These models can be used to analyse and fit the data obtained by SESANS. Dilute, concentrated, random, fractal and anisotropic density distributions are considered. Numerical methods used to calculate the projection from numerical data are presented, either using Fourier transformation or via the real-space pair correlation function.

1.1 Introduction

Small-angle x-ray scattering or Small-angle neutron scattering neutrons (SANS), was developed in order to enable investigations of the bulk microstructure of samples. Samples that are characterised by heterogeneities ranging between tens of nanometers up to several hundred nanometers [23]. A conventional SANS instrument measures the intensities of neutrons scattered into the solid angles of a detector positioned far away from the sample. The scattered intensities measured in a SANS experiment are therefore proportional to the Fourier transform $I(q)$ of the autocorrelation function $\gamma(r)$ of the samples density distribution $\rho(r)$. Since distances in real and Fourier space are mutually inverse this approach makes it necessary to collimate the beam. Beam collimation creates an inverse relationship between angular (momentum, q) resolution and measured intensities. Ultra small-angle neutron scattering (USANS) increases the resolution by orders of magnitude so that micrometer length scales become accessible. For a recent review on SANS and USANS and its applications see [53] and on the data analysis see [58].

Spin-echo small-angle neutron scattering (SESANS) was developed in order to circumvent the need for beam collimation and therefore enable investigations of samples containing structures ranging from the nano up to the micrometer domain. The technical details and theoretical framework needed to realise this development can be found in [66] and its applications in [9]. The SESANS approach relates the polarisation $P(z)$ of the neutron beam to the projection $G(z)$ of the autocorrelation function $\gamma(r)$ of the samples density distribution $\rho(r)$. The polarisation is in a SESANS experiment measured as a function of the spin-echo length. The spin-echo length is the real-space distance over which correlations are measured in the sample. SESANS and its measured quantities can be understood from a wavenumber perspective [80], and in this context the instrument is performing a 2D Fourier transform of the scattered intensities. The SESANS measurement can also be formulated in real-space, both physically [24], [10] and mathematically [45], meaning that SESANS measures the projection of $\gamma(r)$ along the neutron beam path. The integral transformation producing $G(z)$ is called the Abel transformation of $\gamma(r)$. The inverse Abel transform is unique for an isotropic distribution.

An advantage, considering the data analysis of a SESANS measurement, is that multiple scattering effects are easily accounted for [65]. Therefore, SESANS enables measurements on strongly scattering and thicker samples, which is typically the case in the sample-domain of interest. In SANS/USANS, on the other hand, multiple scattering makes the data analysis more involved, see [83] and [68]. The amount of scattering is therefore often reduced by manipulating the sample (dilution, making it thinner, contrast matching etc). The application of SESANS to samples are found throughout a wide range of domains, such as model colloids for fundamental studies [45], fine granular and powder materials [2], food materials [79] and other complex colloidal suspensions, cements and clays, just to name a few areas.

More SESANS-type instruments are being constructed and planned throughout the neutron scattering community, see [60], [62]. Such instruments will be accessible by a more general user community. These developments make it necessary to develop a framework for how to interpret, analyse and model such experiments. This paper introduces such a toolkit that can be used for the analysis of a SESANS experiment.

The first data analysis of a measurement can be done by looking at the raw data by eye. Some rules of thumb together with model free methods will be presented. Model free parameters that can be extracted from a SANS measurement often have SESANS counterparts, such parameters will be discussed. The methods developed by Debye and Porod as well as Guinier's law for the analysis of small-angle scattering will be discussed, and the analogous SESANS formalisms are discussed. This paper translates many of the so called form factors, describing spheres, cylinders, spheroids etc. Some theoretical and model distributions are shown to highlight the applicability of SESANS for the study of anisotropic density distributions.

If the autocorrelation function $\gamma(r)$ of the distribution is known, then the SESANS counterpart is found through the projection of the autocorrelation function. On the other hand, when no analytical functions exists for $\gamma(r)$ it becomes necessary to do numerical calculations. A method for performing such calculations and examples are given. Dense but disordered structures can often be described by relatively simple formalisms and phenomenological correlation functions. Scale invariant, or fractal, distributions yield power laws in both real $\gamma(r)$ and reciprocal space $I(q)$, and it is shown how such distributions would manifest in a SESANS experiment. Models that describe random and self-affine distributions have been proven excellent at modelling many disordered two phase materials [2]. A corresponding SESANS formalism has been developed and some new functions are proposed. Denser monodisperse sphere-packings show, due to the excluded-volume, ordering and therefore oscillations in the correlation function. In SANS one usually separates the measured spectrum into a form-factor, describing intra-particle correlations, and a structure-factor originating from inter-particle correlations. A similar approach can be used for SESANS. The Percus Yevick approximation [59], [74] has been used to calculate the correlation function for hard sphere liquids in order to highlight how ordering can be observed in a SESANS experiment.

Although extra focus is given to the real-space description of microstructure, and the correlation function in particular, we often connect it to the corresponding reciprocal space SANS formalism. This paper is limited to discuss finite ordering and samples with two phases distributed isotropically (unless stated otherwise). All together, this paper presents a toolkit that can be used for the analysis and understanding of a SESANS experiment.

1.2 The density distribution and its autocorrelation, Fourier transform and projection

The density distribution of a phase making up a material takes on the values

$$\rho(\mathbf{r}) = \begin{cases} 1 & \text{if } \mathbf{r} \text{ is inside the phase,} \\ 0 & \text{otherwise.} \end{cases} \quad (1.1)$$

The distribution $\rho(\mathbf{r})$ contained in a volume V is fluctuating around its mean value

$$\phi = \frac{1}{V} \int_V \rho(\mathbf{r}) d\mathbf{r} \quad (1.2)$$

Which is the volume fraction of phase in the volume V . For a two phase system, the fraction of the other phase is $1 - \phi$. The density fluctuations around the average is

$$\Delta\rho(\mathbf{r}) = \rho(\mathbf{r}) - \phi, \quad (1.3)$$

and the autocorrelation function of the density distribution function is:

$$\gamma(\mathbf{r}) = \frac{\int_V \Delta\rho(\mathbf{r}') \Delta\rho(\mathbf{r}' + \mathbf{r}) d\mathbf{r}'}{\int_V \Delta\rho(\mathbf{r}') \Delta\rho(\mathbf{r}') d\mathbf{r}'}, \quad (1.4)$$

so that $\gamma(0) = 1$. The integral in the denominator becomes after using Eqs. (1.1)-(1.3)

$$\int_V [\Delta\rho(\mathbf{r}')]^2 d\mathbf{r}' = V\phi(1 - \phi), \quad (1.5)$$

which is a mean square fluctuation term. The correlation function for an isotropic distribution depends on the modulus of \mathbf{r} only (i.e., $\gamma(r) = \gamma(\mathbf{r})$). The formalism assumes no long-range order, so that $\gamma(r)$ will be zero for $r = \infty$. In fact, $\gamma(r)$, as defined here, is invariant to which phase is being correlated, and one can interchange the 1 and the 0 in Eq. (1.1), meaning that $\gamma(r)$ of phase one is equal to $\gamma(r)$ of phase two, which also leads to Babinet's theorem [23].

The shape and width of $\gamma(r)$ depends on the structure of the density distribution, which might be random, scale invariant (fractal), ordered, well defined (a sphere, a particle) etc.

The projection of $\gamma(r)$ along, for example, the Cartesian coordinate x is

$$G(z) = \frac{2}{\xi} \int_0^\infty \gamma(x, 0, z) dx, \quad (1.6)$$

where

$$\xi = 2 \int_0^\infty \gamma(x, 0, 0) dx. \quad (1.7)$$

For a spherical symmetric (i.e., isotropic) density distributions the projection $G(z)$ can be written as

$$G(z) = \frac{2}{\xi} \int_z^\infty \frac{\gamma(r)r}{\sqrt{r^2 - z^2}} dr. \quad (1.8)$$

Provided that $\gamma(r)$ decays to zero faster than $1/r$, the inverse transformation is found as:

$$\gamma(r) = -\frac{\xi}{\pi} \int_r^\infty \frac{G'(z)}{\sqrt{z^2 - r^2}} dz \quad (1.9)$$

where the prime denotes differentiation w.r.t z . After integrating by parts in Eq. (1.9) the derivative is avoided and the transformation reads

$$\gamma(r) = \frac{\xi}{\pi} \int_r^\infty \frac{G(r) - G(z)}{(z^2 - r^2)^{3/2}} z dz \quad (1.10)$$

Thus, $\gamma(r)$ and $G(z)$ are Abel transform pairs [14]. $G(z)$ is the sample dependent property measured in a SESANS experiment together with the correlation length of the density distribution

$$\xi = 2 \int_0^\infty \gamma(r) dr. \quad (1.11)$$

The power spectrum $I(q)$, proportional to the intensities measured in a conventional small-angle scattering experiment, is the Fourier amplitudes squared of the density fluctuations and therefor the Fourier transformation of $\gamma(r)$ according to the convolution theorem [14]. Assuming a rotational invariant density distribution and using Eq. (1.5) the Fourier transformation becomes

$$\begin{aligned} I(q) &= \frac{1}{V\phi(1-\phi)} \left| \int_V e^{-i\mathbf{q}\mathbf{r}} \Delta\rho(\mathbf{r}) d^3\mathbf{r} \right|^2 \\ &= \int_V e^{-i\mathbf{q}\mathbf{r}} \gamma(\mathbf{r}) d^3\mathbf{r} \\ &= 4\pi \int_0^\infty \langle e^{-i\mathbf{q}\mathbf{r}} \rangle \gamma(r) r^2 dr \\ &= 4\pi \int_0^\infty \frac{\sin(qr)}{qr} \gamma(r) r^2 dr, \end{aligned} \quad (1.12)$$

where $\langle e^{-i\mathbf{q}\mathbf{r}} \rangle = \langle e^{-iqr \cos\theta} \rangle = \frac{\sin(qr)}{qr}$ is the angular average over θ and the second equality is due to the convolution theorem [14]. The fourth equality assumes an isotropic distribution $\Delta\rho(\mathbf{r})$. The inverse transformation is

$$\gamma(r) = \frac{1}{2\pi^2} \int_0^\infty \frac{\sin(qr)}{qr} I(q) q^2 dq \quad (1.13)$$

The so called Fourier-Abel-Hankel [14] cycle relates the three functions, $I(q)$, $G(z)$ and $\gamma(r)$ to each other. The relationships are illustrated schematically in Fig. 1.1 for isotropic distributions, where the figure shows the inverse related Abel-Hankel-Fourier transformation and also the operations yielding $\gamma(r)$, $I(q)$ and $G(z)$ directly from $\rho(r)$. Note that $G(z)$ can be calculated as the correlation function of the Abel transformation of $\rho(r)$. The Abel transformation of a circular symmetric function is equivalent to the Hankel transformation of that functions Fourier transform, thus $G(z)$ is the Hankel transformation of $I(q)$, mathematically

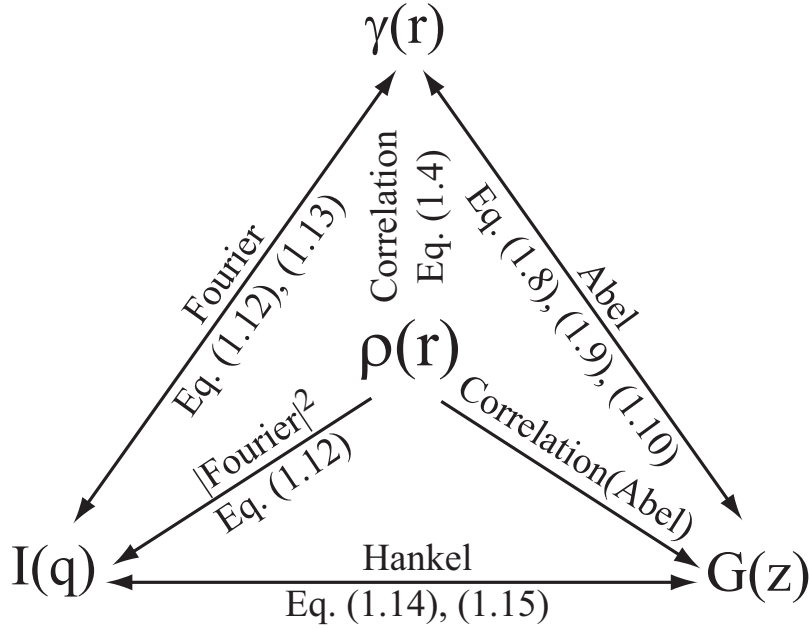


Figure 1.1: The relationship between the Abel, Hankel and Fourier transformation for an isotropic distribution $\rho(r)$. Note that $G(z)$ can be found by calculating the autocorrelation function of the projection of $\rho(r)$.

$$G(z) = \frac{1}{2\pi\xi} \int_0^\infty J_0(qz)I(q)q dq \quad (1.14)$$

and the inverse transformation is

$$I(q) = 2\pi\xi \int_0^\infty J_0(qz)G(z)z dz \quad (1.15)$$

directly relating a SESANS measurement to a SANS measurement, see Sec. 1.4. The correlation length is here given by

$$\xi = \frac{1}{2\pi} \int_0^\infty I(q)q dq. \quad (1.16)$$

When calculating $\gamma(r)$ and $G(z)$ based on a numerical density distribution $\Delta\rho(r)$ it is computationally more efficient to calculate in the wavenumber domain by using Eq. (1.12) and Eq. (1.14). Such a procedure bypasses the calculation of the correlation function in Eq. (1.4).

Previously, this was expressed in cartesian coordinates where $G(z)$ is a 2D Fourier transform of $I(\mathbf{q})$ [80]. If $q_x = 0$ (i.e., the small-angle scattering approximation) the correlation function becomes

$$G(y, z) = \int_{-\infty}^\infty \int_{-\infty}^\infty I(q_y, q_z) e^{-i(q_y y + q_z z)} dq_y dq_z. \quad (1.17)$$

Note also that in the current SESANS setup there is no sensitivity in the y direction, i.e., the measurement is as a function of correlation across z . Switching to polar coordinates

in real and reciprocal space (i.e., $q_y = q \cos \theta$, $q_z = q \sin \theta$, $x = r \cos \varphi$ and $y = r \sin \varphi$) with the area element $dq_y dq_z = q dq d\theta$ gives

$$\begin{aligned} G(r) &= \int_0^\infty \int_0^{2\pi} I(q) e^{-iqr(\cos \varphi \cos \theta + \sin \varphi \sin \theta)} q dq d\theta \\ &= \int_0^\infty \int_0^{2\pi} I(q) e^{-iqr \cos \theta} q dq d\theta \\ &= \int_0^\infty I(q) \left(\int_0^{2\pi} e^{-iqr \cos \theta} d\theta \right) q dq \\ &= \frac{1}{2\pi} \int_0^\infty J_0(qr) I(q) q dq. \end{aligned} \quad (1.18)$$

Since $y = 0$, as in the current SESANS setup, and after normalising with ξ this becomes Eq. (1.14).

Similarly, $I(q)$ can be expressed as a Fourier transformation in cartesian coordinates, but now in 3D

$$\begin{aligned} I(q_y, q_z) &= \int \int \int e^{-i(q_y y + q_z z)} \gamma(x, y, z) dx dy dz, \\ &= \int \int e^{-i(q_y y + q_z z)} G(y, z) dy dz, \end{aligned} \quad (1.19)$$

leading to Eq. (1.15) after switching to polar coordinates in the same way as in Eq. (1.18).

1.3 Basic principle of the SESANS technique

SESANS makes use of the Larmor precession of neutrons in magnetic field regions [54]. The geometry of the field regions encodes the scattered angles of the neutrons, meaning that the angular resolution of the instrument becomes independent of the angular divergence of the incoming beam [66], see Fig. 1.2. The neutron precesses at a certain angle φ_1 in the first field $B+$ region and the precession is reversed in the second field $B-$. Scattering at small angles 2θ between the fields breaks this symmetry and makes the neutron travel a different path length through the second field so that ($\Delta\varphi = |\varphi_1 - \varphi_2| \neq 0$). The net precession $\Delta\varphi$ causes the beam to depolarise, the polarisation is directly related to the projection of the autocorrelation function of the sample.

1.4 SESANS measured quantities and standard data interpretation

SESANS measures $G(z)$ through the transmission of polarisation, thus the instrument itself is performing Eq. (1.14). The polarisation as a function of the real-space parameter (spin-echo length) z after normalisation with an empty beam (i.e., $P(0) = 1$)

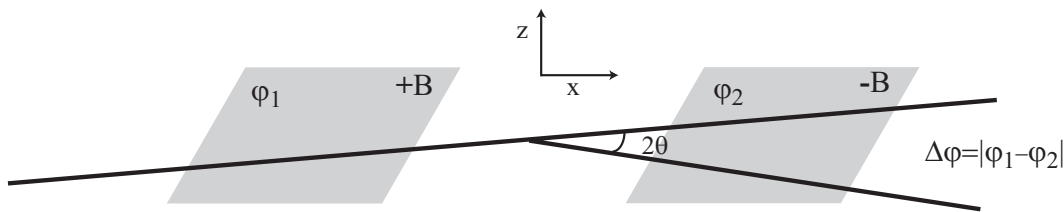


Figure 1.2: Schematic drawing of the SESANS principle and the coordinate frame of reference. In the absence of scattering the neutron spin precesses through an angle φ_1 in the two magnetic fields. Scattering at small angles 2θ breaks the symmetry of the setup and give rise to a net precession $\Delta\varphi = |\varphi_1 - \varphi_2| \neq 0$, which is detected as depolarisation of the neutron beam.

is

$$P(z) = e^{\Sigma_t(G(z)-1)}, \quad (1.20)$$

where Σ_t is the average number of times a neutron scatters when traversing the sample, i.e., this takes into account multiple scattering. For a two phase system this becomes [23]

$$\Sigma_t = \lambda^2 t (\Delta\rho_0)^2 \phi (1 - \phi) \xi. \quad (1.21)$$

Where t is the sample thickness, λ is the neutron wavelength and $\Delta\rho_0$ is the neutron scattering length density (SLD) contrast between the two phases (discussed below). The $(1 - \phi)$ term is due to the subtraction of the average density in Eq. (1.3), this term, however, does not appear in a single-particle scattering treatment. The last terms in Eq. (1.21) originate from the following correlation function

$$\int dr \langle \Delta\rho_0(0) \Delta\rho_0(r) \rangle_V = (\Delta\rho_0)^2 \phi (1 - \phi) \xi, \quad (1.22)$$

where $\Delta\rho_0(r)$ is the SLD contrast distribution of the sample. A density distribution with no long-range ordering means that $G(\infty) = 0$, thus

$$P(\infty) = e^{-\Sigma_t}, \quad (1.23)$$

yielding the so called saturation level of the measured polarisation. $P(\infty)$ is the fraction of neutrons that does not scatter when traversing the sample. This level contains information about both concentrations through ϕ and the microstructure through ξ as well as on the chemical composition via the SLD contrast

$$\Delta\rho_0 = \rho_1 - \rho_2. \quad (1.24)$$

The individual scattering length densities can be calculated by

$$\rho_i = \frac{\delta N_a}{M} \sum_{j=1}^n b_j, \quad (1.25)$$

where δ is the solid density of the material, N_a is Avogadro's constant, M is the molecular mass of the molecule making up the material and finally b_j is the bound

coherent scattering length of element j [73]. The sum is running over all n atoms in the molecule. The neutron scattering length for deuterium and hydrogen is different, making it possible to work with contrast variation, either by deuterium labelling of the molecules or by using proper mixing ratios of light and heavy water. Contrast matching with heavy/light water can be used in order to simply determine the SLD of a structure or to ensure proper experimental conditions so that the final transmission of the polarisation $P(\infty)$ is optimal ($0.9 < P(\infty) < 0.3$).

Although, it is the polarisation $P(z)$ that is the raw data outcome of a SESANS measurement, the focus of this paper will be on $G(z)$ and on the correlation length ξ . From an experimental point of view:

$$G(z) = 1 - \frac{\ln P(z)}{\ln P(\infty)} \quad (1.26)$$

and

$$\xi = -\frac{\ln P(\infty)}{\lambda^2 t (\Delta\rho_0)^2 \phi(1-\phi)}, \quad (1.27)$$

provided that the saturation level $P(\infty)$ is well determined and that the sample is well characterised in terms of $\Delta\rho_0$ and ϕ .

The differential scattering cross section, i.e., the measured intensities, measured as a function of q in conventional SANS is

$$\frac{d\Sigma}{d\Omega}(q) = (\Delta\rho_0)^2 \phi(1-\phi) I(q), \quad (1.28)$$

and can be related to a SESANS experiment via the formalism described in Sec.1.2 and Eq. (1.20). Note that, when considering measurements, the relationship between $\frac{d\Sigma}{d\Omega}(q)$ and $\gamma(r)$, through the Fourier transformation, is only valid within the Born approximation.

The second moment of $\frac{d\Sigma}{d\Omega}(q)$ is invariant to the structure, i.e.,

$$Q = \int_0^\infty \frac{d\Sigma}{d\Omega}(q) q^2 dq = (\Delta\rho_0)^2 \phi(1-\phi) = \frac{\Sigma_t}{\lambda^2 t \xi}. \quad (1.29)$$

Q is called the Porod invariant [23]. Normalising the first moment with Q gives the correlation length, i.e.,

$$\xi = \frac{\pi}{Q} \int_0^\infty \frac{d\Sigma}{d\Omega}(q) q dq. \quad (1.30)$$

The intensity extrapolated to $q = 0$ is proportional to the isothermal compressibility, thus

$$\frac{d\Sigma}{d\Omega}(0) = (\Delta\rho_0)^2 \phi(1-\phi) \int G(z) z dz. \quad (1.31)$$

1.4.1 Visual interpretation of measurements

A SESANS measurement can often be given an intuitive way of interpretation, which is useful for experimentalists outside the scattering community. The reason for this is the

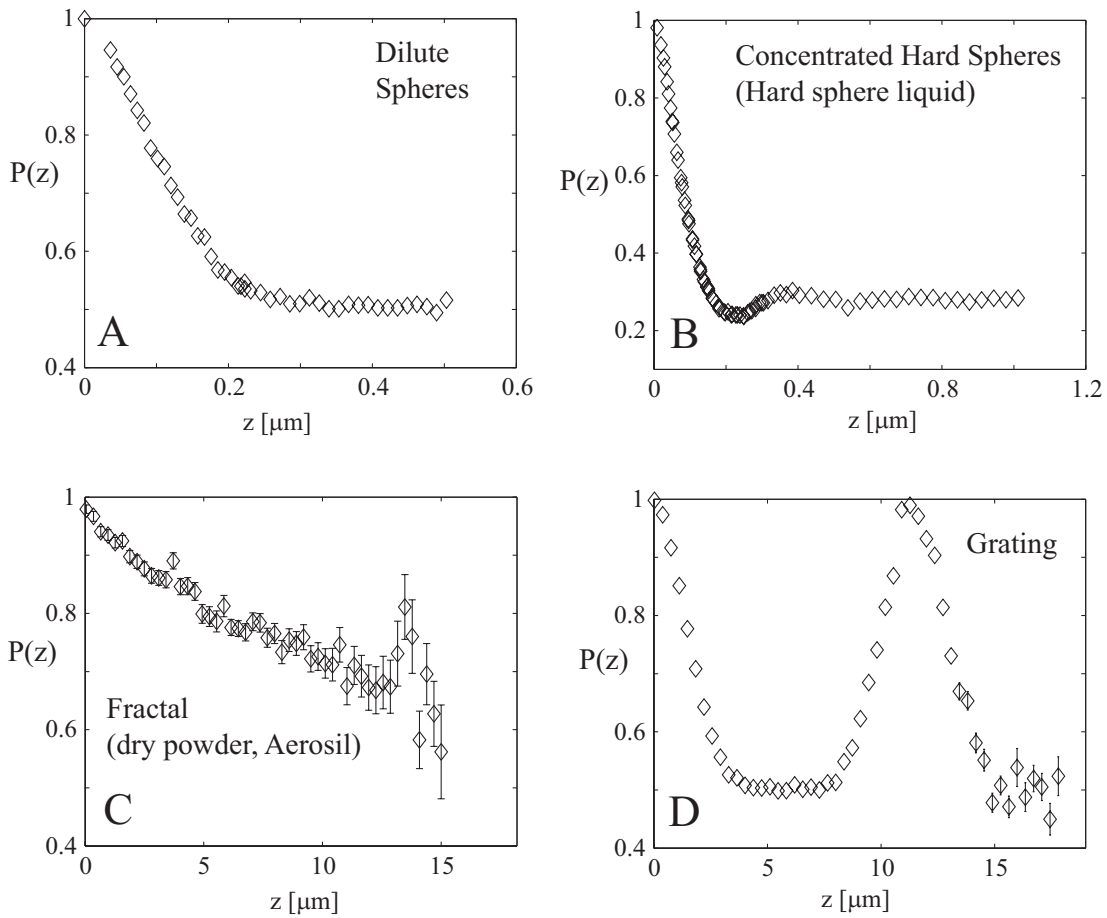


Figure 1.3: These are SESANS measurements conducted on various samples. Top left figure A is a measurement on a dilute sample of sterically stabilised silica spheres. Figure B is the result from a more concentrated dispersion of silica spheres. For more information on measurement A and B see [44]. Figure C shows a measurement on a dry nano-powder of silica and finally figure D shows a measurement of a grating made up of periodic silicon beams.

real-space nature of SESANS. A diverse set of measurements are presented in Fig. 1.3, measurements that illustrate the real-space character of this technique.

From these measurements it is possible to determine the diameter of the sphere (Fig. 1.3A); nearest neighbour distances in the hard-sphere liquid (Fig. 1.3B); the fractal dimension of the powder Fig. 1.3C; the width, periodicity and thickness of the ridges making up the grating in Fig. 1.3D.

1.4.2 The width of the polarisation curve

For dilute isotropic materials without any ordering, $\gamma(r)$ and therefore $G(z)$ and $P(z)$ decay at the length scale of the size of the inhomogeneities making up the sample structure. A plot of $P(z)$ versus z starts at unity, decays and saturates at a spin-echo length equal to the size that characterises the sample, this is the point at which no more density correlations are seen in the sample, or the largest size at which correlations exist in the sample. For a dilute sample of monodisperse spheres this point will be exactly at the diameter of the sphere (the longest line possibly drawn inside a sphere is the diameter). For a dilute sample of monodisperse cylinders of length l and diameter D this point will be strictly $\sqrt{l^2 + D^2}$.

An illustration regarding the basic interpretation of a SESANS measurement is made in Fig. 1.4.

1.4.3 The height of the polarisation curve

The level $P(\infty)$ of the saturation point will depend on the structure of the sample as well as on its average compositions, see Eq. (1.23). The saturation level is proportional to the chemical composition $\Delta\rho_0$, the packing fraction ϕ and the correlation length ξ of the sample inhomogeneities, and therefore on the sample structure (see also Fig.1.4). It is worthwhile to note that ξ is not the same as the saturation point l_{\max} on the horizontal axis. A conceptual interpretation is that: ξ is the average length of all lines possibly drawn inside the density fluctuations whilst the saturation point, on the horizontal axis, is the largest possible line drawn inside the inhomogeneity. A sphere with diameter D corresponds to a correlation length of $\xi = 3/4D$. Thus, the difference between ξ and l_{\max} gives information about the compactness of the distribution.

1.4.4 The initial slope of the polarisation

The initial slope of the polarisation $dP(z)/d(z)$ can be used to analyse a SESANS measurement. The slope will be proportional to the contrast $\Delta\rho_0$ and the packing fraction ϕ of the inhomogeneities. The slope is to some approximation independent on the arrangement of the inhomogeneities. By dividing Eq. (1.21) with ξ one obtains

$$-\frac{d\ln(P(z))}{dz} \simeq t\lambda^2(\Delta\rho_0)^2\phi(1-\phi). \quad (1.32)$$

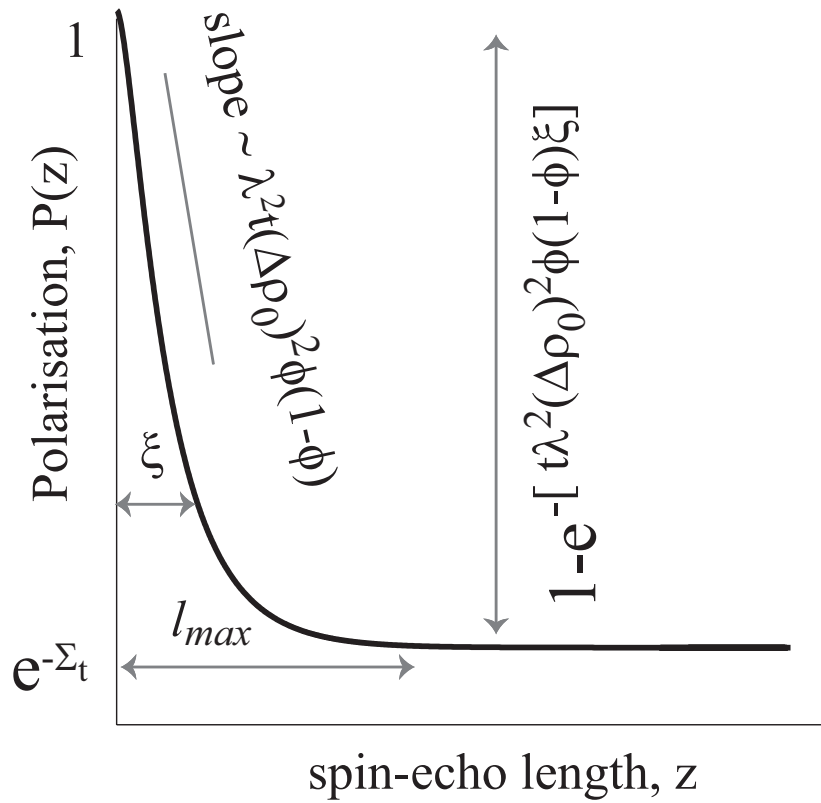


Figure 1.4: Schematic plot of a SESANS measurement where the polarisation is plotted against the spin-echo length z . l_{max} is the largest length scale characteristic for the density distribution. ξ is the correlation length of the density distribution and is an average size that describes the microstructure. The initial slope can be approximated to depend only on the chemical composition, via the scattering length density $\Delta\rho_0$, and the phase fraction through ϕ .

This, in some sense, is the SESANS equivalent to the Porod invariant, to be discussed in Sec. 1.4.6. The argument for this structural invariance is that the two length scales, the ratio of l_{\max} and the correlation length ξ , have cancelled each other. An illustration of this can be found in measurements on the structure of food related emulsion gels. Several gels were prepared and with different processes, but with the same composition. The initial slope of all measurements was identical [8]. By applying such analysis one could follow the change in packing fraction and chemical composition as the sample evolves, provided that the relation between the width l_{\max} and the correlation length ξ is unchanged throughout the procedure.

The initial slope can also be used to investigate anisotropy in the density distribution of a sample, provided that the sample can be re-oriented and rotated in the beam without disturbing its structure. An isotropic sample has to give the same slope in all directions. The initial slopes have been used to determine the grain density and to investigate the microstructure structure of a cohesive powder undergoing compression [2] as well as for the study of anisotropy [3]. It was shown that uniaxial compression of a nanotube powder induces anisotropy in the density distribution, whereas no anisotropy was found in a compressed powder composed of isotropic grains. It was also shown that the powders can be well described by rather simple correlation functions, which describe fractal or self affine materials.

1.4.5 Extracting the correlation function $\gamma(r)$ from a SESANS measurement

For many samples there is no *a priori* information about the density correlation function of the sample. In such cases the goal could be to extract directly a correlation function $\gamma(r)$ from the SESANS measurement. Such a procedure was applied in the data analysis of dairy products [79] and emulsion gels [8].

In general, calculating $\gamma(r)$ from a measurement involves differentiating the measured data according to Eq. (1.9). This does not seem to be very practical due to the typically noisy data obtained from measurements, and the errors produced by such a step will be blown up by the subsequent integration. An alternative is Eq. (1.10) or one could perform the inverse transformations according to Eq. (1.15) and then using Eq. (1.13) to calculate $\gamma(r)$. A numerical problem with such direct methods is that the value of $G(z)$ for when it approaches zero is not well determined from the experimental $P(z)$.

The proposed data analysis describes the autocorrelation function of the material with a sum of n Gaussians having some dimensionless amplitudes A_i and widths a_i (having the dimension of length). It is important to keep n low in order to avoid over-parameterising the data.

By using this method it is possible to describe a fast changing slope at the shorter z 's and a final slope, without over parameterising the fit function. This is mathematically convenient, since the Gaussian function is a self reciprocal [15] function, meaning that

it survives the Fourier, Hankel and therefore also the Abel transformation.

Measurements are fitted by a sum of Gaussians.

$$G(z) = \frac{\sum_{i=1}^n A_i e^{-(z/a_i)^2}}{\sum_{i=1}^n A_i}, \quad (1.33)$$

where A_i is the amplitude of the Gaussian and a_i is its width. The sum runs over n Gaussians. The correlation length ξ is

$$\xi = \frac{\sqrt{\pi} \sum_{i=1}^n a_i}{\sum_{i=1}^n A_i/a_i}. \quad (1.34)$$

Thus, the autocorrelation function in this formalism becomes

$$\gamma(r) = \frac{\sum_{i=1}^n A_i/a_i e^{-(r/a_i)^2}}{\sum_{i=1}^n A_i/a_i}. \quad (1.35)$$

1.4.6 Porod's analysis: The invariant and the specific surface

In conventional SANS it is possible to relate the scattered intensity at higher q to the surface area S of the density distribution

$$I(q) \propto \frac{S}{q^4}. \quad (1.36)$$

This is known as the Porod law. Debye [19] made the connection to the real-space correlation function and showed that for a two phase material characterised by sharp phase boundaries

$$\gamma(r) = 1 - \frac{Sr}{4V}. \quad (1.37)$$

and

$$\lim_{r \rightarrow 0} \gamma'(r) = -\frac{S}{4V}. \quad (1.38)$$

Where V is the volume containing the distribution. The Fourier transformation of such a linear function yields the scaling seen in Eq. (1.36). It is possible to relate the projection of $\gamma(r)$ to the specific surface area. Using Eq. (1.10), shifting the integration boundaries by letting $u = z - r$ and differentiating yields

$$\begin{aligned} \gamma'(r) = & \quad (1.39) \\ -\frac{\xi}{\pi} \int_0^\infty & \frac{1}{u^{3/2}(u+2r)^{5/2}} ([G(r) - G(r+u)](2u+r) + \\ & [(G'(r+u) - G'(r))(u+r)(u+2r)] du. \end{aligned}$$

Evaluating for the limit $r \rightarrow 0$ and using Eq. (1.37) gives the specific surface in the SESANS formalism

$$\frac{S}{V} = \frac{8\xi}{\pi} \int_0^\infty \frac{1}{z^3} [G(0) - G(z) + \frac{1}{2}zG'(z)] dz, \quad (1.40)$$

where $G'(0) = 0$ for all finite distributions. The integral in Eq. (1.40) exists if at least $G(z) \propto -z^2$.

The Porod invariant Q introduced in Eq. (1.29) is the mean square fluctuation of the scattering length density distribution, i.e., $\phi(1 - \phi)(\Delta\rho_0)^2$. In a conventional scattering experiment this is found as an integral over the scattered intensities [23] (the second moment of the distribution $I(q)$). The SESANS analogue is found by calculating the initial slope Sec. 1.4.4, i.e. $-\frac{d\ln(P(z))}{dz} \frac{1}{i\lambda^2} = (\Delta\rho_0)^2\phi(1 - \phi)$ for a two phase material.

1.4.7 Guinier approximation

The Guinier law relates the radius of gyration R_g of the particle to the scattered intensity. For small q this means that

$$I(q) \simeq e^{-q^2 R_g^2/3}. \quad (1.41)$$

An equivalent law for SESANS has been derived by essentially applying the transformation in Eq. (1.14) to the Gaussian function, therefore yielding a new Gaussian [80]. A series expansion of $G(z)$ confirmed this [39] and is based on the wavenumber representation of $G(z)$. It should be stressed, however, that the average size describing the structure is measured directly as the width of a $P(z)$ versus z plot, providing a very straightforward way of extracting the size best describing the sample.

1.5 Power-law scattering and the dimensionality of $\rho(r)$

A scaling-law can be derived for $\gamma(r)$ based on the dimensionality of the distribution $\rho(r)$. For a scale invariant density distribution, the mass $M(r)$ falling within a radius r will scale as

$$M(r) \propto r^d, \quad (1.42)$$

where d is the dimensionality of the object (Hausdorff, packing, fractal dimension etc.). Objects are called fractals if this dimensionality exceeds the topological dimension of the object [51]. Normalising and differentiating w.r.t. r gives in a 3D envelope space

$$\gamma(r) = \frac{dM(r)}{2\pi r^2 dr} \propto r^{d-3}. \quad (1.43)$$

In the wavenumber domain the powerlaw reads

$$I(q) \propto q^{-d}, \quad (1.44)$$

sometimes referred to as power-law scattering [72]. Translating the power law into SESANS means calculating the projection according to Eq. (1.8). For the integral transformation to converge, $\gamma(r)$ has to decay faster than r^{-1} , thus the integral in

Eq. (1.8) does not converge for $d > 2$, and one is forced to introduce a cutoff function or a boundary in the integration limit. For $d < 2$, however, this scaling-law transforms into

$$G(z) \propto z^{d-2}. \quad (1.45)$$

Thus, the fractal dimension for density distribution which scales with $d < 2$ can be found by representing $G(z)$ on a log-log scale.

After making the correlation function finite by imposing a finite upper integration boundary a in Eq. (1.8) gives for $z < a$

$$G(z) \propto z^{d-3} {}_2F_1 \left[\frac{1}{2}, \frac{3-d}{2}; \frac{3}{2}; -\frac{a^2}{z^2} \right] \quad \text{for } d \leq 3, \quad (1.46)$$

where a is a measure of the size of the microstructure structure and ${}_2F_1$ is the Hypergeometric function. Examining the limit $d = 1$ (needles):

$$G(z) \propto z^{-1} \tan^{-1}[a/z], \quad (1.47)$$

and for a dimensionality $d = 2$ (membranes):

$$G(z) \propto \ln[a + (a^2 - z^2)] - \ln[z]. \quad (1.48)$$

1.5.1 Finite fractals

Taking into account a finite extension of the fractal structure is commonly done by introducing an exponential cutoff [72] so that

$$\gamma(r) \propto r^{d-3} e^{-r/a}, \quad (1.49)$$

where a represents the spatial extension of the fractal. Including a lower building block size a_0 that builds up the fractal can be done by

$$\gamma(r) = (r/a_0 + 1)^{d-3} e^{-r/a}. \quad (1.50)$$

This correlation function has the important property of being unity at $r = 0$. The proposed correlation function is to the authors knowledge proposed here for the first time. Using Eq. (1.50) enables the calculation of the correlation length (see Eq. (1.11)), i.e.,

$$\xi = 2a_0 e^{a_0/a} E_{3-d}(a_0/a), \quad (1.51)$$

where E_n is the generalised Exponential integral. We are unable to express $G(z)$ analytically, but present numerical results in Fig. 1.5 for $d = 2.7$, $d = 2.5$ and $d = 2.3$, with $a/a_0 = 1 \times 10^3$. Although, it is possible to calculate an analytical expression for $G(z)$ using Eq. (1.49) in terms of Hypergeometric functions, this expression is too lengthy and not shown here.

No direct method (log-log plot, semi-log plot etc) of illustrating the scattering from fractals with $d > 2$ in SESANS data seems to exist, but one is forced to use

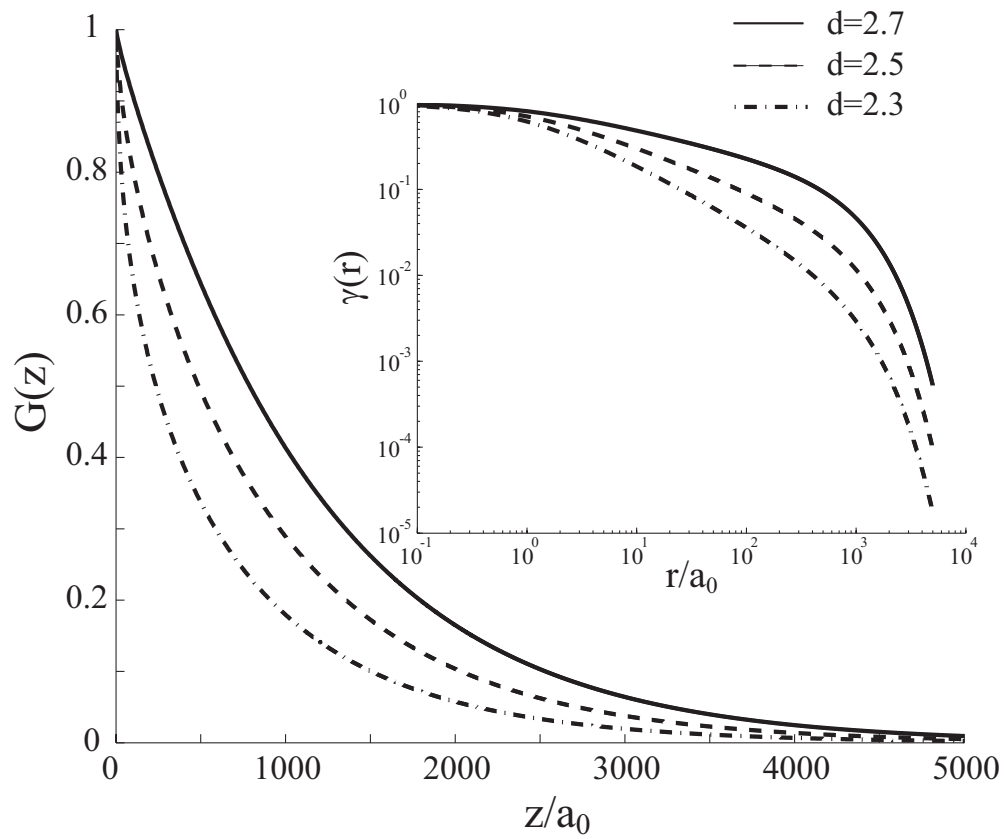


Figure 1.5: $G(z)$ for a finite fractal according to Eq. (1.50) with $a/a_0 = 1 \times 10^3$. The solid line is with $d = 2.7$, dashed line represents $d = 2.5$ and the dotted-dashed line is for $d = 2.3$. The inset shows the corresponding $\gamma(r)$ on a loglog scale.

numerical techniques or involved analytical formulas in order to fit a d to the measured data. In Fig 1.5 it is evident that the projection becomes generally narrower for lower dimensionalities but the projection makes the decay less sharp when comparing with $\gamma(r)$. The formalism described here has been used to model SESANS measurements on dry powders upon compaction [3].

1.5.2 Random two phase media

For a perfectly random inhomogeneous solid Debye, Anderson and Bueche (DAB) [19], [20] conjectured that

$$\gamma(r) = e^{-r/a}, \quad (1.52)$$

where a represents a measure of the size of the random inhomogeneities. The argument for its validity is that its series expansion at small r yields Eq. (1.37). The projection of this correlation function is

$$G(z) = \frac{z}{a} K_1(z/a), \quad (1.53)$$

where K_n is the modified Bessel function of the second kind. The Fourier power spectrum is

$$I(q) = \frac{8a^3\pi}{(1+(qa)^2)^2}. \quad (1.54)$$

This can be seen as a special case of a more general correlation function for describing self-affine random density distributions [41] and [35].

$$\gamma(r) = \frac{2}{\Gamma(H)} \left(\frac{r}{2a}\right)^H K_H\left(\frac{r}{a}\right), \quad (1.55)$$

where $K_n(x)$ is the Modified Bessel function of the second kind and Γ is the Gamma function. H is the so called Hurst exponent, related to the space filling capacity of the structure ($d = d_t + 1 - H$), with d_t being the topological dimension of the structure. The limit $H = 1$ represents a smooth euclidian field and $H = 0$ is a space filling euclidian field (see Fig 1.6). For $H = 1/2$ this reduces to the DAB formula Eq. (1.52), describing a perfectly random inhomogeneous solid.

Two domains are usually discussed with regards to the Hurst exponent H . First for $H > 1/2$ where the distribution is persistent, so that a previous event is likely to be followed by a similar event, characteristic for smoothness and long-range correlations. Secondly, when H is below $1/2$ the distribution is called anti-persistent, meaning that the previous event is more likely to be followed by a different event (roughness, short range correlations).

The projection, measured in a SESANS experiment, has the analytical solution:

$$G(z) = \frac{2}{\Gamma(H + 1/2)} \left(\frac{z}{2a}\right)^{H+1/2} K_{H+1/2}\left(\frac{z}{a}\right), \quad (1.56)$$

and the correlation length is

$$\xi = \frac{2\sqrt{\pi}a\Gamma(H + 1/2)}{\Gamma(H)}, \quad (1.57)$$

being a decaying function for decreasing H . This model has been used to investigate the microstructure development in a cohesive powder undergoing compressive strain using SESANS [2].

The corresponding wavenumber domain expression measured in SANS is found by Fourier transforming Eq.(1.55), yielding

$$I(q) = \frac{4a^3\pi(1+2H)}{(1+(qa)^2)^{\frac{3}{2}+H}}. \quad (1.58)$$

Fig. 1.6 illustrates the significance of the Hurst exponent. The autocorrelation function of the 1D curves $\rho(x)$ are given by Eq. (1.55), with $a = 1$ and H as denoted in the figure. Note that a is a scaling factor in the exponent and not the maximum size of the fluctuations, which is rather about $5a$. These curves have been calculated by filtering a uniform deviate (white noise) in the wavenumber domain. The filter is the Fourier spectrum of the distribution, i.e., the square root of Eq. (1.58). The inverse Fourier transformation of the filtered noise yields a real-space representation of a distribution having the correlation Eq. (1.55), see for more information [41].

At least the model correlation function has to satisfy $\gamma(0) = 1$, $\gamma(\infty) = 0$ and to be realistic $\gamma'(0) < 0$ (see Eq. (1.37)). One such correlation function has been proposed above in Eq. (1.50). Similar, but a more simple function for the projection could be

$$G(z) = e^{-(z/a)^\alpha}, \quad (1.59)$$

where $0 < \alpha < 2$ is related to the structure of the phase boundary. The limit $\alpha = 1$ corresponds to $H = 0$ in the above formalism and would be scattering from a 2D distribution. The domain $1 < \alpha < 2$ corresponds to more compact distributions, let's say $d > 2$ and the lower domain $0 < \alpha < 1$ corresponds to the more open and branched distributions with higher specific surfaces, or $d < 1$. This correlation function, although phenomenological, is at least not over-parameterised.

1.5.3 Numerical examples of random and fractal media

Fig. 1.7 shows a Diffusion Limited Aggregate (DLA) [52], composed of >18000 particles. The left part of the figure represents a random density distribution (in 200^3 voxels) according to the DAB formalism.

The random density distribution was simulated in the wavenumber domain by applying a filter $\sqrt{I(q)}$ according to Eq. (1.58) on white noise generated in the wave number domain (here with $H = 1/2$). The spatial domain representation is then obtained by inverse fast Fourier transformation. Both distributions are discretised so that $\rho(x, y, z) = \{0, 1\}$, the packing fraction is $\phi = 0.5$ for the random media. And about $\phi = 0.01$ for the DLA cluster (depending on how the boundary is defined).

The correlation function and $G(z)$ was calculated by means of Fourier transformations according to Eq. (1.12) and Eq. (1.14). This procedure is computationally more efficient as compared to calculating the autocorrelation function in real space. Fig. 1.7

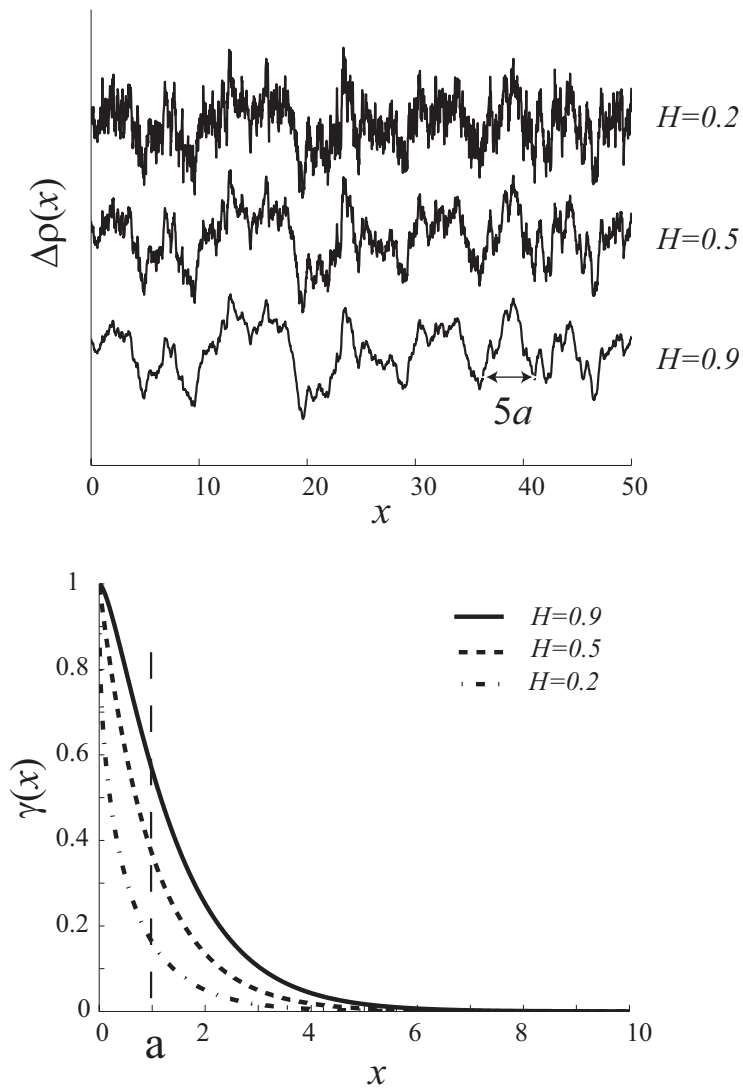


Figure 1.6: The top figure shows examples of reconstructed 1D density distributions $\rho(x)$ based on the von Karman correlation function Eq. (1.55). The corresponding correlation functions are shown in the bottom figure. The characteristic size is here $a=1$.

shows the results of this procedure in terms of $\gamma(r)$, $I(q)$ and $G(z)$ for the two real-space density distributions illustrated on top.

These examples, where the density distributions are explicitly known, help to highlight the real space nature of SESANS. The 3D distributions are plotted on the same scale as the correlation functions. The size of the random heterogeneities in the random case is about 20-25 units and rather well defined, the correlation function decays exponentially according to Eq. (1.52) and saturates around this region. For the DLA cluster, the initial decay is much sharper and we see a saturation at about half the size of the entire cluster.

1.6 Form factor and the correlation function of isolated shapes

For many simple shapes the autocorrelation function $\gamma(r)$ is known analytically. Its Fourier transform is called the form factor. The form factor is measured in SANS experiments in non-interacting and typically dilute samples. Important to note is that the form factor is only defined for a single particle in vacuum, that is to say –a single-particle treatment, where the correlations are only considered within the finite boundaries of the particle. Therefore, Eq. (1.5) becomes $V\phi$ and Eq. (1.21) reduces to: $\Sigma_t = \lambda^2 t (\Delta\rho_0)^2 \phi\xi$.

The challenge in order to calculate $\gamma(r)$ for a given geometry, is to find the intersecting volume between the object and its ghost image after shifting the ghost by a distance r .

1.6.1 Sphere

For a single sphere with radius R the autocorrelation function is

$$\gamma(r) = 1 - \frac{3}{4} \frac{r}{R} + \frac{1}{16} \left(\frac{r}{R}\right)^3 \quad (1.60)$$

for $r \leq 2R$ and zero elsewhere. The corresponding projection $G(z)$ is found by inserting Eq. (1.60) in Eq. (1.8) and integrating from zero to $2R$; this gives for $z \geq 0$ [45].

$$G(z) = \quad (1.61)$$

$$\Re \left[\sqrt{1 - \left(\frac{z}{2R}\right)^2} \left(1 + \frac{1}{2} \left(\frac{z}{2R}\right)^2\right) + 2 \left(\frac{z}{2R}\right)^2 \left(1 - \frac{z}{4R}\right)^2 \ln \left(\frac{z/R}{2 + \sqrt{4 - (z/R)^2}} \right) \right],$$

where \Re gives the real part. This removes the condition on $z \leq 2R$, since the real part is zero for $z > 2R$, which is practical for fitting procedures. The results for $G(z)$ and $\gamma(r)$ are shown in Fig. 1.8.

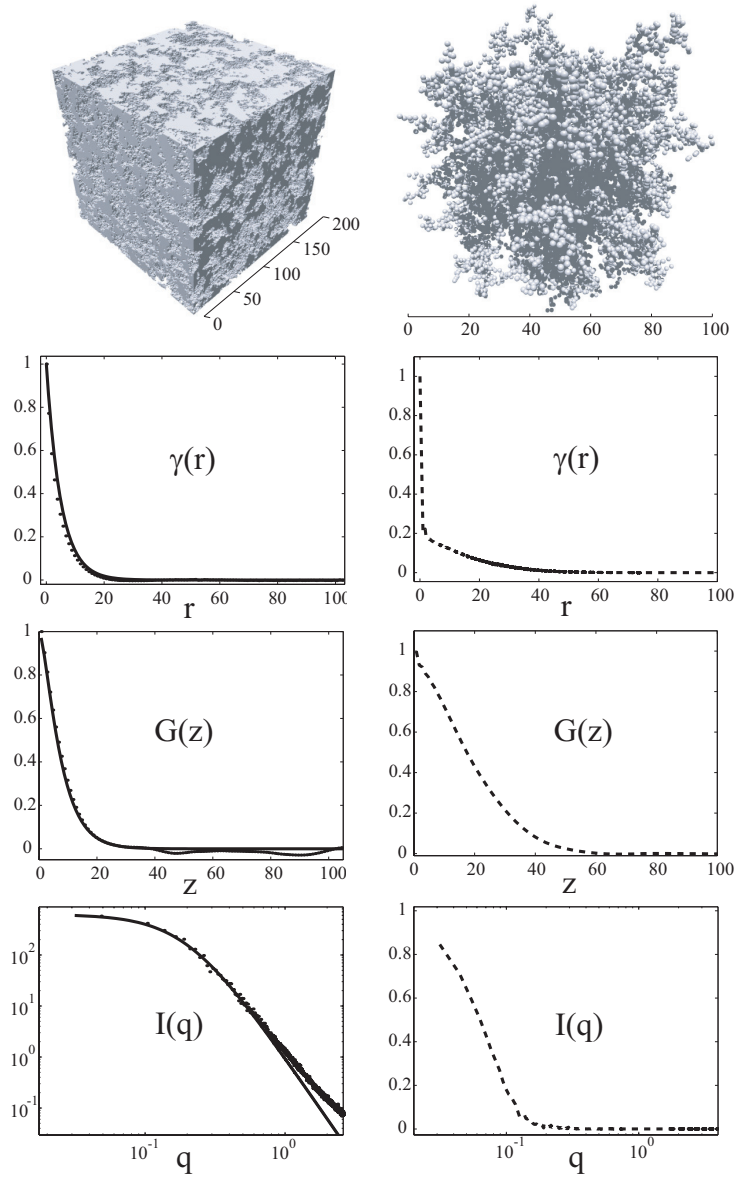


Figure 1.7: The autocorrelation function $\gamma(r)$, its projection $G(z)$ and the power spectrum $I(q)$ of the density distributions illustrated on top. The top left figure corresponds to a random distribution according to Eq.(1.52) with $a = 5$ (the line corresponds to Eq.(1.52), Eq.(1.53) and Eq.(1.54)). The figure to the right represents a DLA cluster and its corresponding correlation functions.

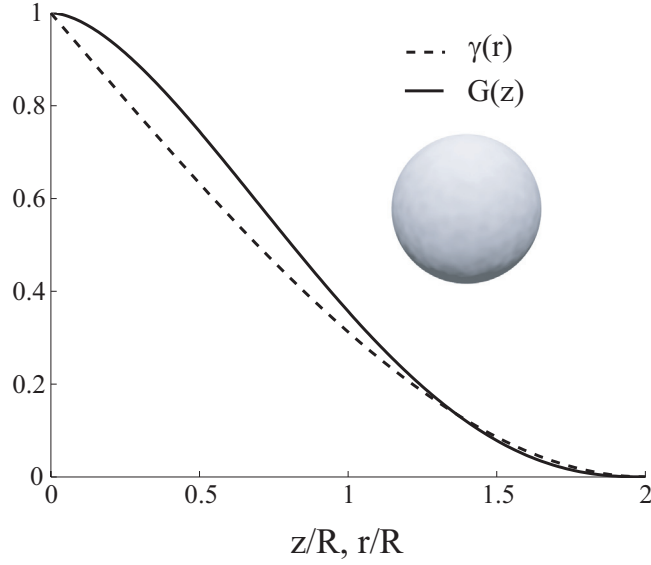


Figure 1.8: $\gamma(r)$ (dashed line) and its projection $G(z)$ (solid line) for a sphere with radius R according to Eq's (1.61) and (1.60).

The correlation length for a sphere is found by inserting Eq. (1.60) in Eq. (1.11), which yields $\xi = 3/2R$ and this is simply the average end-to-end distance one finds inside a sphere.

$G(z)$ for a sphere can be well approximated by the Gaussian function:

$$G(z) = e^{-\frac{3}{8}(z/a)^2}, \quad (1.62)$$

where $a \simeq R$.

Measurements on isolated sterically stabilised silica spheres are shown in Fig. 1.3 and [44].

1.6.2 Spherical shell and multi-shell

An object consisting of concentric shells of different densities ρ_i (and radii R_i) is a multi-shell. One extreme is a single spherical shell with some thickness. It can also be an onion containing many layers. The correlation function of two layers of radius R_i and R_j is

$$C(r, R_i, R_j) = \frac{4\pi}{3} R_j^3 \times \quad (1.63)$$

$$\begin{cases} 1 & 0 < r < R_i - R_j \\ \left[\frac{R_i^3 + R_j^3 + \frac{1}{8}r^3 - (R_i^2 + R_j^2) \frac{3}{4}r}{(R_i^2 - R_j^2) \frac{2}{8}r^{-1}} \right] / (2R_j^3) & R_i - R_j \leq r \leq R_i + R_j \\ 0 & R_i + R_j \leq r < \infty. \end{cases}$$

The correlation function $\gamma(r)$ for a multi-shell is a weighted sum over N layers of $C(r, R_i, R_j)$

$$\gamma(r) = \frac{1}{\left(\sum_{i=1}^N w_i\right)^2} \left(\sum_{i=1}^N w_i^2 C(r, R_i, R_i)^2 + 2 \sum_{i=1}^{N-1} \sum_{j=i+1}^N w_i w_j C(r, R_i, R_j) \right) \quad (1.64)$$

with $w_i = \rho_i - \sum_{k=1}^{i-1} \rho_k$ being the weight w_i and equaling ρ_i minus the density (SLD contrast) of the preceding layers.

The projection of Eq. (1.64) is:

$$\begin{aligned} \mathcal{P}(R_i, R_j, z) = & \quad (1.65) \\ & \frac{2}{3}\pi R_i^4 \left[H_0\left(\frac{R_i+R_j}{R_i}, \frac{z}{R_i}\right) - H_0\left(\frac{R_i-R_j}{R_i}, \frac{z}{R_i}\right) \right] + \\ & \frac{2}{3}\pi R_j^4 \left[H_0\left(\frac{R_i+R_j}{R_j}, \frac{z}{R_j}\right) - H_0\left(\frac{R_i-R_j}{R_j}, \frac{z}{R_j}\right) \right] + \\ & \frac{4}{3}\pi R_j^3 h_0(R_i - R_j, z) - \\ & \frac{1}{4}\pi (R_i^2 - R_j^2)^2 [h_0(R_i + R_j, z) - h_0(R_i - R_j, z)], \end{aligned}$$

where

$$h_1(\alpha, z) = 2\Re \left[\sqrt{\alpha^2 - z^2} \right], \quad (1.66)$$

\Re denotes the real part and

$$h_0(\alpha, z) = \Re \left[\ln \left(\frac{2\alpha + h_1(\alpha, z)}{2\alpha - h_1(\alpha, z)} \right) \right] \quad (1.67)$$

and finally

$$\begin{aligned} H_0(\alpha, z) = & -\frac{3}{8}z^2 \left(1 - \frac{1}{16}z^2\right) h_0(\alpha, z) + \\ & \left(1 - \frac{3}{8}\alpha + \frac{1}{64}\alpha^3 + \frac{3}{128}\alpha z^2\right) h_1(\alpha, z). \end{aligned} \quad (1.68)$$

The un-normalised SESANS correlation function $G^*(z)$ can be calculated from the individual contributions of each layer i with layer j , weighted respectively with w_i and w_j ,

$$G^*(z) = \frac{4}{3}\pi \sum_{i=1}^N w_i^2 R_i^4 H_0\left(2, \frac{z}{R_i}\right) + 2 \sum_{i=1}^{N-1} \sum_{j=i+1}^N w_i w_j \mathcal{P}(R_i, R_j, z) \quad (1.69)$$

and

$$G^*(0) = 2\pi \sum_{i=1}^N w_i^2 R_i^4 + 2\pi \sum_{i=1}^{N-1} \sum_{j=i+1}^N w_i w_j \times \left[R_i R_j (R_i^2 + R_j^2) \frac{1}{2} (R_i^2 - R_j^2)^2 \ln \frac{R_i + R_j}{|R_i - R_j|} \right]. \quad (1.70)$$

The projection of $\gamma(r)$ expressed in the normalised form is

$$G(z) \equiv G^*(z)/G^*(0) \quad (1.71)$$

A special, relevant case of the above formalism is the spherical shell, i.e., with $N = 2$ and $R_i = R_{\text{in}} < R_j = R_{\text{out}}$ Fig. 1.9 shows the result for a shell with $R_{\text{in}}/R_{\text{out}} = 0.9$ (the ratio between the inner and outer radius). The two regions $z < 2R_{\text{in}}$ and $z > 2R_{\text{in}} - R_{\text{out}}$ are both due to inter shell correlations (equivalent to correlating a sphere of radius R_{out}) and the region between is intra shell correlations, which scale as r^{-1} due to the 2D nature of a shell (r^{d-3}). A decaying linear region is observed when plotting $G(z)$ vs $\log(z)$, the slope is decaying with decreasing shell thickness, see Fig1.10.

The correlation length ξ for a spherical shell is

$$\xi = R_{\text{out}} \left(\frac{3(1-s)}{2(1-s^3)} + \frac{3(1-s^2)^2}{4} \ln \left(\frac{1+s}{1-s} \right) \right), \quad (1.72)$$

with $s = R_{\text{in}}/R_{\text{out}}$, meaning that the polarisation saturation level Eq. (1.23) will be highly sensitive to s .

Some illustrative examples can be found in [11]. They calculated $G(z)$ for shells and multi-shells numerically, using inverse Fourier transformation.

The density distribution for thick $s < 0.5$ hollow spheres can be approximated by a Gaussian function

$$\rho(r) = \frac{1}{\pi^{3/2} \left(\frac{3}{2}\right)_p} e^{-r^2} r^{2p}, \quad (1.73)$$

where $(x)_p$ is the Pochhammer symbol and $p = 0, 1, 2, \dots, \infty$ has the effect of sharpening the shell so that zero correspond to filled and higher values to thinner shells. The Fourier spectrum of $\rho(r)$, its power spectrum $I(q)$, autocorrelation function $\gamma(r)$ and $G(z)$ can be analytically calculated using Computer Algebra Systems, such as Mathematica.

1.6.3 Ellipsoids and Spheroids

The ellipsoid is a sphere that has been scaled by a factor along each orthogonal axis and finding the autocorrelation function of the ellipsoid involves averaging over all azimuthal and polar angles. The correlation function for an ellipsoid with semi-axes a ,

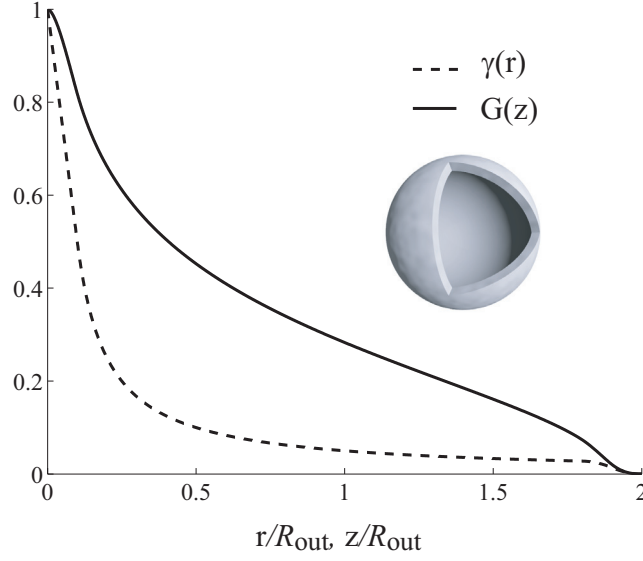


Figure 1.9: $\gamma(r)$ (dashed line) and its projection $G(z)$ (solid line) for a spherical shell with $s = R_{\text{in}}/R_{\text{out}} = 0.9$

b and 1 is

$$\gamma(r, a, b) = \frac{2}{\pi r^2} \int_0^{\pi/2} d\theta \sin \theta \int_0^{\pi/2} \frac{1}{f_{\theta, \varphi}(a, b)} P\left(\frac{r}{f_{\theta, \varphi}(a, b)}\right) d\varphi, \quad (1.74)$$

where $f_{\theta, \varphi}(a, b) = \sqrt{[a^2 \cos^2(\varphi) + b^2 \sin^2(\varphi)] \sin^2(\theta) + \cos^2(\theta)}$, which represents distances in spherical coordinates after the scaling. $P(x) = x^2 - 3/4x^3 + 1/16x^5$ for $x < 2$ is the probability distribution function of distances inside a sphere of unit radius. The double integral has to be solved numerically, and after this one obtains $G(z)$ by a second numerical integration according to Eq. (1.8).

The ellipsoid is called a spheroid when $a = b$ and when $a > 1$ it is called an oblate (membrane) spheroid and $a < 1$ produces a prolate spheroid (needle). This simplifies the problem and produces an analytical solution for the correlation function [25]. The oblate case ($a > 1$) yields after normalisation

$$\gamma(r) = \begin{cases} 1 - \frac{3r}{8} + \frac{r^3}{64} + \frac{3r^3}{128} - \frac{3r \ln(a + \sqrt{a^2 - 1})}{8a\sqrt{a^2 - 1}} + \frac{3r^2 \ln(a + \sqrt{a^2 - 1})}{128a\sqrt{a^2 - 1}}, & r < 2 \\ \frac{3\sqrt{4a^2 - r^2}}{8r\sqrt{a^2 - 1}} + \frac{3r\sqrt{4a^2 - r^2}}{64a^2\sqrt{a^2 - 1}} - \frac{3r \ln(U)}{8a\sqrt{a^2 - 1}} + \frac{3r^3 \ln(U)}{128a^3\sqrt{a^2 - 1}}, & 2 < r < 2a, \end{cases} \quad (1.75)$$

where $U = ar^{-1}(2 + \sqrt{4 - (r/a)^2})$. For the prolate case when $a < 1$ it is again possible to write $\gamma(r)$ in terms of elementary functions, but these will not be shown here due to

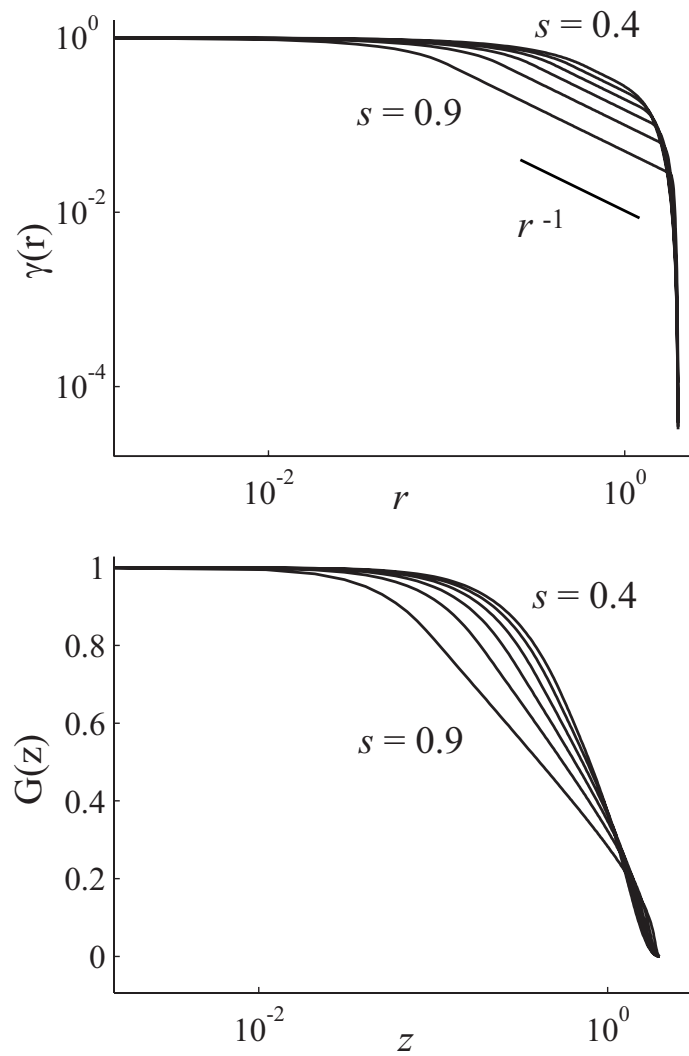


Figure 1.10: $\log[\gamma(r)]$ vs $\log(r)$ and its projection $G(z)$ plotted as a function of $\log(z)$ for $s = 0.4, 0.5, 0.9$.

their length. The integrals, in the two domains, to be solved in the prolate case are

$$\gamma(r) = r^{-2} \times \begin{cases} \int_0^1 dx \frac{1}{\sqrt{a^2 + (1-a^2)x^2}} P\left(\frac{r}{\sqrt{a^2 + (1-a^2)x^2}}\right), & r < 2a \\ \int_s^1 dx \frac{1}{\sqrt{a^2 + (1-a^2)x^2}} P\left(\frac{r}{\sqrt{a^2 + (1-a^2)x^2}}\right), & 2a < r < 2, \end{cases} \quad (1.76)$$

where the lower bound $s = \sqrt{\frac{4a^2-r^2}{4a^2-4}}$ is given by the condition that $x < 2$ in $P(x)$ above. The previous expression for the oblate case is the solution to the same integrals, but in the domains $r < 2$ and $2 < r < 2a$, and with the integration boundary going from zero to s .

1.6.4 Infinitely long Cylinder with diameter D

The correlation function $\gamma(r)$ for a right and infinitely long cylinder with a diameter D is [27]

$$\gamma(r) = \begin{cases} 1 - \frac{{}_2F_1\left(\frac{1}{2}, \frac{3}{2}; 3; \frac{r^2}{D^2}\right)r^3}{4D^3} - \frac{{}_2F_1\left(-\frac{1}{2}, \frac{3}{2}; 2; \frac{r^2}{D^2}\right)r}{D}, & 0 \leq r < D \\ 1 - \frac{{}_2F_1\left(\frac{1}{2}, \frac{3}{2}; 3; \frac{D^2}{r^2}\right)D^2}{4r^2} - 2 F_1\left(-\frac{1}{2}, \frac{3}{2}; 2; \frac{D^2}{r^2}\right), & D < r < \infty \end{cases} \quad (1.77)$$

Where ${}_2F_1$ is the Hypergeometric function. We are unable to solve the projection $G(z)$ analytically but present a numerical solution in Fig. 1.11. The correlation function $\gamma(r)$ and $G(z)$ show a levelling decay saturating, not surprising, around D on the horizontal axis.

1.6.5 Cube and cuboid

The autocorrelation function for both the cube and the cuboid is known analytically [31], [26] and the corresponding projection can be evaluated numerically as will be shown in Sec. 1.6.8.

1.6.6 Ideal Polymer

A polymer chain can in certain cases be approximated as a random walk, this is called an Ideal Polymer or a polymer in theta condition. The approximation neglects any interaction or excluded volume among the monomers. The coil is made up of N uncorrelated monomers of length a_0 with a radius of gyration of

$$R_g = \sqrt{\frac{N}{6}} a_0. \quad (1.78)$$

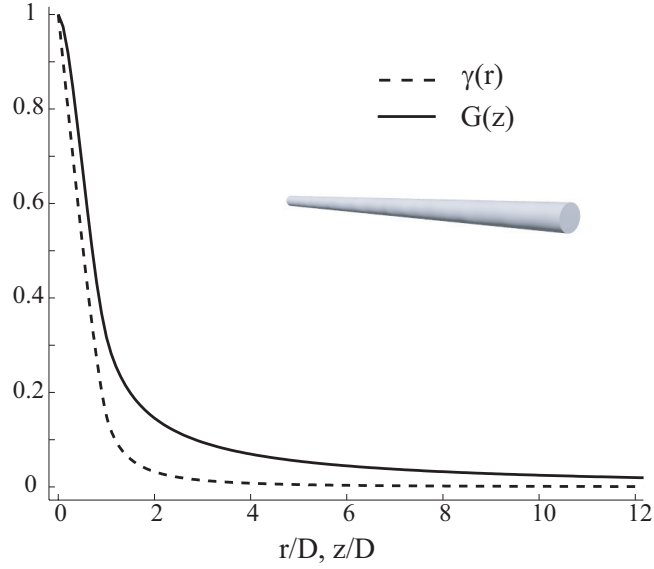


Figure 1.11: $\gamma(r)$ (dashed line) and its projection $G(z)$ solved numerically (solid line) for a infinitely long cylinder with diameter D .

Debye [18] calculated the Fourier transform of the autocorrelation of the Ideal Polymer:

$$I(q) = \frac{e^{-q^2 R_g^2} - 1 + q^2 R_g^2}{q^4 R_g^4}. \quad (1.79)$$

This formulation neglects the size of the monomer, thus $a_0 = 0$. The inverse transformation is

$$\gamma(r) \propto \frac{(r^2 + 2R_g^2)\text{erf}\left(\frac{r}{2R_g}\right)}{rR_g} - e^{-\frac{r^2}{4R_g^2}}, \quad (1.80)$$

where erf is the Error function. The projection can be expressed in terms of Exponential integrals (E_n -function).

$$G(z) \propto E_1 \left[\left(\frac{r}{2R_g} \right)^2 \right] - E_2 \left[\left(\frac{r}{2R_g} \right)^2 \right], \quad (1.81)$$

for $z \geq a_0$. For $R_g \gg z$ and $z > a_0$ the following relation is obtained

$$G(z) \propto -\ln \left(\frac{z}{2R_g} \right). \quad (1.82)$$

Thus, as expected for a random walk in 3D, the Ideal Polymer has the same scaling as a 2D structure (see Eq. (1.48)).

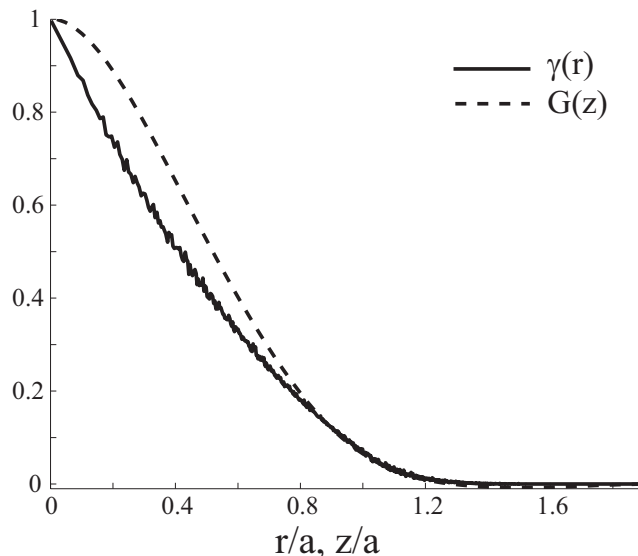


Figure 1.12: $G(z)$ and $\gamma(r)$ calculated numerical for a cube of size a . The largest correlating size of a cube is $\sqrt{3}a$ and the correlation length is found to be $\xi \simeq 0.9a$.

1.6.7 Taking a size-distribution (polydispersity) into account

Given that there is no interaction between particles (i.e., dilute samples and no long-range potentials) it is possible to weigh $\gamma(r)$ and $G(z)$ with a size distribution function. Such approach was applied on measurements of microemulsions [30]. For poly-disperse samples the projection becomes

$$G(z) = \int_0^{\infty} G(z, a)P(a)da \quad (1.83)$$

and

$$\xi = \int_0^{\infty} \xi(a)P(a)da. \quad (1.84)$$

Where $P(a)$ is the normalised probability distribution for the occurrence of size a , commonly Gaussian or log-normal distributed. It is important to carefully consider the upper integration boundary in the integrals, so that the “whole” distribution $P(a)$ is used (the boundary, strictly ∞ , depends on distribution widths, expectance values etc.).

1.6.8 Numerical calculations on isolated shapes

Finding an analytical solution to the spherically averaged autocorrelation $\gamma(r)$ of a 3D density distribution can be a formidable task. We are, however, able to solve this problem numerically, which is best done in the wave number domain. After constructing the density distribution $\rho(x, y, z)$ the Fourier spectrum of $\rho(x, y, z)$ is calculated by

using 3D Fast Fourier Transform (FFT); this result is then multiplied with its complex conjugate to yield $I(q)$ after which $\gamma(r)$ is calculated by inverse FFT of $I(q)$. $G(z)$ can be calculated with either Eq. (1.14) or Eq. (1.8).

Fig. 1.12 shows $\gamma(r)$ for a cube with side a , here the correlation length is calculated to be $\xi/a = 0.92$ (mean chord length inside the cube). The longest possible correlation in a cube is $\sqrt{3}a$ and that is the point where no more correlations are seen.

A spheroid is given by $(x/a)^2 + (y/a)^2 + (z/b)^2 = 1$. The spheroid is oblate if $a > b$, prolate when $a < b$ and spherical when $a = b$. In Fig. 1.13 the numerical results for the three cases are shown, the horizontal axis is scaled with the largest radius present in the spheroid. An aspect ratio of $a/b = 1.5$ was used for the oblate case and the inverse for the prolate case. The correlation lengths were calculated for the prolate, oblate and the sphere to be $\xi_p/(2R) = 0.57$, $\xi_o/(2R) = 0.65$, $\xi_s/(2R) = 0.76$.

The examples given here could be solved partly analytically according to Eq's. (1.76) and (1.75) for the ellipsoid and the result found in [31] for the cube example. The method described here is more natural for complicated shapes and other numerical density distributions, see for instance Sec. 1.5.3.

1.7 Packings of Hard-Spheres

For monodisperse assemblies of hard spheres with radius R one usually introduces the pair correlation function $g(r)$ where non-interacting dilute hard spheres give $g(r) = 1$, but in concentrated samples one observes deviations in $g(r)$ due to the excluded volume between hard cores. Longer ranged potentials could lead to excluded volume, clustering etc., which manifests in correlations between particles. Thus, the pair correlation function gives insight into the interactions between particles and is especially useful for assemblies of monodisperse spheres.

The pair correlation function is the probability of finding a particle center-of-mass at a certain distance \mathbf{c} away from the origin, given that there is a particle at the origin. For N particles in a volume V , isotropically distributed, with their center-of-mass separated by a distance \mathbf{c}_{ij} the pair correlation function is as a function of distances c

$$g_2(c) = \frac{V}{N^2 4\pi c^2} \left\langle \sum_{i=1}^{N-1} \sum_{j=i+1}^N \delta(c - c_{ij}) \right\rangle, \quad (1.85)$$

where $\delta(c - c_{ij})$ is the Dirac delta function. For the hard sphere system, this function is zero when $c < 2R$ and if there is no long-range ordering one expects $g_2(\infty) = 1$. The N particles are forming $N(N - 1)/2$ pairs, making $g_2(c)$ readily calculated on numerical data. The pair correlation function can be used in order to calculate $\gamma(r)$ and $G(z)$ (see in Sec. 1.7.1).

Assuming isotropic distributions, the autocorrelation function of the density distribution can be separated into contributions from pair density-correlations $C_2(r)$, found

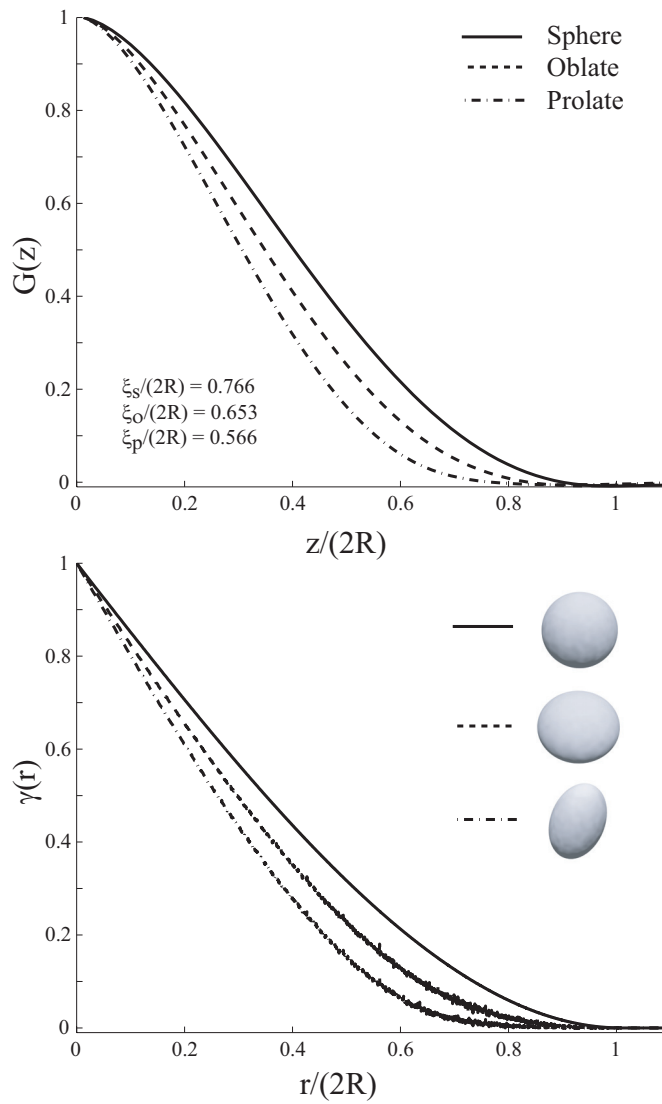


Figure 1.13: $G(z)$ (top figure) and $\gamma(r)$ (bottom figure) calculated numerically for an oblate, prolate and a spherical spheroid. The horizontal axis is scaled with the largest radius of the spheroid.

by correlating all distances r_{ij} separating the pairs,

$$C_2(r) = \langle \rho(0)\rho(r_{ij}) \rangle_V, \quad (1.86)$$

and secondly the density correlations within the isolated particle $C_1(r)$, found by correlating distances r_i within the particles

$$C_1(r) = \langle \rho(0)\rho(r_i) \rangle_V = \phi\gamma_1(r), \quad (1.87)$$

where $\gamma_1(r)$ is the autocorrelation function of the isolated particle shape (see Sec. 1.6).

The density-density correlation function is then the sum of the two contributions.

$$C(r) = C_1(r) + C_2(r) - \phi^2, \quad (1.88)$$

where $C_1(0) = \phi$, $C_1(\infty) = 0$, $C_2(0) = 0$ and $C_2(\infty) = \phi^2$ giving the mean square fluctuation $C(0) = \phi(1 - \phi)$. And finally the normalised correlation function is

$$\gamma(r) = \frac{C(r)}{C(0)}, \quad (1.89)$$

For hard spheres, $C_2(r)$ can be expressed in terms of the pair correlation function [46], i.e.,

$$C_2(r) = \frac{1}{V} \int \gamma_1^D(r, c) g_2(c) c^2 dc. \quad (1.90)$$

Where $\gamma_1^D(r, c)$ is the autocorrelation of a dumbbell [28]. In other words $\gamma_1^D(r, c)$ gives the pair density-correlation and $g(c)c^2$ is its probability distribution in the volume V .

1.7.1 The pair correlation function and $G(z)$

$G(z)$ is related to the pair correlation function through Eq. (1.88), Eq. (1.89) and Eq. (1.8). For distributions of equal sized spheres $G(z)$ and ξ can be calculated from analytical $\gamma_1(r)$ and $\gamma_1^D(r, c)$ when the pair correlation function is known. This can be generalised for polydisperse assemblies of spheres, since the autocorrelation function of a dumbbell with two unequal sized radii is known [28].

Fig. 1.14 shows $C_2(r)$, $C_1(r)$, $C(r)$ and $\xi G(z)$ for a hard sphere fluid with a particle radius $R = 1/2$ and packing fraction $\phi = 0.25$. The Percus-Yevick approximation [59], [74] for a hard sphere fluid was used to calculate $g_2(r)$.

The projection makes excluded volume peaks become more pronounced as compared to $\gamma(r)$, making SESANS particularly useful to study ordering in hard sphere systems as can be seen in [45].

The correlation length for a hard sphere fluid will decrease with increasing packing fraction and therefore increase the saturation level in a SESANS experiment. The maximum amount of scattering is found around $\phi = 1/3$, see Fig. 1.15.

These calculations can be done in the wavenumber domain using the form factor $P(q)$ and the structure factor of the distribution. The Fourier transformation of $\gamma_1(r)$

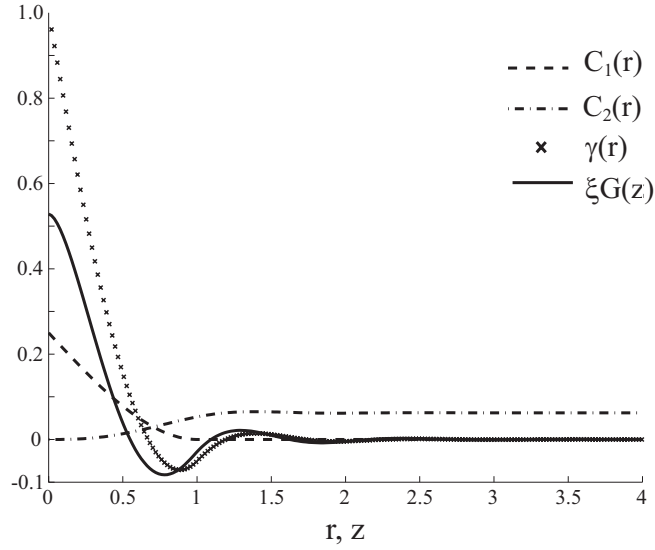


Figure 1.14: $C_1(r)$, $C_2(r)$, $C(r)$ and $\xi G(z)$ for a hard sphere fluid calculated with the Percus-Yevick approximation using $\phi = 0.25$ and $R = 1/2$.

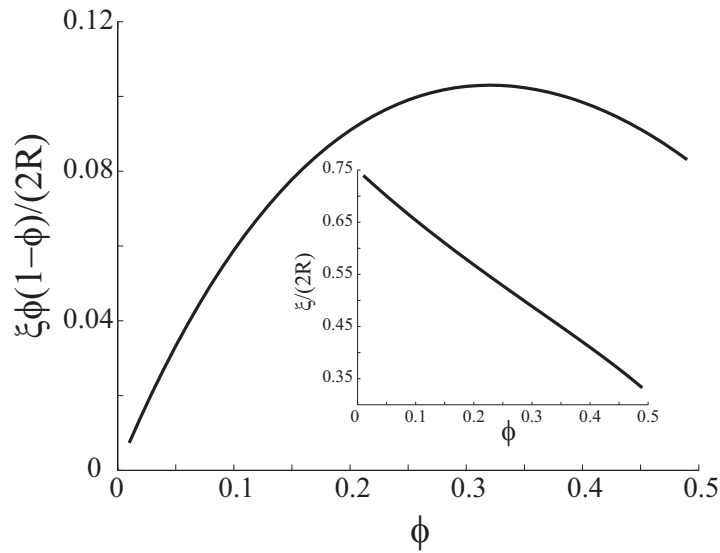


Figure 1.15: $\xi\phi(1-\phi)$ plotted as a function of hard sphere packing fraction ϕ for a hard sphere fluid with $\phi = 0.49$ and $R = 1/2$ in the Percus-Yevick approximation. The inset shows the correlation length $\xi/(2R)$ as a function of ϕ .

and $\gamma_2(r)$ is the form and structure factor respectively. The product of the two yields $I(q) = P(q)S(q)$ and $G(z)$ can be calculated by the Hankel transformation in Eq. (1.14).

SESANS measurements on the structural transitions in hard-sphere colloid dispersions illustrate the significance of ordering when transition occurs from gaseous to liquid and solid (glassy) state [44].

1.8 Oriented anisotropic samples

Anisotropy in the density distribution of a sample can be studied with SESANS provided that the sample can be rotated. Writing the projection and the correlation length in Cartesian coordinates yields again

$$G(z) = \frac{2}{\xi} \int_0^\infty \gamma(x, 0, z) dx. \quad (1.91)$$

and

$$\xi = 2 \int_0^\infty \gamma(x, 0, 0) dx. \quad (1.92)$$

The projection is along x (i.e., the neutron beam is along x). Note again that SESANS has no sensitivity along the y direction.

The final level of polarisation Eq. (1.23) is proportional to ξ , meaning that the end level of the polarisation, for an anisotropic sample, depends on how the sample is oriented in the beam. The shape of the curve will depend on the microstructure along the z coordinate (see Fig. 1.2).

1.8.1 The oriented right cylinder

The correlation function of a disk with diameter D in 2-dimensions is

$$\gamma_c(r) = \begin{cases} \frac{2}{\pi} \left(\cos^{-1} \left(\frac{r}{D} \right) - r \frac{\sqrt{D^2 - r^2}}{D^2} \right) & \text{if } r \leq D \\ 0 & \text{otherwise,} \end{cases} \quad (1.93)$$

with $r = \sqrt{x^2 + z^2}$, (Eq. (1.93) gives the mean intersecting area between two disks of equal diameters separated by a distance r). Consider the cylinders illustrated in Fig. 1.16, here it is possible to separate the correlations across the diameter of the cylinder from correlations along its length L . The total correlation function is the product of the two. For example, when $r \leq D$ and $y \leq L$:

$$\gamma(r, y) = \frac{2}{\pi} \left(\cos^{-1} \left(\frac{r}{D} \right) - \frac{r \sqrt{D^2 - r^2}}{D^2} \right) \left(1 - \frac{y}{L} \right), \quad (1.94)$$

which is the case when the cylinder-face is in the xz -plane and the side is parallel to y (see Fig. 1.16). For a cylinder with its side parallel to the z -coordinate and its face in

the xy -plane (denoted i in Fig. 1.16) gives according to Eq. (1.91) and after shifting coordinates in Eq. (1.94) so that $r = \sqrt{(x^2 + y^2)}$ and $y = z$ yields for $z \leq L$

$$G(z) = 1 - z/L. \quad (1.95)$$

Integrating to the diameter D of the cylinder in Eq. (1.92) yields the correlation length

$$\xi = 2 \int_0^D \gamma_c(x) dx = \frac{8D}{3\pi}, \quad (1.96)$$

which is the average length of a all chords drawn inside a disk of diameter D .

Having the cylinders side parallel to y and its diameter in the xy -plane (denoted ii in Fig. 1.16), yields for $z \leq D$

$$G(z) = \int_0^D \gamma_c(\sqrt{x^2 + z^2}) dx \quad (1.97)$$

and again the correlation length is $\xi = \frac{8D}{3\pi}$.

If the cylinder is oriented with its side along x and its face in the zy -plane, the projection along x becomes for $z \leq D$

$$G(z) = \gamma_c(z) \quad (1.98)$$

and the correlation length is in this case

$$\xi = 2 \int_0^L \left(1 - \frac{x}{L}\right) dx = L. \quad (1.99)$$

This configuration is denoted iii in Fig.1.16. $G(z)$ for the three different orientations is also plotted in Fig. 1.16. The plot shows three distinct curve shapes having two different end levels in $P(z)$ given by Eq. (1.21) and Eq. (1.23).

Note that if the cylinders revolve around the x -axis, then the first two cases (i and ii) would be symmetric in the yz -plane, giving an identical projection $G(z)$.

1.8.2 The oriented Gaussian spheroid

The correlation function for an ellipsoidal Gaussian distribution can be written as

$$\gamma(r) = e^{\left(-\sqrt{x'^2/a^2 + y'^2/b^2 + z'^2/c^2}\right)^2}, \quad (1.100)$$

where the prime distinguishes the ellipsoid's coordinate frame of reference. The spheroid, a special case, has two of its radii equal, i.e., $a \neq b = c$. For an oblate spheroid its axes are $a < b = c$ and for the prolate spheroid this becomes $a > b = c$. Orienting the spheroid in the SESANS coordinate system gives three distinct cases:

$$\xi G(z) = \begin{cases} ae^{-(z^2/b^2)} & \text{if } x \parallel x' \ \& \ z \parallel (z', y') \\ be^{-(z^2/a^2)} & \text{if } x \parallel (z', y') \ \& \ z \parallel x' \\ be^{-(z^2/b^2)} & \text{if } (x \parallel z' \ \& \ z \parallel y') \ \text{or } (x \parallel y' \ \& \ z \parallel z') \end{cases} \quad (1.101)$$

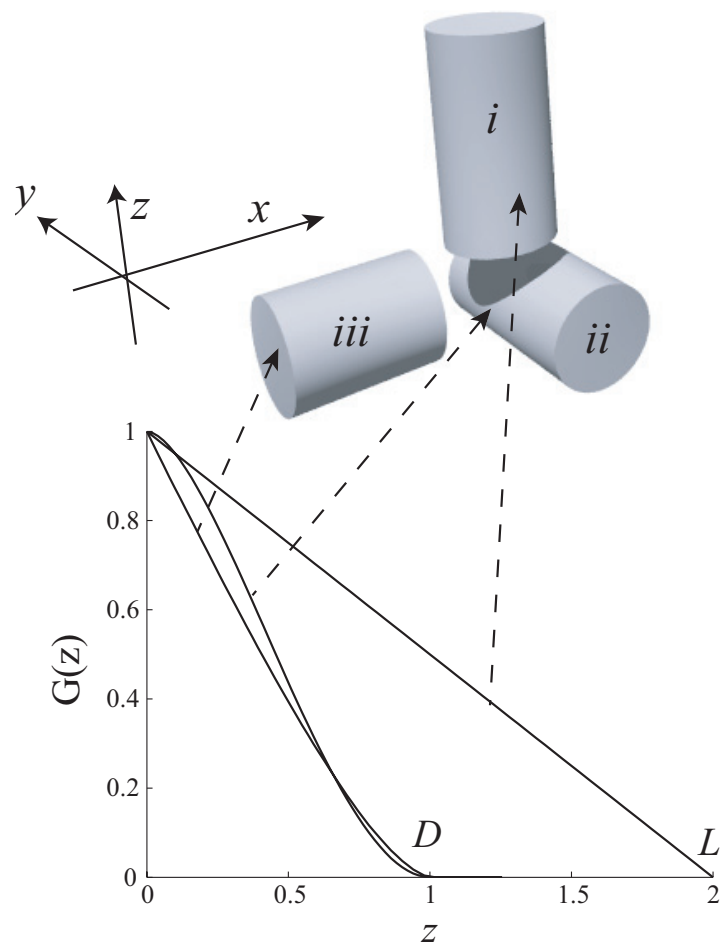


Figure 1.16: An oriented cylinder in cartesian coordinates, where z is the correlation direction and the projection is taken along the x coordinate. D denotes the diameter of the cylinder and L is its length.

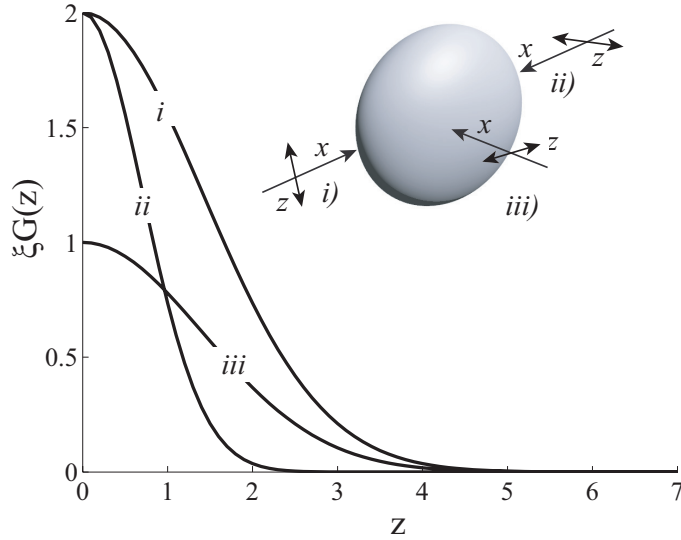


Figure 1.17: $\xi G(z)$ plotted for three distinct sample orientations; (i) has a long side parallel to both x and z ; (ii) is with the long side parallel to x and the short side parallel to z ; (iii) has the long side parallel to z and x is along the short side.

where \parallel denotes being parallel oriented. Thus, a SESANS experiment on aligned spheroids can discriminate between oblate and prolate cases and it would be possible to determine the aspect ratio a/b of the distribution. Performing the experiment suggested by Eq. (1.101), would for the oblate case give one curve with a typically high polarisation end level and two curves with equal but lower levels (vice versa for the prolate case).

Fig. 1.17 shows the oblate case and plots $\xi G(z)$ for three orientations indicated by the inset. Here it is evident that, depending on orientation, more scattering and therefore more depolarisation (Eq. (1.23) and Eq. (1.21)) is expected when the long axis of the spheroid is oriented parallel to the neutron beam, indicated by i and ii in Fig. 1.17. The width of the curve becomes more narrow when correlations are sampled across the shorter axis, as seen in configuration ii , conversely a wider curve saturating at larger length scales is seen when the density distribution is probed over the longer axis in i and iii .

The aspect ratio of the structure can be determined by comparing the correlation lengths in the various orientations.

1.9 Grating, oriented periodic beams

Oriented periodic beams, also shown in Fig. 1.18, offer a good way of illustrating the principles of neutron scattering instruments [37]. SESANS has been applied on a silicone grating in order to illustrate the technique in [13, 78] and theory [17]. The autocorrelation function of such a distribution (square wave), if taken across the ridges,

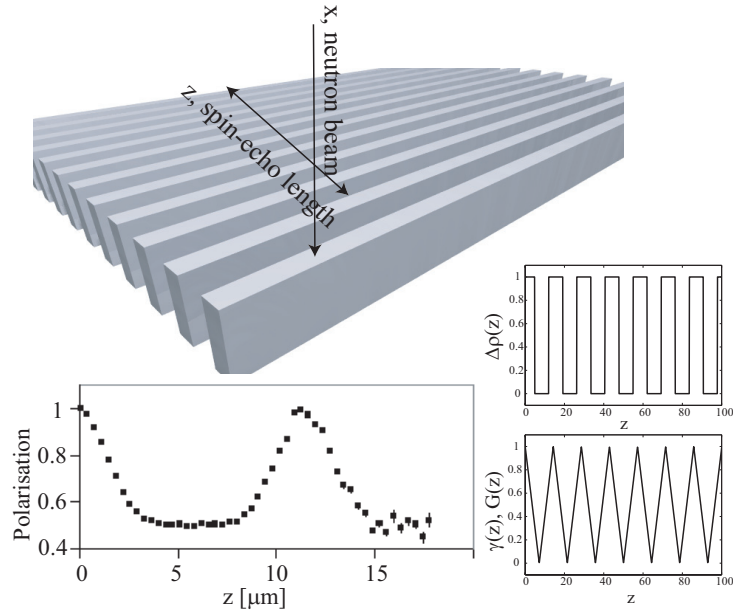


Figure 1.18: The autocorrelation function of a square wave is a triangle function and if oriented as illustrated in the top figure, then $G(z) = \gamma(r)$. For oriented beams (grating) the SESANS signal will be given by such triangle function with a correlation length ξ equal to the size of the ridges in the beam direction, this has been illustrated in an experiment shown here in the left figure at the bottom.

is a triangle function. When the measurement is performed with the beam parallel to the ridges, then the correlation length ξ will be equal to their length.

The actual SESANS measurement, shown in Fig. 1.3 and repeated below in Fig. 1.18, shows that the ridges that make up the grating were slightly trapezoidal in shape, which gives rise to a smoother correlation function. Note also that there is no difference in the shape between $\gamma(z)$ and $G(z)$, this because correlations along x and z can be separated in this geometry.

1.10 Summary and concluding remarks

The analysis of Spin-echo small-angle neutron scattering measurements has been discussed and a toolkit for analysing SESANS data has been developed. Theoretical, phenomenological, model free as well as visual ways of interpreting and modelling SESANS measurements have been presented. Once the autocorrelation of the density distribution or its Fourier transform is known, the corresponding SESANS correlation function can be calculated through the real-space projection of the correlation function $\gamma(r)$ or by performing the Hankel transformation of the Fourier power spectrum $I(q)$. The relation between the transformations and their inverse $\gamma(r)$, $I(q)$ and $G(z)$ has been presented.

In general, the width of the polarisation versus spin-echo length plot represents the

size of the heterogeneities making up the measured structure. Further more, the final polarisation transmission or the level at which the polarisation saturates depends on the packing fraction, chemical composition and the correlation length of the sample inhomogeneities. The relationship between the SESANS measured quantities and the ones usually extracted from SANS data has been presented.

For isolated geometries, so called form factors measured in dilute samples, the correlation function can be expressed as an analytical function or by means of numerical calculations best done in the wavenumber domain. Models describing random and fractal media have been translated into the SESANS language, being particularly useful since the materials characterised by the SESANS accessible length scales often fall in these random-disordered categories. Packings of equal sized hard spheres, at higher volume fractions, show oscillations in the correlation function due to excluded volume among the spheres. This ordering can be studied with SESANS and it was illustrated using the Percus Yevick approximation for the hard sphere liquid.

1.11 Acknowledgements

We thank M. Trinker, E. Jericha and H. Rauch, Atominstitut, Vienna University of Technology for lending us the silicon gratings. We thank C.P. Duif and J. Plomp for performing some of the SESANS-measurements. This work is part of the research programme of the 'Stichting voor Fundamenteel Onderzoek der Materie (FOM)', which is financially supported by the 'Nederlandse Organisatie voor Wetenschappelijk Onderzoek (NWO)'.

Chapter 2

Stress, strain and bulk microstructure in a cohesive powder

This article, By Robert Andersson, Wim G. Bouwman, Stefan Luding and Ignatz M. de Schepper, appeared in the scientific journal: Physical Review E 77, 051303 (2008).

Abstract

Spin-echo small-angle neutron scattering is able to characterise powders in terms of their density-density correlation function. Here we present a micro-structural study on a fine cohesive powder undergoing uniaxial compression. As a function of compression we measure the autocorrelation function of the density distribution. From these measurements we quantify the typical sizes of the heterogeneities as well as the fractal nature of the powder packing. The fractal dimension increases with increasing stress, creating a more space-filling structure with rougher phase boundaries. The microscopic stress-strain relation showed the same nonlinear behaviour as the macroscopic relation. In this way it was possible to link the macroscopic mechanical response with the evolution of microstructure inside the bulk of the cohesive powder. The total macroscopic compressive strain is in agreement with a corresponding decrease in microstructural length scales.

2.1 Introduction

Rather than being driven by the hard-core exclusion between grains, the structure of cohesive powders is mainly determined by the van der Waals attraction amongst small primary particles ($<100\mu\text{m}$). As a result of these adhesive forces, and the irrelevancy of body forces, very loosely packed and fluffy structures are seen to form in these materials. The structures lead to process related issues relevant to industry in a sense that mass flows become unstable [76]. An increased demand for particulate materials on the nanoscale makes the understanding of this type of granular materials important.

To precisely understand the macroscopic behaviour of powders, the computer-modelling and theory-buildup needs the support of experiments on realistic samples. More specifically, there is a need for experiments that can quantify powders in terms of their microstructure. Experiments are needed that can look inside the “fluffy” structure of cohesive powders so that more quantitative statements can be made.

Extracting information from the bulk of powders and granular materials is difficult. The opacity and the wide range of sizes present in real materials renders most optical and conventional wave diffraction techniques more or less useless. The opacity can be overcome by using a penetrating radiation such as x-rays in x-ray tomography [5, 67, 71] or radio-waves in magnetic resonance imaging [70, 55].

Understanding macroscopic mechanical behaviour can be obtained by investigating the changes in crystallographic microscopic parameters [33]. Following the microscopic evolution by using penetrating radiation makes it possible to understand the macroscopic development from the microscopic point of view. Methods for studying the mechanical properties at the grain level of granular packings exist [50] and it is usually the buildup of force chains that is addressed. Neutron diffraction has been used to study non linear stress strain behaviour in granular materials [16].

In order to access the bulk of more realistic materials it becomes necessary to use penetrating radiation and a technique that has enough resolution to analyse the small-angle scattered radiation.

Spin-echo small-angle neutron scattering (SESANS) is a high resolution technique which measures the autocorrelation function of the sample density distribution in real space [12]. SESANS can be used to probe the structure across three orders of magnitude ranging from 30nm up to $20\mu\text{m}$, making it applicable to fine cohesive powders [1], colloidal systems [45], and dairy products [79], just to name a few.

The autocorrelation function of the density distribution $\gamma(r)$ can be used to characterise the microstructure of materials. This function is measured in a small-angle scattering experiment as its Fourier transform (the so-called structure or form factor). SESANS measures $\gamma(r)$ via its projection along the neutron beam path, making SESANS a real-space technique. The typical size, packing fraction, any anisotropy, scale invariance, ordering etc of the sample heterogeneities are examples of extractable sample properties.

A stress-strain measurement on a fine cohesive silica powder together with consec-

utive SESANS measurements has been performed and is reported in this paper. In the analysis, the cohesive powder is considered as being a self-affine random two-phase material. We use a model function for the density-density correlation function containing a typical size a of the structure and the so-called Hurst exponent H , related to the fractal dimension of the structure [41, 51]. The Hurst exponent depends on the phase boundary roughness, and the higher the degree of “surface roughness” the lower is the Hurst exponent.

From the initial decay of the measured SESANS curve it is possible to extract the unknown grain density and consequently the grain packing fraction. We find that the typical size of the inhomogeneities decays in a non linear way with increasing compressive strain and the microscopic stress-strain relationship shows the same exponential behaviour as the macroscopic stress-strain curve. The Hurst exponent is seen to decrease with increasing stress and strain, showing that a more space-filling structure with rougher interfaces is being formed as a function of compression. All-together, the study links the non-linear compressive stress-strain relationship to the evolution of microstructural parameters.

2.2 Microstructure and SESANS

2.2.1 Density distribution and its correlation function

The density distribution $\rho(r)$ in a heterogeneous two-phase sample is expected to fluctuate around its mean value. These fluctuations might be characterised by a typical size, anisotropy, being fractal or self-affine, regular (crystalline), random and so on. Taken all together, this is what we call the structure of a material. The structure of two phase systems such as a powder material can be analysed in terms of the autocorrelation function of its density distribution:

$$C(r) = \langle \Delta\rho(0)\Delta\rho(r) \rangle, \quad (2.1)$$

where the mean $\bar{\rho}$ has been subtracted [$\Delta\rho(r) = \rho(r) - \bar{\rho}$]. The mean square fluctuation is

$$C(0) = \Delta\rho_0\phi_1\phi_2, \quad (2.2)$$

where $\phi_1 + \phi_2=1$ are the packing-fractions of the two phases and $\Delta\rho_0 = \rho_1 - \rho_2$ is the solid-density difference between the two phases. The normalised (dimensionless) correlation function is

$$\gamma(r) = \frac{C(r)}{C(0)}. \quad (2.3)$$

The correlation function can be expressed in terms of the pair correlation function $g_2(r)$ [46]. $g_2(r)$ gives the probability of finding a particle centre of mass at a distance r away from an origin given that there is a particle at that origin. This function is especially useful for the study of monodisperse sphere packings. For spheres the correlation function becomes

$$\gamma(r) = \gamma_0(r) + 2 \int_0^\infty \gamma_D(r, c)g_2(c)c^2dc, \quad (2.4)$$

where $\gamma_D(r, c)$ is the autocorrelation of a pair of spheres separated by c [28] and $\gamma_0(r)$ is the autocorrelation function of a sphere.

The projection of $\gamma(r)$ is given by:

$$G(z) = \frac{2}{\xi} \int_z^\infty \frac{r\gamma(r)}{\sqrt{r^2 - z^2}} dr \quad (2.5)$$

and in Cartesian coordinates by

$$G(z) = \frac{1}{\xi} \int_{-\infty}^\infty \gamma(x, 0, z) dx. \quad (2.6)$$

The projection is made dimensionless with the correlation length of the density distribution [23]

$$\xi = \int_{-\infty}^\infty \gamma(r) dr, \quad (2.7)$$

so that $G(0) = 1$.

2.2.2 Spin-echo small-angle neutron scattering

Spin-echo small-angle neutron scattering (SESANS) is based on the Larmor-precession of neutrons in parallelogram shaped magnetic field regions [24], [66]. In SESANS, the polarisation of a neutron beam is measured, after transmission through a sample, as a function of the so-called spin-echo length ($30\text{nm} < z < 20\mu\text{m}$, set by the instrument user). The spin-echo length is a real-space parameter representing the size at which the correlations are measured (in the z -direction of the laboratory-coordinate system). In SESANS $G(z)$ is measured through the transmission of polarisation, normalised by experimental effects, as a function of z .

$$P(z) = e^{\Sigma_t[G(z)-1]}, \quad (2.8)$$

where

$$\Sigma_t = t\lambda^2 \Delta\rho_0^2 \phi_1 \phi_2 \xi. \quad (2.9)$$

Here t is the sample thickness, λ the neutron wavelength, and $\Delta\rho_0$ the neutron-scattering-length density difference in the sample (i.e., the contrast between the two phases in the sample). Note that Eq. (2.8) takes into account the effects of multiple scattering [65].

The correlation length ξ is measured along the neutron beam-axis of a SESANS experiment, which is perpendicular to the z direction. ξ is a measure of the width of the distribution $\gamma(r)$, which is in principle a measure of the size of the inhomogeneities in the sample (for a sphere the correlation length is 3/4 of the sphere-diameter). It can be interpreted as the mean-free-path of a neutron in the sample.

At large z (above the largest size describing the heterogeneities) one expects no more correlations [$G(\infty) = 0$], this gives a so-called saturation level of the polarisation:

$$P(\infty) = e^{-\Sigma_t}. \quad (2.10)$$

Thus, the logarithm of the polarisation at saturation is proportional to the correlation length ξ of the sample-inhomogeneities.

2.2.3 Correlation function of a random two-phase system

A cohesive powder is a particular case of a two-phase system that is heterogeneous at (most likely) many scales. The attractive forces between grains allow for the build up of connected networks and aggregates of low coordination number, resulting in large voids of air pockets and, in essence, low densities. In the end we have in mind a very porous material carrying a low packing fraction of grains that will be far from a random close packing of hard-spheres, or any other ordered density distribution.

For a perfectly random heterogeneous material made up of three-dimensional (3D) solids bounded by smooth 2D surfaces the density-density correlation function can be described by the so-called Debye-Andersson-Bueche (DAB) formalism [20, 19, 84]:

$$\gamma(r) = e^{-r/a}, \quad (2.11)$$

where a is a measure of the typical size of the heterogeneities. This function can be seen as a special case of the more general von Karman correlation function [35, 41]:

$$\gamma(r) = \frac{2}{\Gamma(H)} \left(\frac{r}{2a}\right)^H K_H\left(\frac{r}{a}\right), \quad (2.12)$$

where K_H is the second-order modified Bessel function and Γ is the Gamma function. For $H = 1/2$ this simplifies to the DAB formula in Eq. (2.11).

The so-called Hurst exponent $0 < H < 1$ is related to the dimensionality of the structure. The limits $H = 0$ and 1 correspond to a space filling and a smooth Euclidian distributions, respectively. In this context it is related to the interface roughness between the two phases making up the material. One usually discusses two domains $H > 1/2$ where the distribution is persistent and characterised by a certain degree of memory and longer-ranged correlations; and the domain $H < 1/2$ describing an anti-persistent distribution, governed by shorter-ranged correlations (i.e., rougher).

The Hurst exponent has been used to analyse the structure of shear bands [77] as well as for the study of percolation in porous materials [40] and in fracture profiles [6].

A 1D reconstruction of density distributions for various Hurst exponents can be seen in Fig. 2.1 below. This calculation is done in the wave number domain where a uniform deviate (white noise) is filtered with a spectral filter. The inverse Fourier transformation of the filtered white noise yields a real-space representation of the distribution. The spectral filter is the square root of the Fourier transformation of the autocorrelation function, in this case Eq. (2.15) below, (see also [41]).

The projection of Eq. (2.12) is found by insertion in Eq. (2.5), which leads too

$$G(z) = \frac{2}{\Gamma(H + 1/2)} \left(\frac{z}{2a}\right)^{H+1/2} K_{H+1/2}\left(\frac{z}{a}\right). \quad (2.13)$$

The corresponding correlation length for this density distribution will be:

$$\xi = \frac{2\sqrt{\pi}a\Gamma(H + 1/2)}{\Gamma(H)}. \quad (2.14)$$

In conventional small-angle neutron scattering one measures the Fourier transform of Eq. (2.12), which yields the normalised intensities as a function of wave number

$$I(q) = \frac{1}{[1 + (qa)^2]^{\frac{3}{2}+H}}. \quad (2.15)$$

2.3 Experiments and sample properties

A powder sample was kindly provided by Degussa (www.degussa.com). The product is called Sipernat-310, it is a synthetic-precipitated silica used in coatings, cosmetics, cements, rubbers, as filler etc. It is a typical cohesive powder containing fine grains

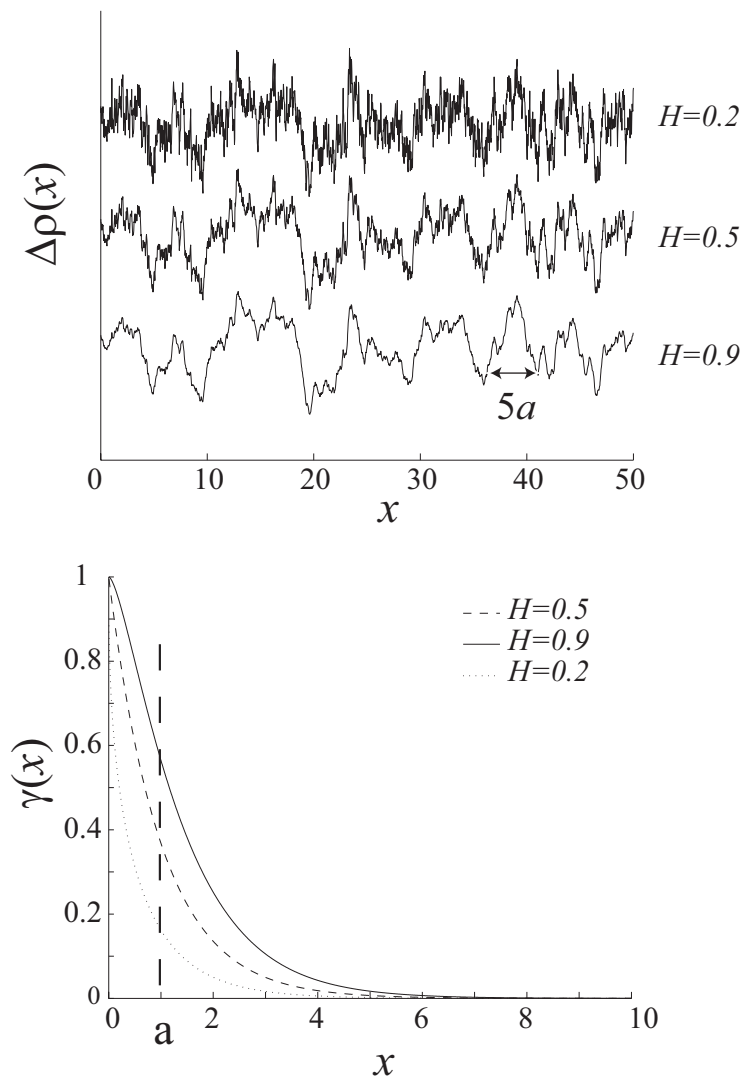


Figure 2.1: The top figure show examples of reconstructed 1D density distributions $\rho(x)$ based on the correlation function Eq. (2.12). The corresponding correlation functions are shown in the bottom figure. The characteristic size is here $a=1$

around $5\mu\text{m}$ in diameter. The sample was used without any further treatment, in ambient conditions.

We have used the SESANS setup at the Reactor Institute Delft (Delft University of Technology in the Netherlands) to perform the measurements. The instrument contains two parallelogram-shaped magnetic field regions with opposite magnetic induction directions (otherwise identical). The sample is positioned between the field regions. Any neutron scattering between the two fields will break the symmetry of the setup and cause the beam to depolarize. The strength of the field defines the so-called spin-echo length z , which is perpendicular to the beam direction and pointing in the direction of gravity. The polarisation of the neutron beam is measured as a function of z . The beam is nearly monochromatic with a wavelength of 0.21nm having a cross section at the sample position around 1cm^2 .

A simple uniaxial load-cell was used in order to measure the stress versus strain function of the powder (see Fig. 2.2). Strain is here defined as being the relative decrease in thickness of the sample

$$\delta t = 1 - \frac{t}{t_0}, \quad (2.16)$$

where t is the thickness after compressive straining and t_0 is the initial sample thickness. The stress and strain tester contains a cylindrical cavity with a movable hollow plunger that achieves the compression inside the cavity. The plunger was moved by a separate screwing action (without rotating the plunger) until a desired incremental strain was reached. We used nine increments of 0.25mm with an initial powder height of 6.5mm . The cylindrical cavity and the plunger are sealed off with aluminium windows (aluminium is virtually transparent to neutrons). The absolute stress was measured with Flexiforce load sensors provided by Tekscan (www.tekscan.com).

The initial powder packing is a very soft, low-density material and easily compacted (weakly aggregated). As seen in the stress-strain curve, which shows an exponential variation of stress as a function of strain in the probed interval (Fig. 2.3). The goal of this study is to understand this non linear stress-strain relationship through the bulk microstructure at each point of the stress-strain curve.

2.4 Results

2.4.1 First interpretation

When analysing the measurements it is often useful to interpret what we simply see by eye. In Fig. 2.4 the polarisation is plotted as a function of z . In total, ten measurements at ten different strain levels were carried out. The figure shows only four of the ten measurements for the sake of clarity.

Increasing the strain moves the saturation polarisation upwards, thus the upper curves correspond to higher stress and strain than the lower ones. Increasing the

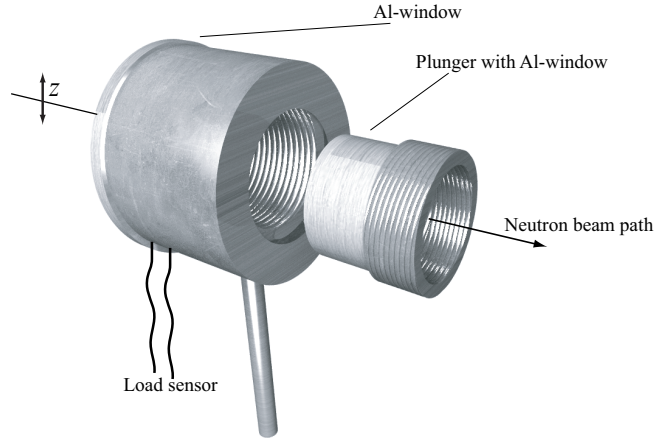


Figure 2.2: This figure is illustrating the load cell used in the stress-strain measurements on the cohesive powder. The initial height of the powder packing was 6.5mm and subsequently strained by nine increments of 0.25mm. The stress was measured using Flexiforce load sensors situated at the first Al-window.

strain makes the powder packing denser (ϕ) and thinner (t), both contributing to less scattering and higher polarisation saturation levels.

The second microstructural parameter contributing to the end level is the correlation length ξ . The rearrangement of particles into a denser state must decrease the size of the heterogeneities, giving rise to a lower correlation length with increasing strain.

At saturation we are able to read off the largest correlating size of the microstructure on the horizontal-axis. The measurement saturates around $5\mu\text{m}$, which is the size of grains making up the powder. Thus, no correlations are seen beyond the size of a grain.

The stress versus strain curve can be seen in Fig. 2.3. The curve shows that when plotting the logarithm of the stress versus strain a linear relationship is obtained. The powder in its native state is a very soft powder with low density stabilised by adhesive forces in the form of capillary and van der Waals forces. The hard-core exclusion between the silica grains finally governs the interaction between grains, as can be seen in the divergent behaviour of the applied stress for lower characteristic sizes (see the upper left plot in Fig. 2.6).

2.4.2 Linear initial slopes

The powder is composed of grains having an unknown solid density. The grain density will be lower as compared with the solid density of pure silica ($\rho_{\text{SiO}_2}=2.2\text{g/cm}^3$). From the grain density it is then possible to calculate the grain packing fraction ϕ_{grain} rather than the skeleton packing fraction ϕ_{sk} , which is calculated from solid silica density. To summarise:

$$\phi_{\text{sk}} = \frac{\rho_{\text{sample}}}{\rho_{\text{SiO}_2}} \quad (2.17)$$

and

$$\phi_{\text{grain}} = \frac{\rho_{\text{sample}}}{\rho_{\text{grain}}}. \quad (2.18)$$

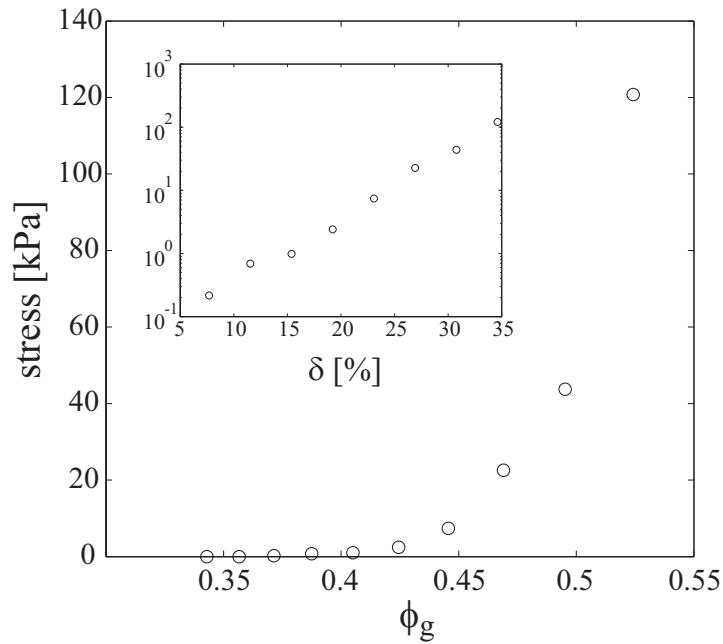


Figure 2.3: The stress versus grain packing-fraction ϕ_{grain} relationship for the Sipernat-310 powder. The inset shows a linear relationship between the logarithm of the stress versus strain δ . Note that the first two points yielded no measurable stress on the Flexiforce load sensors.

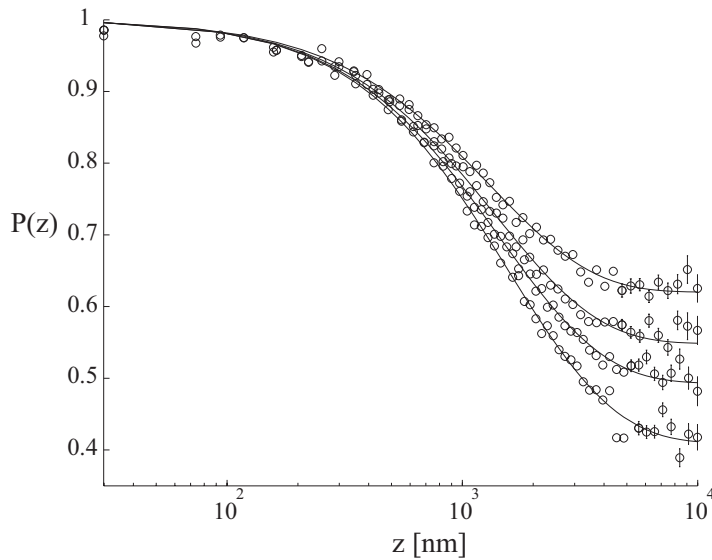


Figure 2.4: Polarisation plotted as a function of z . From top to bottom these measurements correspond to a uniaxial stress(strain) of 120kPa(35%), 7.4kPa(23%), 1kPa(15%) and 0kPa(3.8%). The full curves are fitted according to Eqs. 2.13,2.14 and 2.8. Unless shown, the error falls within the marker symbol

Where ρ_{sample} is the density of the powder packing and ρ_{SiO_2} is the solid density of pure silica.

The grain density and the grain packing fraction can be determined from the SESANS measurement by analysing the initial slope of the $P(z)$ vs z curves. The final amplitude of the polarisation (saturation level) is given by Eq. (2.10) and is read at a spin-echo length z related to ξ . Thus, the gradient of the initial part of $P(z)$ vs z yields a quantity that depends only on the sample-thickness, packing fraction ϕ and the scattering length density $\Delta\rho_0$. The slope is in a sense independent of structural arrangement of the density

$$-\frac{d\ln(P)}{dz} \simeq t\lambda^2\Delta\rho_0^2\phi(1-\phi). \quad (2.19)$$

Thus, division of the values of the slopes by the sample thickness and the primary particle packing-fraction ϕ_{grain} should yield a constant term for all experiments (see bottom right figure in Fig. 2.5), because straining the sample does not change $\Delta\rho_0$ or λ . We find the grain packing fraction ϕ_{grain} by fitting until a nearly constant term is found for all measurements. The grain density can then be found by using Eq. (2.18).

This analysis gives a density of $\rho_{\text{grain}}=1.1\text{g/cm}^3$ and packing fractions ranging from $\phi_{\text{grain}}=0.34$ up to $\phi_{\text{grain}}=0.53$ for the highest strain.

2.4.3 Curve shapes and their amplitudes

For a more complete analysis of the SESANS experiment we apply a model that describes an autocorrelation function of the density distribution. From that model we are able to calculate the corresponding projection as well as the expected polarisation-shapes and amplitudes.

The thickness t , packing fraction ϕ , and neutron wavelength λ are all known experimental parameters that contribute to the saturation level $P(\infty)$. The scattering length density $\Delta\rho_0$ is a constant parameter given by the chemical composition of the sample. Thus, in order for the model to be consistent it has to yield a constant scattering length-density for all ten measurements. In short, we have to find a model capable of describing $\gamma(r)$ as well as ξ in such a way that it produces the saturation level and curve shapes observed in the measurement.

To model the data we use the von Karman correlation function introduced in Sec. 2.2.3, which describes a statistical self affine density distribution according to Eqs: (2.12)-(2.14). The model explains the microstructure with two parameters, the Hurst exponent H and a characteristic size a of the density distribution. This yields, including experimental parameters, a scattering length density of about $1.1\times 10^{14}\text{m}^{-2}$ for all samples.

The model parameters measured at each incremental strain are plotted in Fig. 2.6. The characteristic size rapidly decreases with increasing strain before it saturates for strains larger than 20-25%. In order for the powder to be compressed the larger inhomogeneities, clusters and voids have to be broken and collapsed. This first stage occurs

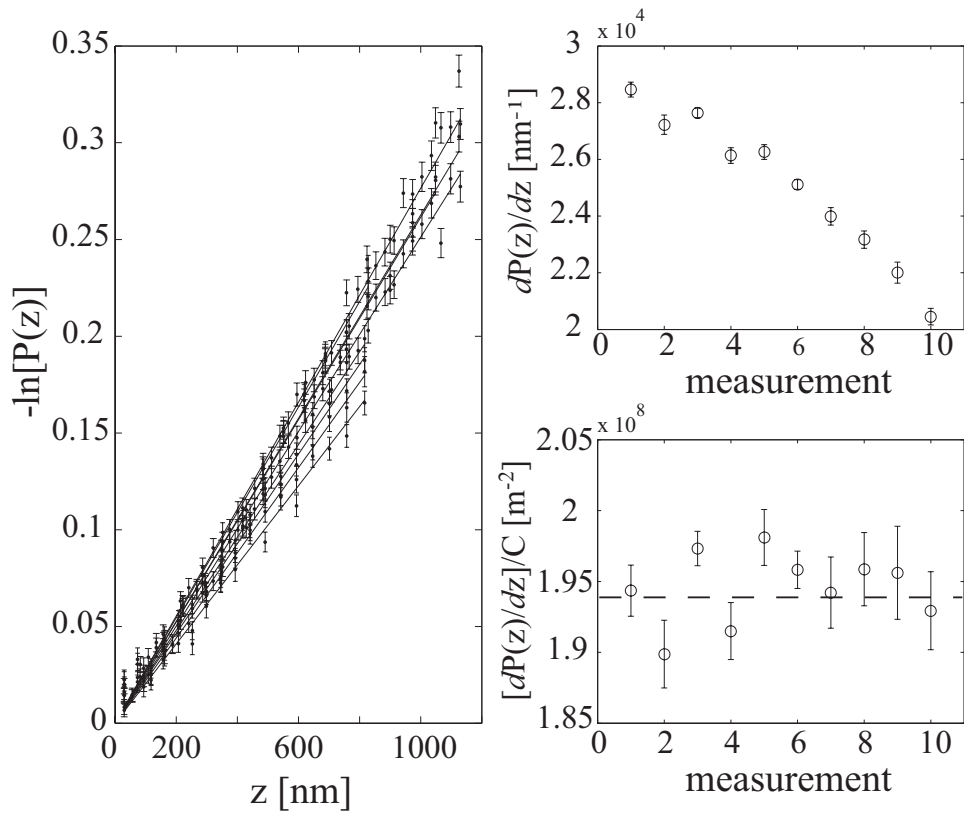


Figure 2.5: The initial slopes of the polarisation $\frac{d \log(P)}{dz}$. The slopes are proportional to the grain packing-fraction and the sample thickness multiplied by a constant (see Eq. (2.19)). Dividing out the known thickness and the packing fraction ($C = \phi_{grain}(1 - \phi_{grain})t$) should yield a constant term for all measurements as seen in the lower right figure. This analysis makes it possible to determine the solid grain density, yielding about $1.1\text{g}/\text{cm}^3$.

at the lower stress amplitudes and produces relatively large changes in a . When the larger and weaker heterogeneities have collapsed and produced a denser structure any further densification is created by the rearrangement of primary grains. This latter stage is governed by higher stresses and smaller changes in the characteristic size of the heterogeneities. This “hard-core” behaviour is illustrated when we plot the stress versus the characteristic size a in Fig. 2.6. The stress diverges at around 1400nm and no significant changes is seen for higher stresses. The total microscopic strain for the experiment is given by

$$\delta a_{\text{tot}} = 1 - \frac{a_{\text{end}}}{a_0} = 1 - \frac{1290}{1780} \simeq 28\%, \quad (2.20)$$

where a_{end} is the characteristic size reached at the maximum applied strain and a_0 is the size at the beginning. This value is comparable with the final macroscopic strain, being about 35% (see Fig 2.3).

The Hurst exponent decreases with increasing strain, consistent with the formation of a more space-filling structure as well as with an increase in the phase boundary roughness. The short range structure becomes more irregular, creating more sliding contacts which contributes to the non-linear stress-strain behaviour and in particular makes the structure more resistant towards straining.

The two microscopic strains are

$$\delta a = 1 - \frac{a}{a_0} \quad (2.21)$$

and

$$\delta \xi = 1 - \frac{\xi}{\xi_0}. \quad (2.22)$$

The microscopic strain is plotted versus the logarithm of the stress in Fig. 2.7. This shows that the exponential stress-strain relationship measured macroscopically has its origin in a similar relationship at the microscopic level.

2.5 Discussion and conclusions

A stress-strain measurement was conducted simultaneously with a bulk microstructural investigation by using spin-echo small-angle neutron scattering on a cohesive silica powder (Sipernat-310). The microstructure was characterized in terms of the autocorrelation function of the density distribution and the experimental result was modelled using a correlation function describing a random density distribution. The correlation function characterizes the density distribution in terms of its typical size a and a self-affine parameter called the Hurst exponent H , related to the short-range correlations, i.e., to the structure of the phase boundaries. The proposed correlation function proved excellent at describing our measured data.

The primary grain density was determined by analysing the initial slopes of the SESANS measurements. This yields a density of about a factor of 2 smaller than the

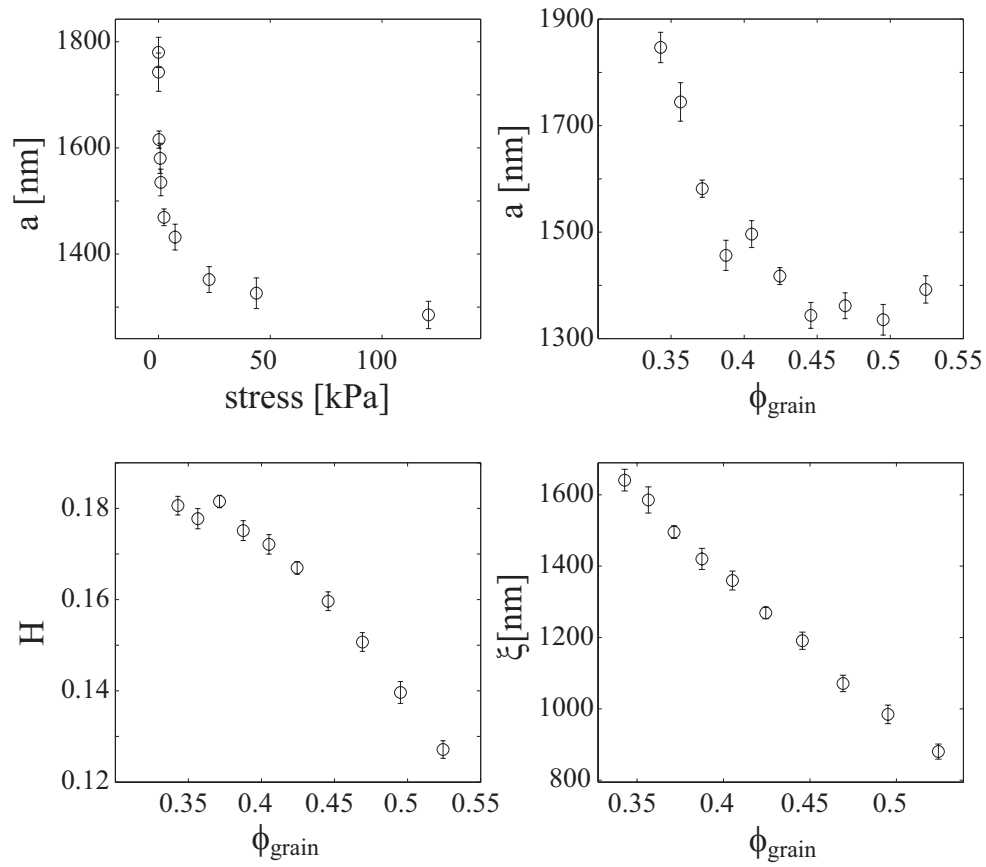


Figure 2.6: The characteristic size a and the Hurst exponent H obtained when applying the model Eq. (2.13) to the measurement. The model shows that the characteristic size as well as the Hurst exponent H decreases as a function of compression (higher ϕ_{grain}). The packing fractions are here expressed in terms of the grain-packing fraction ϕ_{grain} defined in Eq. (2.18)

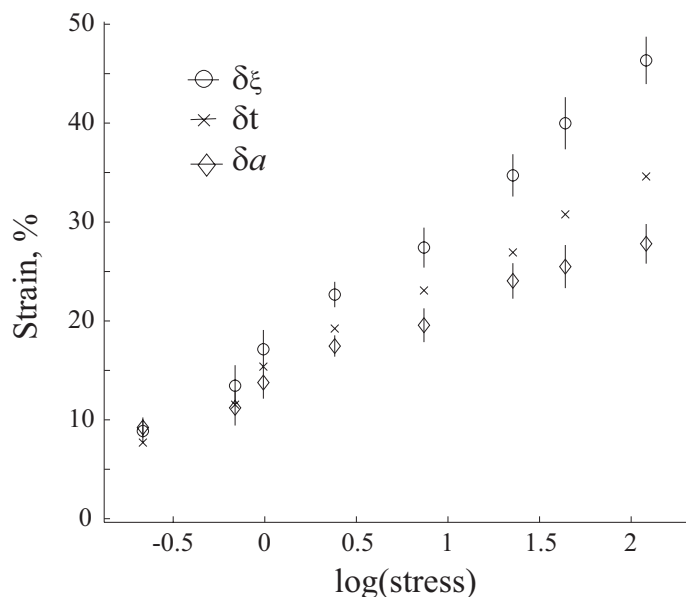


Figure 2.7: The logarithm of the stress plotted as a function of microstructural strains δa and $\delta\xi$ together with the macroscopic stress strain relationship.

skeleton density of pure silica. The grain density can be used to calculate the packing fraction of grains contained in the sample. A divergence of the stress is reported at a packing-fraction around 0.50.

The fractal nature of the powder can be quantified in terms of the so-called Hurst exponent. When the powder is compressed, decreasing Hurst exponents are evidenced as a function of strain. A decreasing Hurst exponent implies that a more “disordered” density distribution is being formed, and we argue that such a structure can pack more efficiently, thus facilitating the compression of the powder. The decrease in the Hurst exponent also indicates the buildup of a rougher, more disordered, interface. Similar observations have been made in metals [85], shear zones in granular materials [77], and fracture studies [6]. The increase in interface roughness creates more sliding contacts and friction between grains, in essence acting against the action of compression, and contributes to the non linear stress-strain behaviour observed in the macro as well as in the microscopic domain.

Compression of the powder using relatively small stress levels, breaks and collapses the larger voids and clusters that are stabilised by weaker van der Waals forces. This phenomenology is supported by the measurement in a sense that microstructural length scale a decreases quickly for relatively low stresses. Further densification can be achieved through the movement and rearrangement of hard primary grains. Such a structural rearrangement calls for larger stress levels. The measurement shows a sharp diverging stress for smaller characteristic sizes a , and we argue that a domain is reached where the structural rearrangement is governed by hard core exclusions.

The total microscopic strain δa_{tot} (28%) observed in the experiment is comparable, but lower, than the value for the total macroscopic strain of the sample $\sim 35\%$. When the microscopic stress-strain relationship is further analyzed it is evident that the macroscopic exponential behaviour has its origin in a similar microscopic relationship.

It is well established that force networks and chains play an important role in the physics of granular matter [34]. In the measurements conducted here and elsewhere [3] no density correlations were observed beyond the size of a single grain. The measurements can lead to the conclusion that (if present) such networks do not create correlations in the density distribution.

As opposed to discussing the density distribution in terms of a sphere and its diameter, or any other shape of a grain and its size, we argue that parameters such as a (the width of the autocorrelation function of the density distribution) and also ξ (the correlation length of the distribution) represents more general and even well-defined descriptors of the material's microstructural size, especially when realistic materials are considered, materials that typically contain many different shapes having many different sizes.

An important connection between microstructure and macroscopic mechanical behaviour of a powder has been made. The study was made possible by a unique neutron scattering investigation using SESANS. It was shown that the random media model, given by the von Karman correlation function, is excellent at describing the structure of a cohesive powder in a wide range of packing fractions and the model parameters involved provide insight into the mechanics and microstructure of the compressed powder.

Acknowledgments

We thank Chris Duif at the Reactor Institute Delft for valuable discussions and help with performing the experimental part of this work. This work is part of the research programme of the 'Stichting voor Fundamenteel Onderzoek der Materie (FOM)', which is financially supported by the 'Nederlandse Organisatie voor Wetenschappelijk Onderzoek (NWO)'.

Chapter 3

Structure, anisotropy and fractals in compressed cohesive powders

This article, By Robert Andersson, Wim G. Bouwman, Jeroen Plomp, Fokko M. Mulder, H. Gijs Schimmel, Ignatz M. De Schepper, was accepted for publication by the scientific journal: Powder Technology.

Abstract

Correlation functions are commonly used to characterise the microstructure of materials. The correlation function is then related to other properties or phenomenology connected to the investigated material. In this paper, we investigate the bulk microstructure in two cohesive powders –a silica powder containing spherical grains and a carbon nanotube powder, by means of spin-echo small-angle neutron scattering technique. We show that, for the silica powder, the typical size of the heterogeneities decreases with increasing strain, thus linking microscopic deformations with the macroscopic ones. Measurements also show that the compressed silica powder is isotropic in terms of its density distribution. On the compressed nanotube powder we are able to conclude that the applied uniaxial stress induces anisotropy in the density distribution. We are able to link the compressive strain with the measured anisotropy, thus creating the link between macroscopic and microscopic behaviours. Both powders are shown to have a fractal structure, and are characterised in terms of a fractal dimension.

3.1 Introduction

Granular and powder materials show a range of interesting phenomenology and complicated behaviour yet to be explained by a unified granular theory [36, 38]. Powders are normally characterised by history dependence, non-linearity, inhomogeneity, anisotropy etc. Powders are usually cohesive, meaning that for assemblies of small grains ($<100\mu\text{m}$), electrostatic, capillary and van der Waals interactions become increasingly relevant to consider. All together making the cohesive powder very different from dry frictional granular media [76]. Cohesive powders are widely handled throughout industry, producing a variety of costly process-related problems such as clustering, bridging and channelling, leading to, for example, oscillating mass flows in silos [82, 76].

The increase in computational capacity has made the field of granular physics and the study of powders mainstream, so that detailed analysis of the dynamics and structure can be routinely done on numerical data [61, 47]. Alongside computer simulations and modelling, the field needs experimental observations that supports the buildup of models and theory. In particular, the field is in the need for microstructural investigations.

To experimentally extract the microstructure from granular and powder materials is a challenging task –new techniques and methods are needed. Until now, such experiments have been done in the framework of X-ray tomography [5, 67, 71], Magnetic Resonance Imaging [70, 55] or as a 2D imaging investigation [50]. Although the most general way to study structure in any material is by means of conventional wave diffraction methods, the current resolution (reciprocal space) of such instruments does not allow for the study of powders and granular materials at the grain level and beyond.

Opaque materials characterised by inhomogeneities at mesoscopic length scales (colloids, polymers, macromolecules etc.) are commonly investigated with Small-Angle Neutron Scattering techniques (SANS) [23]. Conventional SANS is limited in measurable length scales to a few hundred nanometer and multiple scattering complicates the data analysis [68]. A modified SANS technique, Spin-Echo Small Angle Neutron Scattering (SESANS) [9], increases the resolution so that structures up to $20\mu\text{m}$ become accessible, and therefore being applicable to the study of microstructure in fine cohesive powder-materials [1]. A SESANS experiment measures the samples microstructure in terms of the projection of the density-density correlation function [45].

We have successfully applied SESANS on a uniaxially compressed cohesive powder as well as on a nanotube powder. We found that the measured correlation function is well described by the dimensionality of the structure, either being fractal or having integer dimensionality within a cutoff length. We are able to show that straining the sample by uniaxial compression induces anisotropy in the microstructure of a nanotube powder. A measurement on a uniaxially compressed silica powder, made up of isotropic spherical grains, shows no anisotropy in the density distribution.

3.2 Theory and method

3.2.1 The density-Density correlation function

The density distribution $\rho(r)$ in a two phase material fluctuates around its mean value. These fluctuations might have some characteristic size (particle radius), being scale invariant (fractal), regular (crystalline), random etc. All together, that is the structure of a sample. Characterising the density distribution can be done by analysing its autocorrelation function. After subtracting the mean density $\Delta\rho(r) = \rho(r) - \bar{\rho}$ we have:

$$C(r) = \langle \Delta\rho(0)\Delta\rho(r) \rangle \quad (3.1)$$

where the mean square fluctuation term is

$$C(0) = \Delta\rho_s^2\phi(1 - \phi). \quad (3.2)$$

ϕ is the packing-fraction

$$\phi = \frac{1}{V} \int \rho(r) \quad (3.3)$$

and $\Delta\rho_s = \rho_1 - \rho_2$ is the solid density difference between the two phases. The normalised correlation function is the density-density correlation function:

$$\gamma(r) = \frac{C(r)}{C(0)}. \quad (3.4)$$

The projection of a circular symmetric $\gamma(r)$ along lines separated by a distance z from the origin is

$$G(z) = \frac{2}{\xi} \int_z^\infty \frac{r\gamma(r)}{\sqrt{r^2 - z^2}} dr \quad (3.5)$$

The projection is made dimensionless with the correlation length of the density distribution [23].

$$\xi = 2 \int_0^\infty \gamma(r) dr. \quad (3.6)$$

$G(z)$ and ξ are the microstructural quantities that are measured in a SESANS experiment.

The correlation length ξ is measured along the neutron beam-axis of a SESANS experiment, which is perpendicular to the correlating direction z . If the beam direction is along the x coordinate, then the projection in Cartesian coordinates become

$$G(z) = \frac{2}{\xi} \int_0^\infty \gamma(x, 0, z) dx \quad (3.7)$$

where the correlation length is

$$\xi = 2 \int_0^\infty \gamma(x, 0, 0) dx. \quad (3.8)$$

And there is no sensitivity in along the y coordinate. The correlation length is a measure of the width of the distribution $\gamma(r)$, this is a non trivial quantity but can be understood as a measure of the size of the inhomogeneities in the sample (for a hard-sphere gas the correlation length is 3/4 of the sphere-diameter).

3.2.2 Spin-Echo Small Angle Neutron Scattering (SESANS)

Spin-echo Small Angle Neutron scattering (SESANS) is based on the Larmor precession of neutrons in parallelogram shaped magnetic field regions [66], [24], [79]. In SESANS, the polarisation of a neutron beam is measured, after transmission through a sample, as a function of the so called spin-echo length, z ($30\text{nm} < z < 20\mu\text{m}$). The spin-echo length is a real-space parameter being the size at which correlations are measured. The neutron detector situated after the sample and after the polarisation analyser. Scattering from large micro structures, as considered here easily falls within the detector acceptance angles. A discussion can be found in [63].

The polarisation of the neutron beam is normalised with an empty beam measurement. As a function of z the normalised polarisation is

$$P(z) = e^{\Sigma_t(G(z)-1)}, \quad (3.9)$$

where

$$\Sigma_t = t\lambda^2\Delta\rho_0^2\phi_1\phi_2\xi. \quad (3.10)$$

Here t is the sample thickness, λ being the neutron wavelength and $\Delta\rho_0$ is the neutron scattering length density difference in the sample (directly related to the chemical composition of the sample).

For a structure with no long range order we have $G(\infty) = 0$, so that at some finite length scale we expect no more correlations. This gives a constant saturation level/amplitude of the polarisation:

$$P(\infty) = e^{-\Sigma_t}. \quad (3.11)$$

Thus, the polarisation at saturation is proportional to the packing fraction and the correlation length of the sample-inhomogeneities, according to Eq. 3.10.

For dense monodisperse hard-sphere packings one would, due to excluded volume, observe correlations in the form of nearest neighbour peaks. This is, however, not the case for disordered materials made up of random shapes and sizes.

3.2.3 Random and fractal microstructures

For scattering from a perfectly random distribution of solids and holes –a Swiss-cheese, we use the correlation function given by the Debye, Anderson and Bueche (DAB) formalism [20], [19], so that

$$\gamma(r) = e^{-r/a} \quad (3.12)$$

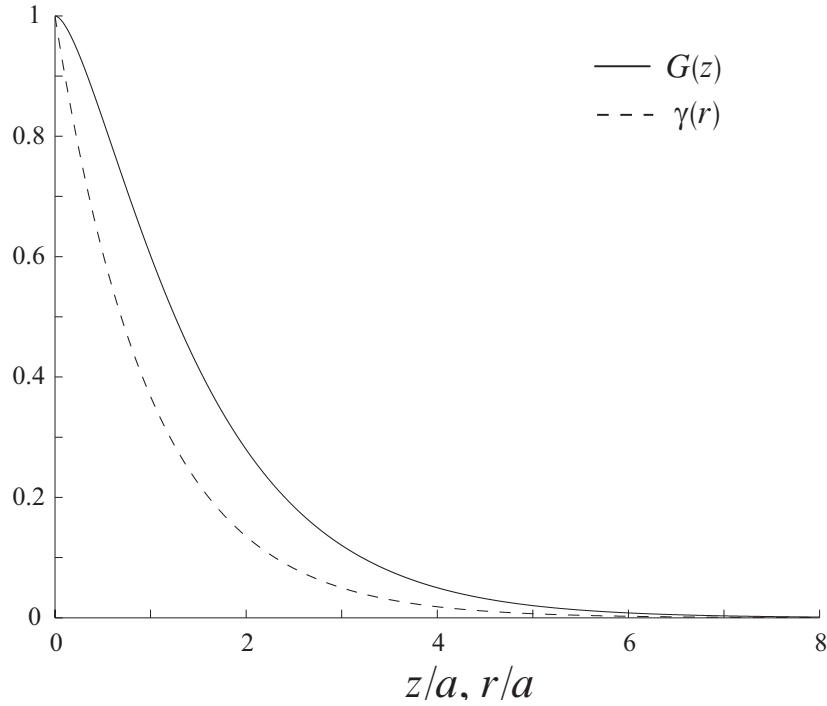


Figure 3.1: The figure is showing the auto correlation function $\gamma(r) = e^{-r/a}$ (dashed line) for perfectly random porous material. $G(z)$ (solid line) is the projection of $\gamma(r)$.

where a is a measure of the size of the inhomogeneities contained in the sample. The corresponding SESANS correlation function for such material is found by inserting Eq. (3.12) in Eq. (3.5), giving

$$G(z) = \frac{z}{a} K_1\left(\frac{z}{a}\right) \quad (3.13)$$

where K_n is the modified Bessel function of the second kind (see Fig. 3.1). This expression has been derived from the reciprocal space counterpart of Eq. (3.12) in [80]. The correlation length for such density distribution leads to:

$$\xi = 2 \int_0^\infty e^{-r/a} dr = 2a. \quad (3.14)$$

Thus, there are two relevant length scales involved in a SESANS measurement: first ξ as the correlation length measured along the neutron beam axis, and secondly, the typical size of the inhomogeneities a , measured perpendicular to the beam.

Although, in the DAB formalism we see that these two quantities are trivially related, it is not generally the case, since ξ will depend on the shape/dimensionality of the inhomogeneities. In order to consistently describe the measurements one has to find both quantities a and ξ , bearing in mind that they are not the same or easily related.

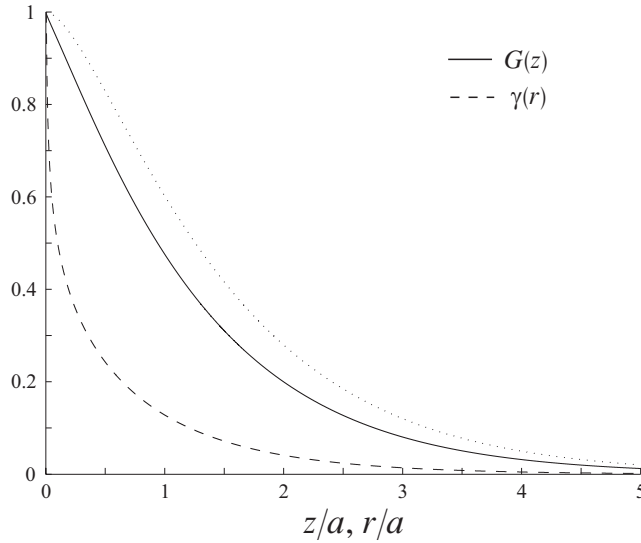


Figure 3.2: The figure shows the auto correlation function $\gamma(r)$ of a self similar -fractal material with $d=2.80$. $G(z)$ (solid line) is the projection of $\gamma(r)$ (dashed line). The dotted line shows $G(z)$ for a random inhomogeneous solid (i.e. $d=3$), according to Eq. (3.13)

Eq. (3.12) is valid for a structure with randomly distributed solids bounded by smooth 2D surfaces [84]. For a material with a structure that is self-similar or self-affine, we expect the correlation function to depend on the dimensionality of the structure (see for instance [69], [72]):

$$\gamma(r) \propto r^{d-3}, \quad (3.15)$$

where d is the so called fractal dimension. Taking into account the finite extension of the fractal, one usually introduces an exponential cutoff given by the DAB formalism. [72], so that:

$$\gamma(r) = (r/a)^{d-3} e^{-r/a} \quad (3.16)$$

In the special case of the integer dimensionality of $d=3$ we see that Eq. (3.16) reduces to Eq. (3.12). The SESANS counterpart for a fractal dimensionality is found by numerical integration of Eq. (3.5) (see Fig. (3.2)).

Any realistic material will have a finite extension, in a sense that it is made up from building-blocks of some size a_0 . Taking into account the two finite sizes a and a_0 we are able to derive an expression for the correlation length (i.e., normalising and integrating from a_0 to ∞ in Eq. (3.6) using Eq. (3.16)). The correlation length becomes:

$$\xi = 2a_0 e^{a_0/a} E_{3-d}(a_0/a), \quad (3.17)$$

where

$$E_n(x) = \int_1^\infty \frac{e^{-xt} dt}{t^n}. \quad (3.18)$$

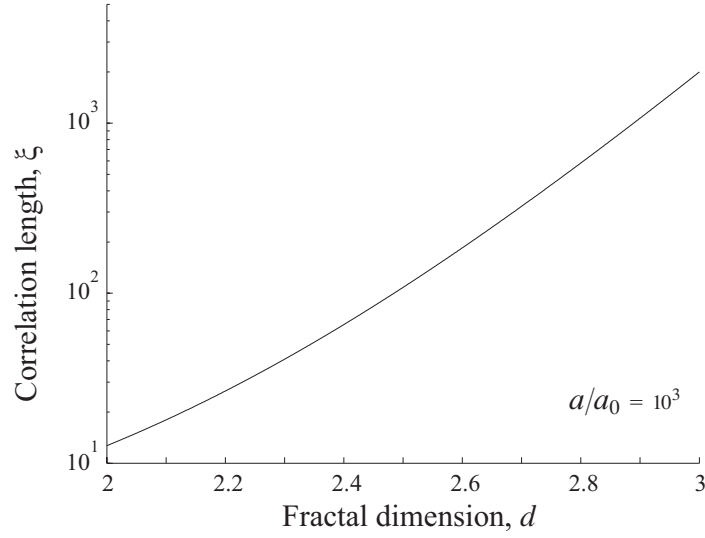


Figure 3.3: The correlation length ξ as a function of the fractal dimension d according to Eq. (3.17). For a finite fractal bounded by a building-block a_0 and some outer cutoff a we see that the correlation length decreases with decreasing dimensionality. For a SESANS experiment this means less scattering and less depolarisation for lower dimensionalities (see Eq:s 3.10 and 3.11).

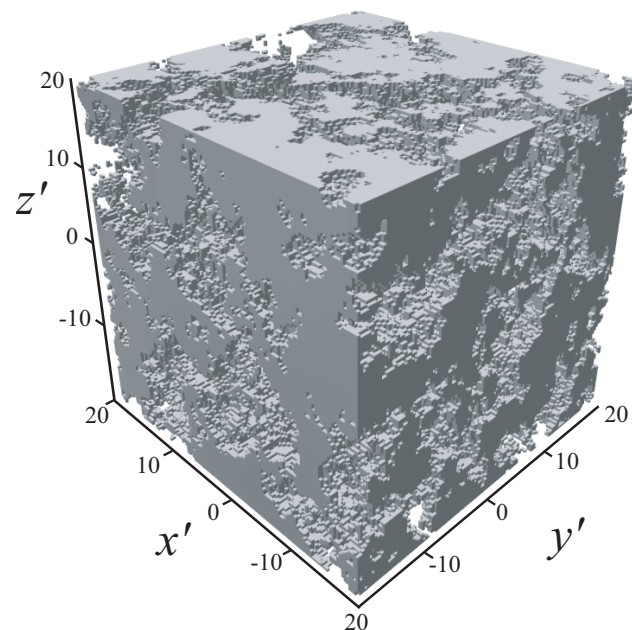
is the so called generalised exponential integral. This shows that the correlation length ξ is decreasing with decreasing dimensionality d for a given characteristic size a . Thus, the end level of polarisation will increase with decreasing dimensionality, see Fig. 3.3. This expression makes it possible to interpret the level of the saturation level in SESANS experiment, since it will depend also on the dimensionality of the structure.

3.2.4 Anisotropy

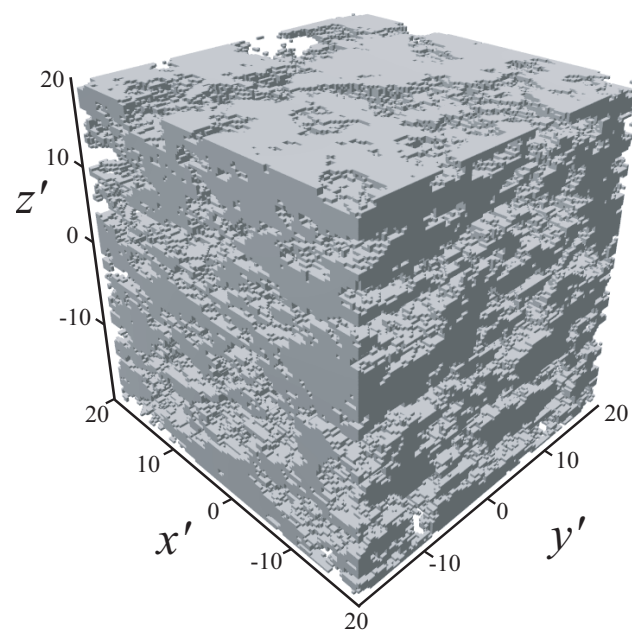
The 3D density distributions in Fig. 3.4 are examples of self affine structures. The correlation function $\gamma(r)$ for the isotropic figure is given by Eq.3.16, with $d = 2.8$. The bottom figure is anisotropic in its density distribution in a sense that its characteristic size is smaller along the z' coordinate.

The density distributions in Fig. 3.4 are calculated in the wavenumber domain q , where a uniform white noise is filtered by a self affine spectral filter (i.e., the Fourier transform $I(q)$ of $\gamma(r)$). This is the power spectrum of the density distribution (i.e., the square of the fourier amplitudes of $\Delta\rho(r)$). A real space representation of this random media is then calculated by inverse fast Fourier transform to yield $\Delta\rho(r)$. We used a spectral filter according to the Fourier transform of Eq. (3.16) found in [72]. For the anisotropic case we used a coordinate transformation $q = \sqrt{(q_x a_x)^2 + (q_y a_y)^2 + (q_z a_z)^2}$. The calculation is fast and straightforward, and more details about the procedure can be found in [41].

Anisotropy in the density distribution can be studied with SESANS, provided that the sample can be re-oriented and rotated in the neutron beam. When fixing the



Isotropic



Anisotropic

Figure 3.4: Example of a 3D self affine anisotropic and an isotropic density distribution. The top figure shows the isotropic case and the bottom figure is the anisotropic counter part. The bottom figure is anisotropic in its density distribution in a sense that its characteristic size a is smaller along the z' coordinate by a factor of two.

SESANS coordinate system so that the projection is along the x coordinate and the correlations are measured in the z coordinate, we get that:

$$G(z) = \frac{1}{\xi} \int \gamma(x, 0, z) dx. \quad (3.19)$$

and

$$\xi = \int \gamma(x, 0, 0) dx. \quad (3.20)$$

Consider Fig. 3.4, the two illustrations represents: top an isotropic density distribution, and the bottom illustration is an anisotropic counterpart.

The three orthogonal projections will produce two correlation lengths, related to $a_{z'}$ when the projection is along the z' coordinate and if the projection is along either x' or y' coordinates the correlation length will be proportional to $a_{x'}$ and $a_{y'}$. The shape and width of $G(z)$ will depend on which of the coordinate, x' , y' or z' is parallel to the z coordinate. Thus the width of the $G(z)$ curve is related to $a_{x'}$ when z is parallel to x' and $a_{y'}$ if parallel to y' and related to $a_{z'}$ when parallel to the z' coordinate in Fig. 3.4.

We can formulate the correlation functions in a more general way with having the SESANS coordinate system fixed so that the spin echo-length is along the z coordinate and the projection (beam direction) is in along the x coordinate. The correlation function for the three distinct cases is, with $\zeta_{a_p, a_c} = \sqrt{(x/a_p)^2 + (z/a_c)^2}$:

$$\xi G(z) = \begin{cases} \int \zeta_{a_{z'}, a_{x'}}^{d-3} e^{-\zeta_{a_{z'}, a_{x'}}} dx & \text{if } x \parallel z' \ \& \ z \parallel x' \text{ (i)} \\ \int \zeta_{a_{x'}, a_{y'}}^{d-3} e^{-\zeta_{a_{x'}, a_{y'}}} dx & \text{if } x \parallel x' \ \& \ z \parallel y' \text{ (ii)} \\ \int \zeta_{a_{x'}, a_{z'}}^{d-3} e^{-\zeta_{a_{x'}, a_{z'}}} dx & \text{if } x \parallel x' \ \& \ z \parallel z' \text{ (iii)} \end{cases} \quad (3.21)$$

where the subscript p and c means projection direction and correlation direction, respectively. For a density distribution that is rotational invariant (isotropic) in one plane (the $x'y'$ -plane in Fig. 3.4), the three measurements noted by Eq.3.21 will be enough to characterise the anisotropy. Although, in total, six orthogonal measurements can be carried out (two correlation directions for each three projections), we have that the projection along y' will equal the projection along x' . From the rotational invariance in the $x'y'$ -plane it follows that only one measurement along z' is needed.

In SESANS it is the polarisation that is measured, according to Eq.3.9. We plot the results expected for the polarisation in Fig 3.5.

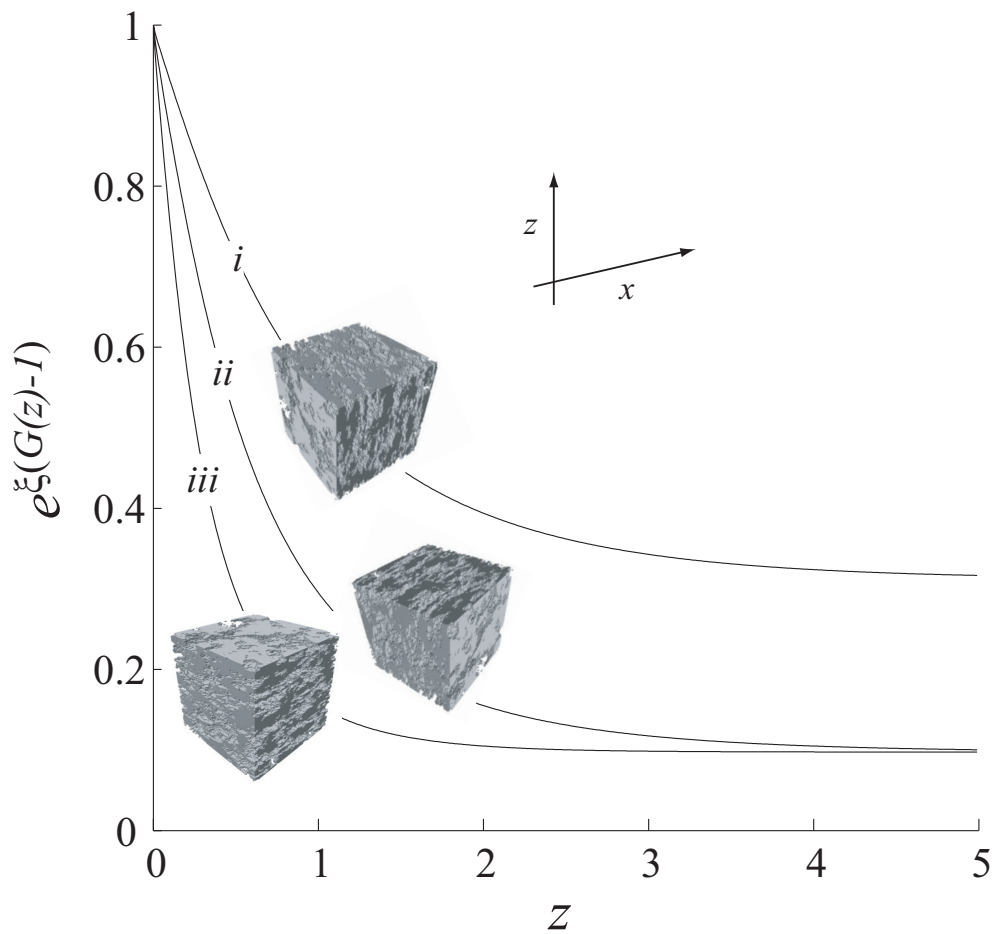


Figure 3.5: Numerical solution of Eq. (3.21) with $d=2.8$, $a_{x'}=a_{y'}=1$ and $a_{z'}=0.5$, illustrating how anisotropy manifests in a SESANS experiment. The (x, z) coordinate system represent the SESANS instrument coordinate system, where x is the neutron beam path and correlations are measured along z .

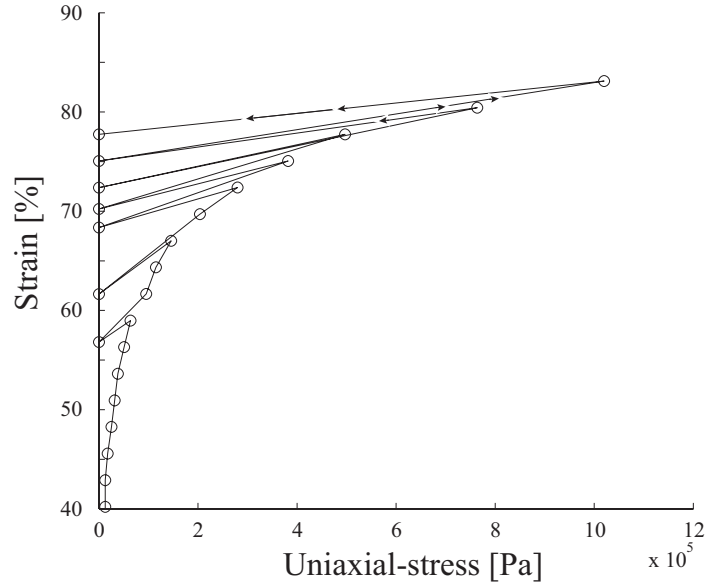


Figure 3.6: Stress-strain curve for the uniaxially compressed nanotube powder. The line (guide to the eye) indicates the applied stress path. Note that the powder packing expands when relaxing the stress for the larger applied stresses.

3.3 Samples and experiments

3.3.1 Silica powder

A silica (SiO_2) powder was kindly provided by Kobo Products, Inc (traded as MSS3H). The powder contains porous spherical grains with an average size around $3\mu\text{m}$, centred on a wide lognormal distribution. The silica powder was characterised in terms of primary particle porosity. The porosity measurement showed that the primary spherical grains have a density of $0.45\text{g}/\text{cm}^3$, which is in good agreement with that stated by the manufacturer (0.5). We use the particle density in order to calculate the equivalent sphere packing-fraction

$$\phi_{sph} = \frac{\rho_{sample}}{\rho_{grain}} \quad (3.22)$$

where ρ_{sample} is the density in g/cm^3 of the sample and ρ_{grain} is the density of a primary grain. This "grain" packing fraction is different from the skeleton packing fraction

$$\phi_{sk} = \frac{\rho_{sample}}{\rho_{bulk}}, \quad (3.23)$$

derived from the solid silica density $\rho_{bulk}=2.2\text{g}/\text{cm}^3$ (see also Table 3.1).

We used a simple uniaxial compression scheme to strain the sample. A pressure cell having a cylindrical geometry was filled with powder, by carefully raining the powder into the cavity. The powder was uniaxially compressed with a plunger until a desired strain was achieved.

With strain being

$$\delta = 1 - \frac{t}{t_0}, \quad (3.24)$$

where t_0 and t is the sample thickness before and after compression, respectively.

Four different stress levels were used: 3kPa, 21kPa, 35kPa and 700kPa. The applied stresses yielded, with increasing stress, a sphere packing-fraction of $\phi_{sph} = 0.60, 0.65, 0.77, 0.85$.

The sample was mounted with the neutron beam parallel to the compression direction so that the correlation function was sampled perpendicular to the compression direction. We did not observe any large structural changes (cracks, holes, settling etc.) of the compressed powders during the measurement, indicating a macroscopically stable packing throughout the measurement. The measurement was done in ambient conditions and the moist content was determined (by drying followed by weighing) to 11% by weight.

Another sample was uniaxially compressed in a cylindrical pressure cell, resulting in a compressive strain of $\delta=47\%$. This sample was prepared in order to investigate the density distribution in different directions w.r.t the applied compression direction, i.e., anisotropy.

A measurement was also performed on an uncompressed powder packing, from now on referred to as the poured-sample ($\phi_{sph} = 0.5$) (see Table 3.1). This sample was prepared by carefully raining the powder into the container. Measurements on $P(z)$ show that the preparation procedure is reproducible.

3.3.2 Nanotube powder

A nanotube sample (Single Walled NanoTube) was obtained from Carbon Nanotechnology, Inc. and used without further treatment and in ambient conditions. Single walled nanotubes are cylindrical graphene sheets with fullerene endcaps. The tube lengths can be between 10-100nm (typically 10-20nm) having diameters of 1-2nm (see for instance [81], [21]). In the SESANS experiments conducted here, the nanotube powder was uniaxially compressed in a cuboid with 100kPa uniaxial stress. This produced a volumetric strain of about 60%.

Three measurements were carried out in three different directions with respect to the compression direction. We measured the correlation function with z either parallel or perpendicular to the stress direction in combination with having the beam-axis either parallel or perpendicular, see also the illustration in Fig. 3.9. One measurement was conducted on a uncompressed sample.

A stress-strain measurement was conducted to further characterise the nanotube powder (see Fig. 3.6). The measurement shows that the powder is expanding upon releasing the applied stress. The SESANS experiment was conducted on a sample having a fixed top plate that hindered such elastic relaxation. The thickness of the sample, (i.e., the neutron transmission length t) was the same for all three measured

Table 3.1: Experimental parameters and results from SESANS experiments on the silica powder. * the correlation length ξ was calculated with Eq. (3.14). For the poured sample ξ was calculated by fixing $\Delta\rho_0=2.22\times 10^{14}$ m⁻², being the average of the other four measurements (a_0 could not be determined from the measurement). ** The effective scattering length density $\Delta\rho_0$ was calculated from fitted/measured parameters and Eq. (3.10).

σ [kPa]	δ_b [g/cm ³]	ϕ_{sk} [-]	ϕ_{sph} [-]	t [mm]	a [nm]	* ξ [nm]	d [nm]	** $\Delta\rho_0$ [10 ¹⁴ m ⁻²]
0	0.25	0.11	0.5	5.0	930 ± 74	1100 ± 40	2.91 ± 0.02	1.22
3	0.30	0.14	0.6	4.3	647 ± 10	1290 ± 50	3	1.27±0.11
21	0.33	0.15	0.66	3.9	575 ± 10	1148 ± 54	3	1.23±0.05
35	0.39	0.18	0.78	3.3	543 ± 10	1082 ± 54	3	1.21±0.05
700	0.42	0.19	0.84	3.0	427 ± 13	855 ± 20	3	1.18±0.02

directions, 6.2mm, meaning that the measurement is reduced to only two parameters, $G(z)$ and ξ , when comparing the different directions. For the poured-sample we used a 12.3mm thick sample.

3.4 Results and discussion

3.4.1 Silica powder

We used three parameters to describe the structure of the compressed silica powder, a dimensionality d of the structure, the characteristic size a of the heterogeneities and $\Delta\rho_0$ being the constant scattering-length-density of the silica.

For the compressed powders we find that the randomly heterogeneous structure described in the DAB formalism models our data well, reducing the problem to two parameters (see Eq. (3.13) and Eq. (3.9)).

As the stress amplitude and the compressive strain is increased we see that the characteristic size a of the inhomogeneities decreases (see Table 3.1). By compressing the sample, voids and clusters will collapse, grains will arrange in a more space filling system. This is consistent with a decreasing characteristic size and a high dimension.

The uncompressed sample, shown at the bottom in Fig. 3.7, was best fitted by using Eq. (3.16) in Eq. (3.5) with a fractal dimension of 2.91, and a characteristic size $a=930$ nm. We were unable to determine the fractal building-block size a_0 from the model since it is outside the resolution of the instrument.

We fixed $\Delta\rho_0$ to the average of the other four measurements since a model has to yield the same $\Delta\rho_0$'s for all five measurements in order to be consistent. Note that ξ can be calculated from Eq. (3.11) and the model parameters.

The uncompressed sample shows a relatively low depolarisation (low Σ_t), meaning that the simple $\xi=2a$ relationship does not hold here. We argue that it is the dimensionality of this microstructure that gives rise to the relatively low depolarisation. Thus, together with the shape of the curve, we get another strong indicator of the fractal nature of this poured powder state.

For the uncompressed sample we note that the correlations extend outside the measured range in z . This shows that the major heterogeneities are larger than the

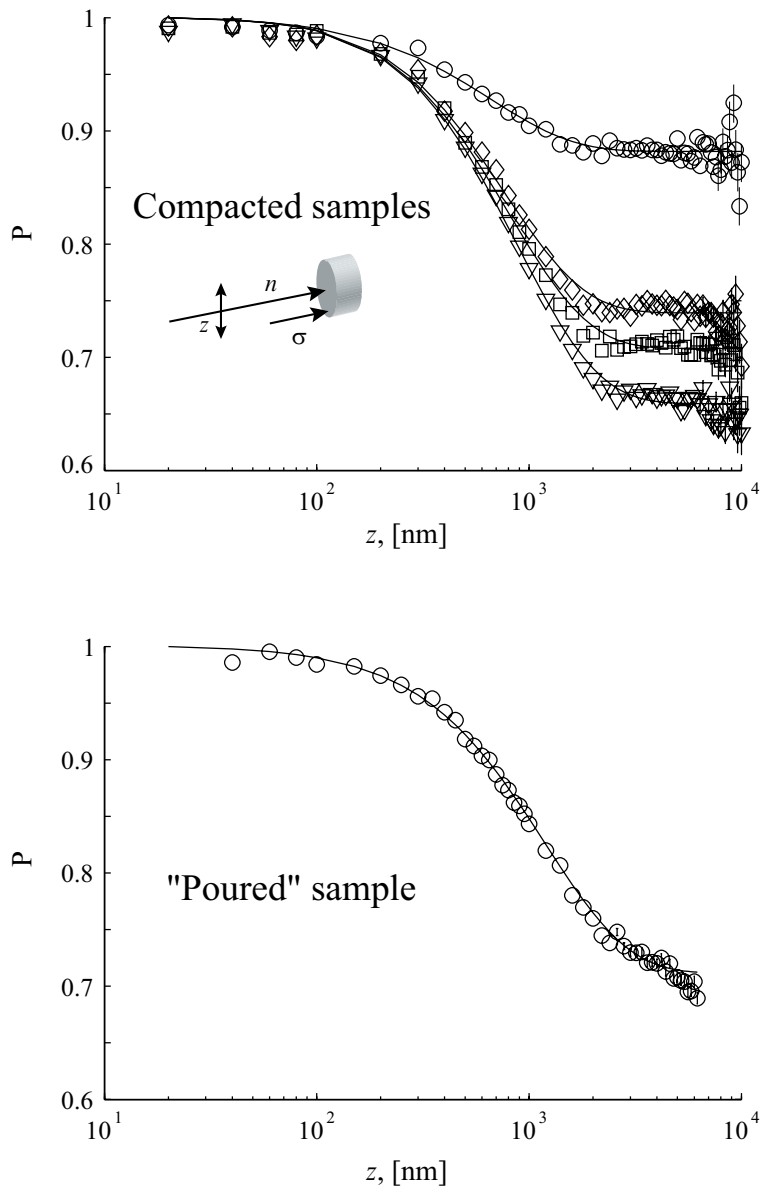


Figure 3.7: The figure shows the measured polarisation as a function of spin-echo length, z for the compressed silica powder. In the top figure the symbols correspond to different uniaxial stresses: triangles 3kPa, squares 21kPa, diamonds 35kPa and circles 700kPa. The lower figure represents the poured-sample. The illustration in top graph illustrates the experiment so that the beam is parallel to the stress direction and the spin-echo z direction is perpendicular to the applied stress. Lines are fits according to Eq. (3.9), having the parameters quoted in Table 3.1. The inset in the figures show the initial linear slopes of the measurement. Unless shown, all errors fall within the markers.

reported grain size. We attribute these scales to voids and clusters created by van der Waals attraction, and capillary forces, acting between fine grains.

In Fig. 3.8 we show a sample that was uniaxially compressed $\delta = 47\%$ giving a packing fraction ϕ_{sph} 70%. The lines drawn through the points are fits using Eq. (3.13). The sample was arranged in three different ways: first with the neutron beam parallel (ξ is measured along the beam) to the applied compression direction and measuring correlations z perpendicular. Secondly, the sample was oriented so that the beam is perpendicular to the applied compression direction and z being parallel. A third orientation was measured, with both z and the neutron beam being perpendicular to the compression. From the measurement, although scattered, we conclude that the uniaxial strain does not produce any significant anisotropy in the density distribution, at least not at this magnitude of compression. The fitted length scales, in terms of a , are 540nm for the sample denoted by diamonds, 570nm for the circles and finally 550nm for the sample denoted by the crosses (all within $\pm 10nm$). The correlation length, i.e., the end level, is found by multiplying a by a factor of two. In Fig. 3.8 we use the convention that x is the neutron beam path, along which ξ is measured. The sample has, after compression, the same thickness (neutron transmission length) in all measured directions.

Experiments using a cuboidal sample container gave indications on anisotropy. The same procedure was used and the powder was uniaxially compressed to yield a strain of about 50%. The correlation lengths measured along the compression direction revealed a longer length scale along. This length scale could, however, not be verified by measuring its correlation (i.e., aligning the compression direction with z).

3.4.2 Nanotube powder

In Fig. 3.9 we show the measurements on the compacted nanotube powder, strained by $\delta = 0.6$. A measurement was done on an uncompressed powder, see the bottom of Fig. 3.9. We measured the polarisation, and consequently the correlation function $G(z)$ and the correlation length ξ in three different directions by rotating the sample with respect to the neutron beam. First with the beam axis x perpendicular and z parallel to the compression axis (squares in Fig 3.9), secondly with the beam parallel and z perpendicular (diamonds), and finally both with the beam and the correlation direction perpendicular to the stress direction (circles). The procedure is schematically illustrated in Fig. 3.9.

The only difference between the three directions is the microscopic arrangement of the density, i.e., the microstructure of the sample. Since the three curves does not fall on top of eachother we are able to conclude that this sample is anisotropic in terms of its density distribution. The interpretation is that the compressive straining creates a long length scale perpendicular to the applied stress.

When the sample is aligned so that the stress direction is parallel to the beam axis we get a curve with higher amplitudes, this means that a shorter length scale along the

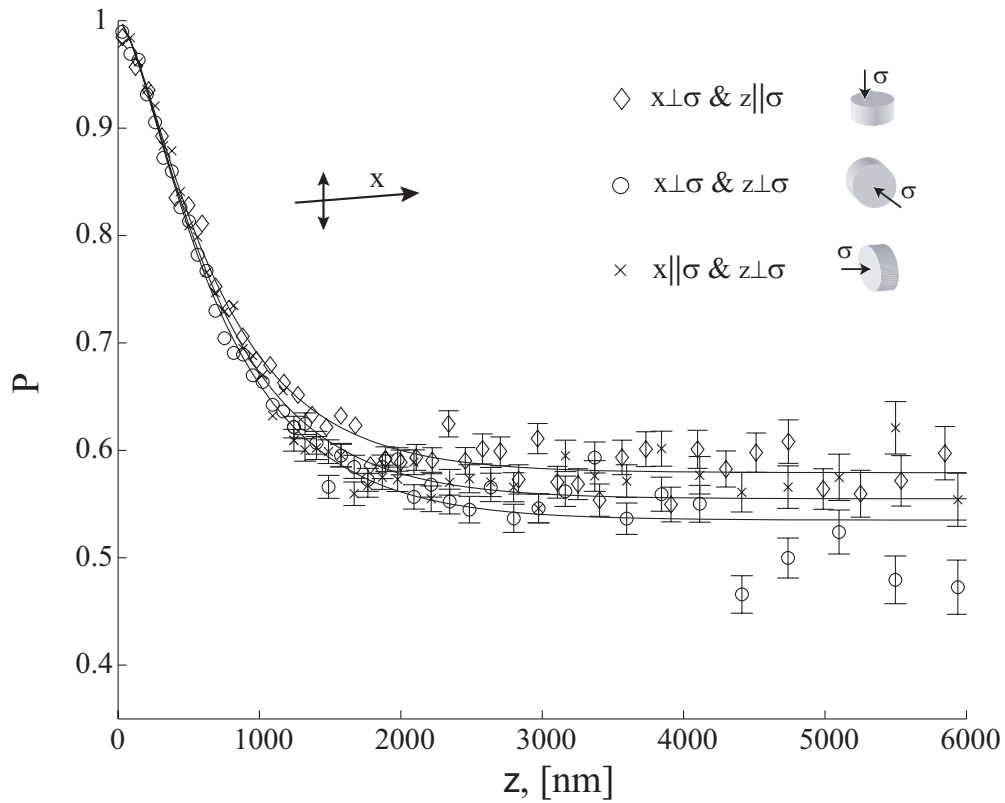


Figure 3.8: Polarisation measured as a function of spin-echo length z . A strained sample (47%) of silica powder containing spherical grains was measured along three direction w.r.t the applied compression direction. Circle represents the measurement with the beam (denoted x) and the spin-echo length z both perpendicular to the applied compression. Diamonds is with z parallel and the beam perpendicular and finally we have crosses, representing the beam parallel and z perpendicular to the strain.

beam.

Furthermore, we note that any characteristic sizes a are outside the measurable scale (the curves do not saturate), therefore it is difficult to make quantitative statements about the size of the structures.

By visual interpretation we can conclude that anisotropy is present in both the width and the amplitudes of the curves (compare also with the example in Fig. 3.5). When the correlations are probed parallel to the applied stress (squares in Fig. 3.9) we get a relatively fast decaying curve. This suggests that, in the stress direction, the typical size a is smaller as compared with the size seen perpendicular to the applied stress direction.

We use the correlation function for a fractal material to describe the measurement. The parameters that best describe our data are presented in Table 3.2. We are not able to quantify the upper cutoff a since it is outside the measured range and does not contribute to the fit (a was fixed outside the resolution).

Rather than determining Σ_t , we determine Σ_t/a by varying a outside the experimental range. This makes it possible to quantify the microscopic anisotropy present in the nanotube powder packing. We recall that a is measured in the z direction and ξ is a length measured along the beam.

We see that when we measure with the beam parallel to the stress (diamonds) the lowest value for Σ_t/a is observed (see also Table 3.2). This analysis conclude that the sample heterogeneities has a long axis perpendicular to the stress direction and a short axis aligned parallel to the applied stress. Furthermore, when looking at the two orientations where Σ_t/a is probed perpendicular to the stress (squares and circles) we see, as expected, larger correlation lengths.

Since $a \simeq \xi$, the ratio between these values is an indicator of the aspect ratio of the heterogeneities (see also Table 3.2).

$$\frac{\Sigma_t^\perp/a_\parallel}{\Sigma_t^\parallel/a_\perp} = \frac{\xi_\perp a_\perp}{\xi_\parallel a_\parallel} = 0.09/0.05 = 1.8 \pm 0.2 \quad (3.25)$$

and

$$\frac{\Sigma_t^\perp/a_\perp}{\Sigma_t^\parallel/a_\perp} = \frac{\xi_\perp a_\perp}{\xi_\parallel a_\perp} = 0.10/0.05 = 2 \pm 0.22, \quad (3.26)$$

and finally

$$\frac{\Sigma_t^\perp/a_\perp}{\Sigma_t^\perp/a_\parallel} = \frac{\xi_\perp a_\parallel}{\xi_\parallel a_\perp} = 0.10/0.09 = 1.1 \pm 0.12. \quad (3.27)$$

We see that the aspect ratio of the structure is about 2, which agrees well with the measured macroscopic strain of 60%.

An unperturbed poured-sample of nanotube powder was measured as a reference. We regard this sample to be isotropic as far as the density distribution is concerned. After correcting for the thickness we see that this sample combines the slope of the *diamond – sample* with the Σ_t of the *square – sample* (see Fig. 3.9 for notation and illustration), thus it is the isotropic equivalent having a size equal to long axis.

Therefore, we argue that the anisotropy is induced by the applied stress and enforced by the inherent anisotropy on the nanotube level.

The density distribution of the nanotube powder was found to be fractal, meaning that the correlation function shows a power law behaviour in r . We find consistently a fractal dimension ranging between 2.77-2.8 for all directions together with the uncompressed sample.

The initial slope of the measurement

A parameter free analysis can be done by analysing the slopes ∇ of the initial part of the curves (see the left corner inset in Fig. 3.9 and Table 3.2). The slopes are directly related to the anisotropy in the density distribution of the sample by the following linear approximation.

$$\nabla = \frac{-d \ln(P)}{dz} \simeq t \lambda^2 \Delta \rho_0^2 \phi_1 \phi_2 \left(\frac{a_x}{a_z} \right) \quad (3.28)$$

Where a_x/a_z gives the an aspect ratio between the size along the beam x and perpendicular to the beam z direction. Dividing the slopes with the slope for the perpendicular-perpendicular case (circles in Fig. 3.9) yields a normalised aspect ration quantity. So that unity means that we probe the same scale along and perpendicular to the beam ($a_x = a_z$), above unity means that the long length scale is parallel to the beam and finally below unity indicates that the shorter scale present along the beam. This analysis yields (with s and l denoting a short and a long axis of the anisotropic structure):

$$\frac{\nabla_{x\perp\&z\parallel}}{\nabla_{x\perp\&z\perp}} = \frac{a_{\perp}/a_{\parallel}}{a_{\perp}/a_{\perp}} = \frac{l}{s} = \frac{0.12}{0.08} = 1.5 \pm 0.2 \quad (3.29)$$

and

$$\frac{\nabla_{x\parallel\&z\perp}}{\nabla_{x\perp\&z\perp}} = \frac{a_{\parallel}/a_{\perp}}{a_{\perp}/a_{\perp}} = \frac{s}{l} = \frac{0.06}{0.08} = 0.8 \pm 0.1 \quad (3.30)$$

and

$$\frac{\nabla_{x\parallel\&z\perp}}{\nabla_{x\perp\&z\parallel}} = \frac{a_{\parallel}/a_{\perp}}{a_{\perp}/a_{\parallel}} = \frac{s^2}{l^2} = \frac{0.06}{0.12} = 0.5 \pm 0.07. \quad (3.31)$$

Thus, this simple analysis of the initial slopes yields a fairly good agreement with both the fractal model and explains about 30% of the macroscopic strain.

3.5 Conclusions

We have investigated the bulk microstructure in a uniaxially-compressed silica powder as well as for a nanotube powder. Measurements were carried out on the uncompressed powders as well. The structure were characterised in terms of the autocorrelation function of the powders density distribution. Spin-echo small angle neutron scattering (SESANS) was used to perform the measurements.

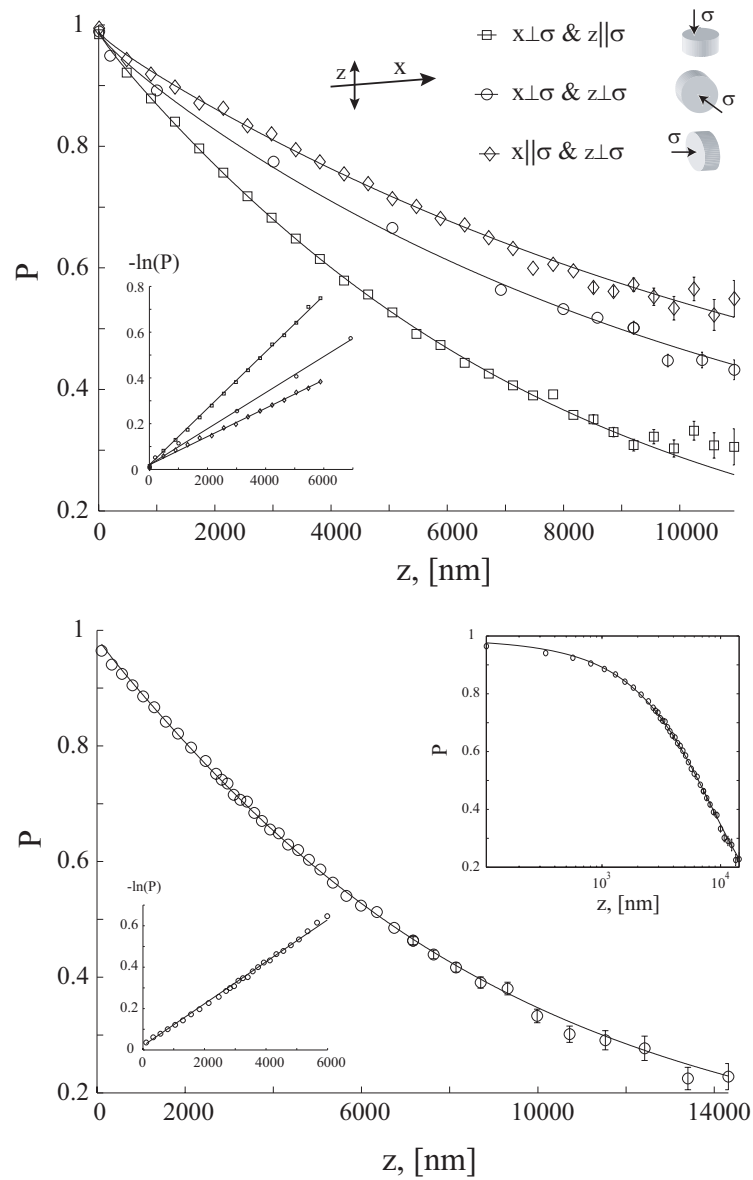


Figure 3.9: The two figures show the measured polarisation as a function of spin-echo length, z for the nanotube powder. Top figure is the compressed sample and the bottom figure shows the uncompressed sample. Diamond is with the neutron beam (x) perpendicular to the stress (σ) and spin-echo length (z) parallel to σ . Squares are $z \parallel \sigma$ and $x \perp \sigma$ and finally circles, which represents $z \perp \sigma$ and $x \perp \sigma$. The solid lines are the best fit according to Eq. (3.9). Unless shown, all errors fall within the markers.

Table 3.2: Results from the nanotube powder experiments. δ_b is the sample bulk density of solids in the sample. The linear slope ∇ was calculated from the initial part of the polarisation curve. *Corrected for a larger thickness. The value for a was fixed outside the experimental range.

Direction [-]	t [cm]	δ_b [g/cm ³]	d [-]	Σ_t/a [μm^{-1}]	∇ [μm^{-1}]
$x \perp \sigma$ & $z \parallel \sigma$, squares	0.62	1	2.81±0.01	0.09±0.01	0.12±0.01
$x \perp \sigma$ & $z \perp \sigma$, circles	0.62	1	2.77±0.03	0.10±0.03	0.08±0.01
$x \parallel \sigma$ & $z \perp \sigma$, diamonds	0.62	1	2.78±0.01	0.05±0.01	0.06±0.01
<i>Uncompressed</i>	1.23	0.6	2.82±0.006	*0.09±0.01	*0.05±0.01

The microstructure of both powders can be well described as being self affine within a cutoff length scale. The characteristic size, i.e., the cutoff length, of the density distribution decreases as a function of compression. Uniaxial compression of the nanotube powder induces anisotropy in the density distribution, so that the density fluctuations are larger perpendicular to the applied compression direction as compared to the fluctuations parallel to the compression. The silica powder, composed of isotropic grains, on the other hand, remains isotropic upon uniaxial compression. The uncompressed or poured-sample was best described as a fractal material with a fractal dimension of about 2.9 for the silica powder and 2.8 in the nanotube case.

We could, by using both the initial slopes of the raw data and the model fit parameters, quantify the aspect ratio of the anisotropic microstructure, yielding an aspect-ratio of $\simeq 2$.

No correlations was observed beyond the size of a grain in the silica powder. Thus, the buildup of force chains among grains [34] does not lead to extended density correlations. It can be concluded that the nanotube powder is composed of aggregated bundles, being tens of micron in size. The strong van der Waals attraction amongst nanotube particles would facilitate such aggregation.

3.6 Acknowledgments

We thank Chris Duif at the Reactor Institute Delft for valuable discussions and help with performing experimental part of this work. We would like to thank Stefan Ludwig at the University of Twente for many valuable discussions and intellectual input contributing to this paper. The authors would like to thank Sander Brouwer at DelftChemTech for performing the N₂ porosimetry measurement on our silica powder. This work is part of the research programme of the 'Stichting voor Fundamenteel Onderzoek der Materie (FOM)', which is financially supported by the 'Nederlandse Organisatie voor Wetenschappelijk Onderzoek (NWO)'.

Chapter 4

Structure in cohesive powders studied with Spin-Echo Small Angle Neutron Scattering

This article, By Robert Andersson, Wim G. Bouwman, Stefan Luding and Ignatz M. de Schepper, was published by the scientific journal: Granular Matter. (<http://dx.doi.org/10.1007/s10035-008-0109-z>)

Abstract

Extracting structure and ordering information from the bulk of granular materials is a challenging task. Here we present Spin-Echo Small Angle Neutron Scattering (SESANS) measurements in combination with computer simulations on a fine powder of silica, before and after uniaxial compression. The cohesive powder packing is modeled by using molecular dynamics simulations and the structure, in terms of the density-density correlation function, is calculated from the simulation and compared with experiment. In the dense case, both quantitative and qualitative agreement between measurement and simulations is observed, thus creating the desired link between experiment and computer simulation. Further simulations with appropriate attractive potentials and adequate preparation procedures are needed in order to capture the very loose-packed cohesive powders.

4.1 Introduction

The macroscopic properties of a granular material are given by the mutual arrangement of the grains and its geometry, i.e., its structure. However, structure in granular materials is usually discussed in the framework of random sphere-packings [7], the classification and underlying theory describing the packings of grains are yet to be found, and more experiments are needed. The structure in granular materials is not only of fundamental importance, but also of great practical relevance in industry related applications. Powders with cohesive properties are widely handled throughout industry, either as a raw material, by-products, or as the desired end product. Considering fine powders (micro meter sized), inter-particle forces such as van der Waals, electrostatic and capillary forces influences the structure of the packing [82], leading to clustering [48], channelling and tunnelling effects in fluidised beds, and oscillating mass flows in general [76].

Various experimental methods to extract structural information in granular materials do exist. Magnetic Resonance Imaging has been proven successful in determining the structure of non-cohesive granular packings [70], and even dynamic measurements have been carried out [55]. Confocal microscopy has been applied to construct 3D images of granular materials immersed in a refraction-index matched liquid [75, 43]. X-ray computed microtomography followed by a tomographic reconstruction is a powerful 3D method that maps out the density in dry packings of, usually, model granular materials [5, 67, 71].

Cohesive powders are complex systems with a typical grain size not readily accessible with the techniques mentioned above. The use of conventional wave diffraction techniques such as Small-Angle Neutron Scattering (SANS) are commonly applied for the study of mesoscopic bulk structures (colloids, polymers, macromolecules etc.) [23]. The resolution of a conventional SANS instrument does not allow for the study of powders at the grain level, and one is usually limited to a few 100nm. At the Delft University of Technology a novel SANS technique has been developed [63, 64]. Spin-Echo Small Angle Neutron Scattering (SESANS) enables measurements over three orders of magnitude, ranging from 30nm-20 μ m in length [66], making this technique applicable for probing the bulk-structure in fine powders [1, 2].

Here we report measurements on a fine cohesive powder of silica before and after uniaxial compression. The measurement shows how larger structures disappear upon compression. In the loose-packed state we observe correlations extending far beyond the average size of a single grain. Molecular dynamics simulations were carried out in order to model the measurement. We find, in the dense case, good quantitative and qualitative agreement with the measurement. A loose packed sample is only in qualitative agreement, showing that more computational work is needed in order to capture the structures formed with low packing fractions.

4.2 Experiment, the sample and measured quantities

4.2.1 SESANS: Measured quantities

Spin-Echo Small Angle Neutron Scattering, SESANS, is based on the Larmor precession of neutrons in tilted magnetic fields [24], [79]. In SESANS, the polarisation of a neutron beam is measured, after transmission through a sample, as a function of the so-called spin-echo length, z ($30\text{nm} < z < 20\mu\text{m}$). The spin-echo length is the length at which density correlations are measured. The measured polarisation is directly related to the projection of the sample density-density correlation function along the neutron beam path. In particular, for a two-phase system we have, for the transmission of polarisation, normalised with experimental effects:

$$P(z) = e^{t\lambda^2\phi(1-\phi)\Delta\rho_0^2\xi(G(z)-1)} \quad (4.1)$$

where $G(z)$ is the normalised SESANS correlation function, representing the projection of the density-density correlation function of the sample (see Fig. 4.1). ϕ is the volume-fraction, t the sample thickness, λ is the neutron wavelength and finally we have $\Delta\rho_0$ being the neutron scattering length density (SLD) [73] difference between the two phases. We write the projection of the density-density correlation function, $\gamma(r)$, as:

$$G(z) = \frac{2}{\xi} \int_z^\infty \frac{r\gamma(r)}{\sqrt{r^2 - z^2}} dr \quad (4.2)$$

and

$$\gamma(r) = 2 \int_0^\infty \Delta\rho(r')\Delta\rho(r'+r)dr', \quad (4.3)$$

being defined so that $\gamma(0) = 1$. $G(z)$ is measured around the mean-square fluctuations of the sample inhomogeneities. Above the characteristic size of the sample inhomogeneities no more correlations are expected and therefore we have that $G(\infty) = 0$. The amplitude of the saturation level is

$$P(\infty) = e^{-t\lambda^2\phi(1-\phi)\Delta\rho_0^2\xi} \quad (4.4)$$

and depends on the correlation length ξ , the volume fraction ϕ of the sample inhomogeneities, on the chemical composition of the sample via $\Delta\rho_0$ and on the neutron wavelength $\lambda=2\text{\AA}$ as well as on the sample thickness t .

The correlation length of the sample inhomogeneities is:

$$\xi = 2 \int_0^\infty \gamma(r)dr \quad (4.5)$$

For a dilute gas of hard spheres we calculate $\xi = 3a/2$, with radius a . Note that the interaction between neutrons and the sample takes place on the SLD differences in the

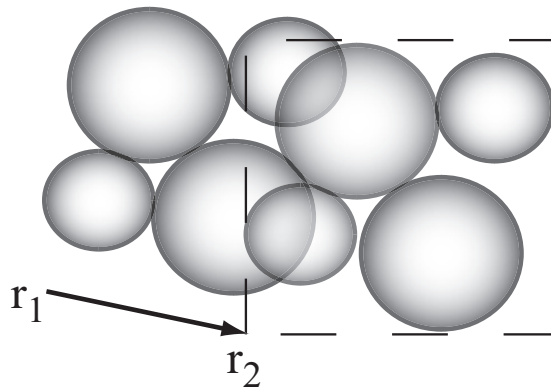


Figure 4.1: $\gamma(r)$ is the autocorrelation function of the density distribution. The correlation function $\gamma(r)$ depends on the shape/geometry and the structure of the sample. The function is a measure of the probability of being in the same phase after shifting from a point r_1 to a point r_2 in the sample ($r = |r_1 - r_2|$). This is equivalent to calculate the mean shared volume between an "image" and its ghost after shifting the ghost image some distance, r . For simple systems like a sphere and others, the correlation function is known analytically, but normally this function is calculated by numerical integration.

sample $\Delta\rho$, being in this study between air (treated as vacuum) and the silica spheres. Correlations are measured around the excess SLD along the beam and for systems with high packing fractions or ordered system $G(z)$ may even exhibit negative values due to the excluded volume at the vicinity of particle surfaces.

4.2.2 Sample and experiment

In the experiment we used a fine spherical silica powder, kindly provided by Kobo Products Inc. The manufacturer reported a wide lognormal size distribution with a peak at $3\text{-}4\mu\text{m}$ spanning across a decade. The density of the primary grain does not necessarily correspond to the density of the material making up that grain. We performed N_2 porosimetry measurements that concluded a primary grain density $\rho_g \simeq 0.45\text{g}/\text{cm}^3$ to be compared to $2.2\text{g}/\text{cm}^3$ for the density of pure silica. This density is in good agreement with the porosity stated by the manufacturer ($0.5\text{g}/\text{cm}^3$).

SESANS experiments were carried out on a hollow cylindrical sample container filled with powder of known mass. Two samples were prepared with the same thickness (5mm) but holding different mass of material, thus giving different volume fractions, $\phi \simeq 0.33$ and $\phi \simeq 0.75$ for the loose and the dense case respectively. The packing fractions are quoted in terms of their grain packing fractions, being

$$\phi = \frac{\rho_s}{\rho_g}, \quad (4.6)$$

where ρ_s is the density of the sample (i.e., mass powder per volume sample container).

A simple uniaxial compression was applied to prepare the sample. The straining of the powder was done by hand. The rate of straining was a few millimeters per second.

To produce the loose sample, $\phi \simeq 0.33$, we carefully rained the powder into a cylindrical mould and sealed it off with glass and aluminium windows (Aluminium and

quartz are transparent for neutrons).

The second measurement was conducted on a compressed sample, where the container was filled with more material, and the packing fraction was increased by compressing the powder along the neutron beam direction, $\phi \simeq 0.75$. We note that such a high packing fraction is possible due to the polydispersity in grain sizes. We also recognise an uncertainty in the measured porosity and in the determined volume-fractions, estimated to $\pm 5\%$.

The experiments were conducted in ambient conditions and the moist level in the powder was determined to be 13% by weight (6% by volume), determined by weighing before and after drying. A reasonable value, given the amount of surface available for moist-adsorption.

The microstructure of the loose packed sample will be mainly given by the attractive van der Waals and capillary forces, rather than be driven by gravitational body forces and hard core repulsion. We do not expect the loose packed sample to settle or undergo compaction during the measurement.

The samples were left for several hours in the neutron beam in order to improve statistics in the recorded spectra. Because of the long measurement time we monitored the stability (cracking, settling, compaction etc) of the powder packing by visual inspection throughout the measurement. No compaction was observed on the loose packed sample during the measurement and the dense sample appeared homogeneous as far as one can see by eye. The pressure applied on the dense sample was about 100kPa, determined by the constant weight acting on the plunger used to compress the powder.

A few points on the stress strain relationship for the powder was measured and is shown in Fig. 4.2. Plotting the volumetric strain ($\Delta V/V_0$, change in volume over initial volume) as a function of the logarithm of the stress shows a linear relationship. It is a soft powder, easily strained, with an initially very low grain packing fraction.

4.3 Molecular Dynamics: Method and model

The interaction between grains in a granular material involves deformations at the contact point and in certain cases an attraction in the form of van der Waals attraction, capillary forces and electrostatic forces. Any computational attempt that convincingly models all possible interactions and deformations would be, to say the least, time consuming. Therefore we relate the interaction force to the overlap between particle pairs and particles interact only at contact (i.e., short-range forces). We used Molecular Dynamics simulations (MD) [61], [47], [49] to model the experiment. From the MD generated particle configuration we are able to calculate the corresponding SESANS correlation function $G(z)$ according to Eq. (4.2), and finally the expected polarisation with Eq. (4.1).

The MD code uses a linear hysteretic contact law, which allows for attractive/cohesive forces upon unloading [47], [49], see Fig. 4.3. Three stiffness parameters govern the

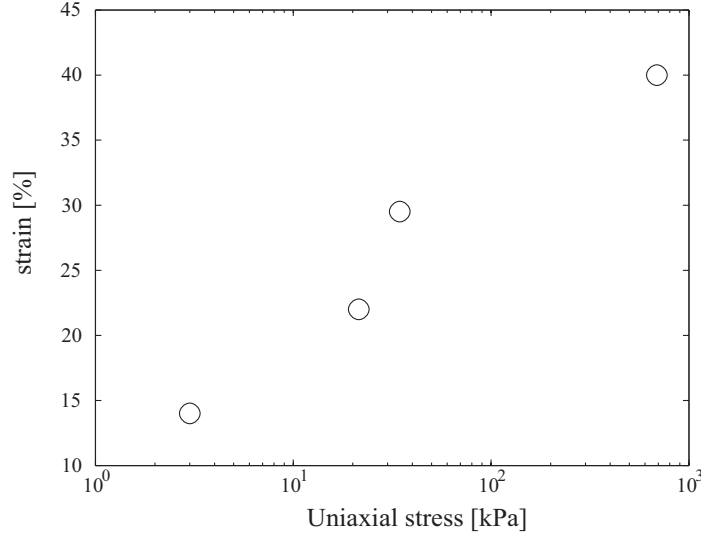


Figure 4.2: Stress-strain curve obtained from uniaxial compression experiments on the silica powder.

particle-particle contact model; k_1 , k_2 and k_c for loading, unloading and cohesive stiffness respectively. The initial loading path follows a linear increase $k_1\delta$ until a maximum overlap δ_{max} is reached where δ_{max} is a history parameter to be updated for each load cycle. For unloading, the force decreases along $k_2\delta$ until δ_0

$$\delta_0 = (1 - k_1/k_2)\delta_{max}. \quad (4.7)$$

Attractive/adhesive forces are activated when unloading below δ_0 . The force can be cast into one equation:

$$f^h = \begin{cases} k_1\delta & \text{loading, if } k_2(\delta - \delta_0) \geq k_1\delta \\ k_2(\delta - \delta_0) & \text{un/reload, if } k_1\delta > k_2(\delta - \delta_0) > k_c\delta \\ -k_c\delta & \text{unloading, if } -k_c\delta \geq k_2(\delta - \delta_0) \end{cases} \quad (4.8)$$

To allow for a stable integration of the equations of motion the timestep was chosen so that it resolves about 70 times the typical contact duration time, t_c , between a typical particle pair.

$$t_c = \frac{\pi}{\omega} = \frac{\pi}{\sqrt{k_2/m_{12} - \eta^2}}, \quad (4.9)$$

where ω is the eigen-frequency of the contact, k_2 the stiffness, $m_{12} = m_1m_2/(m_1 + m_2)$ the reduced mass of the particle pair and $\eta = \gamma/(2m_{12})$ a damping coefficient. Energy is dissipated upon particle contacts and collisions, and also through the viscous damping coefficient γ , which (alone) leads to the coefficient of restitution, r_c :

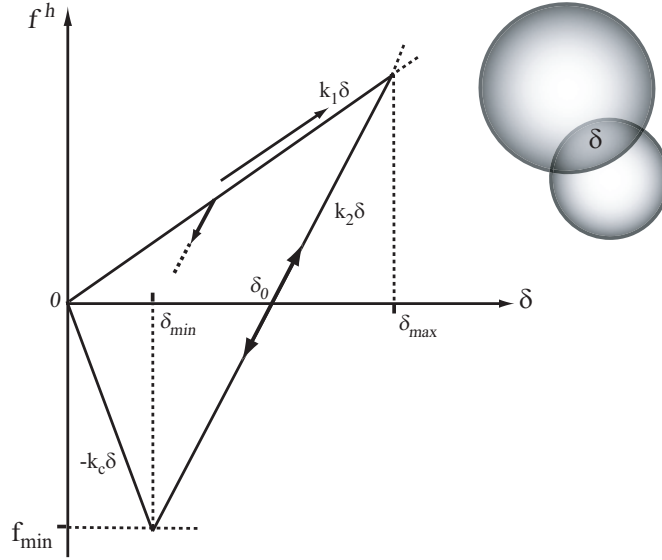


Figure 4.3: Linear hysteretic force model. The left illustrates that at the contact point between two particles plastic deformations takes place in the form of permanent overlap. Unloading below δ_0 gives rise to attraction between contacting pairs. The figure to the right shows two particles in contact producing an overlapping region.

$$r_c = v'/v = \exp(-\eta t_c) \quad (4.10)$$

where v and v' denotes the particle velocity before and after a collision respectively.

The particle size-distribution was chosen to be lognormal distributed with a mean at $3\mu\text{m}$ in terms of a sphere diameter ($R_{max}/R_{min}=15$), see Fig. 4.4. The particles was divided into five size-classes, indicated by the horizontal lines in Fig. 4.4, each holding a range of sizes of the lognormal distribution. The average coefficient of restitution for each size-class was set around $r_c = 0.85$ by giving the particles different stiffness depending on their size.

Coulomb's law gives the tangential forces acting between particles, so that in the static case the tangential force is given by a static friction coefficient i.e., $f^t \leq \mu_s f^n$ and the sliding case is governed by a dynamic counter part $f^d = \mu_d f^n$. In general the relationship is $\mu_d \leq \mu_s$ and we use $\mu_d = \mu_s = 0.4$.

An artificial background viscosity to dissipate the long-wavelength modes of motion is added; this damping can be attributed to a dispersion medium such as air, thus giving it a physical meaning rather than just enhancing the efficiency of the simulation [47].

The MD simulation carried out here contains two steps. First the initial preparation where we go from a packing fraction $\phi = 0.08$ configuration to $\phi = 0.33$ by increasing the radius of the particles. For an assembly of N spheres with radius a contained in volume V we have $\phi = V^{-1} \sum_i^N 4/3\pi a_i^3$. This preparatory step is followed by a uniaxial compression until we reach $\phi = 0.75$. Table 4.1 summarizes the material properties and simulation characteristics at the start of wall movements. It is beyond the scope of this

Table 4.1: Material parameters and simulation parameters used in the MD simulation at the start of the wall movement. The stiffness and viscosity parameters are averages. [‡]This is the average distance that the particles have travelled from the start of the simulation. [†] The timestep of the integration is chosen so that it can resolve the duration of a particle contact.

Parameter	Meaning	MD unit	SI unit (prefixed)
t	time unit	1	1 μ s
l	length unit	1	1m
m	mass unit	1	1kg
$\langle D \rangle$	mean particle diameter	3×10^{-6}	3 μ m
δ	particle density	500	500kg/m ²
V	total volume	3×10^{-12}	3×10^{-3} mm ³
$\langle t_c / \Delta t \rangle^\dagger$	particle contact response time over MD timestep (average)	70	-
$\langle l_{end} \rangle / \langle D \rangle^\ddagger$	particle dist. travelled	900	0.9mm
ϕ	packing fraction	0.33	-
k_2	elastic stiffness	2×10^{-7}	2×10^5 kg/s ²
k_1	plastic stiffness	$0.2k_2$	
k_c	cohesive stiffness	$10k_2$	
k_t	friction stiffness	$0.2k_2$	
k_r	rolling stiffness	$0.2k_2$	
k_s	spinning stiffness	$0.2k_2$	
$\mu_d = \mu_s$	Coulumb friction coefficient	0.4	
μ_r	rolling friction	μ_d	
γ_n	viscosity (normal)	1×10^{-12}	1×10^{-6} kg/s
γ_f	viscosity (tangential)	$0.25\gamma_n$	
γ_r	viscosity (rolling)	$0.25\gamma_n$	
γ_s	viscosity (spinning)	$0.25\gamma_n$	
γ_{bgt}	visc. acting on translations (background)	$0.1\gamma_n$	
γ_{bgr}	visc. acting on rotations (background)	$0.05\gamma_n$	

paper to discuss all parameters, details about the parameters can be found in [49].

4.4 Results

4.4.1 Results: SESANS Experiment

We have used the SESANS setup at the Delft University of Technology to perform the SESANS experiments shown here. Two experiments were carried out on a loosely packed sample ($\phi = 0.33$) and on a uniaxially compressed powder ($\phi = 0.75$) of porous spherical silica particles.

We note that the loose-packed sample shows (see the bottom figure in Fig. 4.5) correlation extending beyond the measured scale, indicating inhomogeneities above four particle diameters, see Fig. 4.5. The experimental result for the loose packed sample contain two seemingly linear branches (separated at $z=2\mu$ m). This behaviour cannot be explained by any simple scaling or power laws. We attribute this to originate from different scales present in the powder, being the size of grains (3μ m) and the size of clusters of grains ($>12\mu$ m).

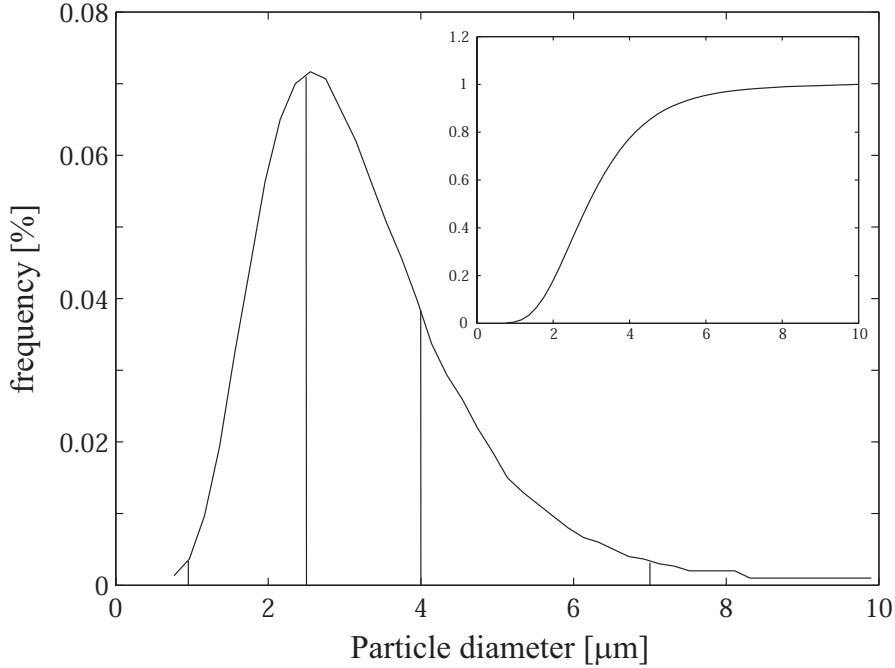


Figure 4.4: The lognormal size distribution used in the simulation. The inset shows the cumulative probability distribution of sizes

The longer ranged correlations are credited to the presence of clusters and voids with an average size above four particle diameters. Upon compacting, one expects the clusters to break up and voids will collapse. As can be seen in the top figure in Fig. 4.5 we reach a saturation in the correlations $\simeq 3\mu\text{m}$ for the dense sample with $\phi = 0.75$, we attribute this size to the diameter of the particles, reported to be centred at $3\mu\text{m}$. The applied stress does not only break clusters and collapse voids, but it also give rise to excluded volume correlation among the grains as seen in the small dip around $2\text{-}3\mu\text{m}$.

The amplitude of the saturation is proportional to the correlation length ξ and the packing fraction ϕ of inhomogeneities in the sample according to Eq.(4.4) and Eq.(4.5). Since the loose-packed sample never shows any saturation on the measured scale, it is hard to draw any quantitative conclusions; however, we note that the saturation level is below that of the compact sample leading to a higher correlation length, which is to be expected for a sample with larger voids.

4.4.2 Results: Molecular Dynamics

We have used the MD method described in a previous section to carry out a uniaxial compression test on a low-volume fraction (33%) cohesive powder packing. Simulations were carried out using a periodic cuboid undergoing a cosinusoidal (half period) compression along one dimension in zero gravity. The initial state was a random granular gas of low volume fraction ($\phi = 0.08$); with a gaussian velocity distribution and in total

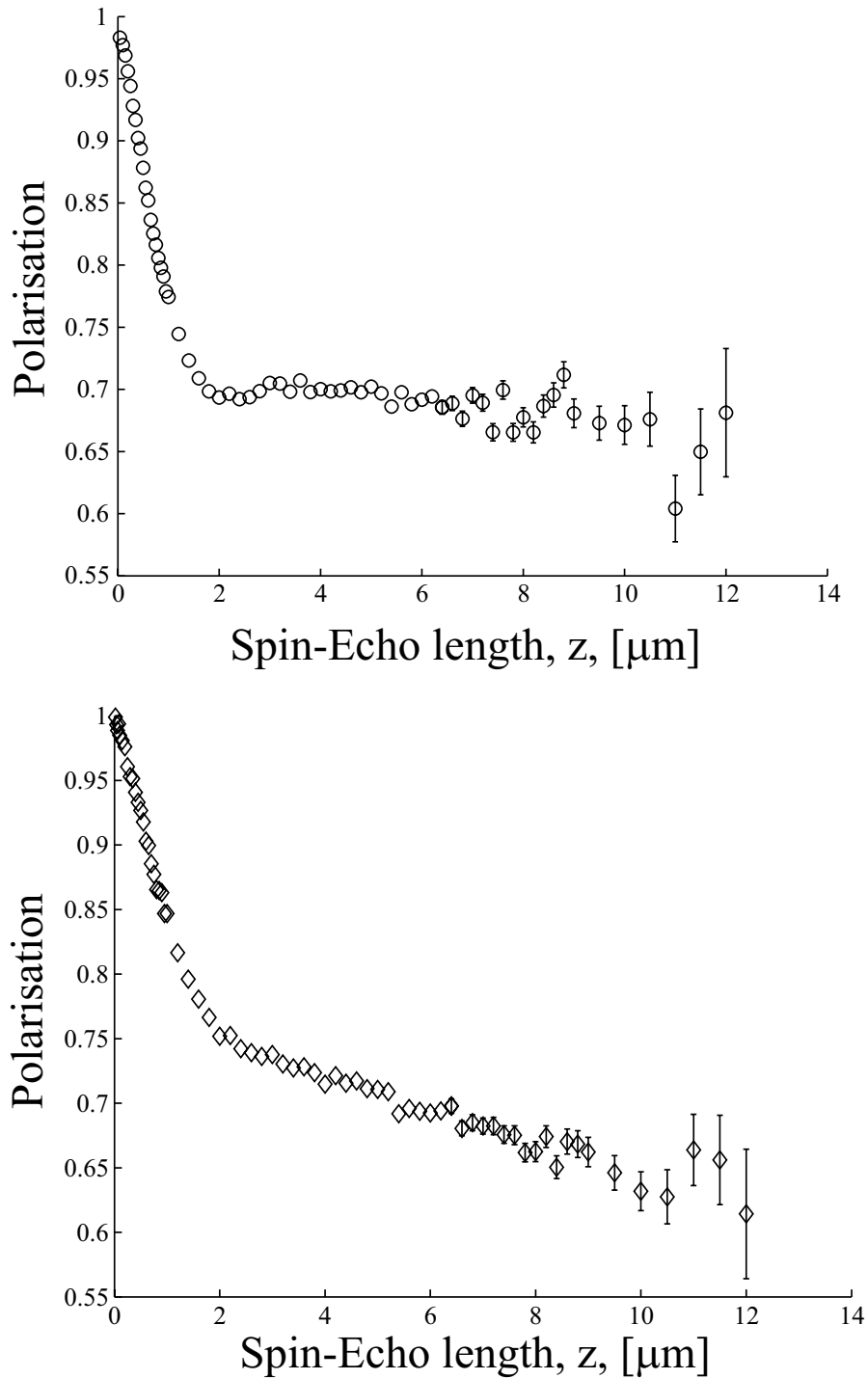


Figure 4.5: Measurements on fine powders of silica, polarisation, $P(z)$, as function of spin-echo length z . The topmost plot is results obtained from the *dense*-packed sample and the lower figure represents the loose-packed sample. If not shown, all errors fall within markers.

carrying 3000 particles. The initial state was allowed to grow (without compromising the size distribution) until a specified volume fraction was reached at $\phi = 0.33$, and the final radius was $1.5\mu\text{m}$. On average the particle has travelled 900 average particle diameters at the end of the growth process. At this stage the simulation should represent the loose-packed sample in our experiment, holding a low volume fraction in a more clustered or open structure. We note that at the end of the simulation at $\phi = 0.33$ the packing is not stable, but containing residual kinetic energy.

The loose-packed sample was compressed along one dimension to yield the final compressed state at $\phi = 0.75$, for an illustration of the packings, see Fig. 4.7. In general, we conclude from Fig. 4.6 that the shapes of the curves are rather well reproduced when comparing the simulation with the experiments. The excluded volume feature seen in the experiment is also seen in the simulation in the dense case.

For the compressed state we calculate the correlation length to $\xi=1\mu\text{m}$, representing the typical size of inhomogeneities projected along the neutron beam, this is in excellent agreement with our measurement when taking into account the measured volume fraction, known SLD, the neutron wavelength and the sample thickness. The correlation function saturates on the horizontal axis around $z=3\mu\text{m}$ and this size represents the typical diameter of the spherical grains. All together, giving good agreement in both shape and amplitude of the polarisation in the dense case.

When comparing the uncompressed and compressed state in terms of $G(z)$ we note that the dense packing show a faster decay in the correlations thus, representing a sample with shorter range in correlations, in essence a more closed system with smaller inhomogeneities.

For the simulation representing a loose-packed structure the calculated polarisation does not reproduce our experiment; however, we clearly see a correlation function with a good qualitative agreement in the overall shape (see the lower-left figure in Fig. 4.6). Note also the slope seen for higher z in the experiment and seen in simulation on the loose-packed sample. The amplitude of the polarisation is given by the total amount of scattering according to Eq. (4.4) where mainly ξ contributes to the amplitude (the other terms are constants, and $\phi(1-\phi)$ in this case, gives only a minor contribution. We extract from our simulation a correlation length, ξ , of $2.5\mu\text{m}$ and $1\mu\text{m}$ for the loose and dense packing respectively. For a hard sphere gas we have $\xi=1.5$ times the sphere radius. We expect this correlation length to drop with increasing packing fraction.

We explain the discrepancy between measured and simulated polarisation on the loose packing by arguing that: in the experiment, we have a two-phase system of low/empty and -high density phases of particles so that the high-dense regions will contribute to a low-scattering amplitude via low ξ and the low packing fraction is given by the large voids. At low length scales, $0.1\mu\text{m} \leq z \leq 3\mu\text{m}$, when comparing the experiment with our simulation result, we see in Fig. 4.6 a steeper slope in the correlation function (i.e., a more close-packed structure) and the argument here is that dense regions are giving this behaviour. When we further compress the system we expect, at some stage, all clusters to break and larger voids to collapse, all together

giving a final random dense-packing of polydisperse spheres.

4.5 Conclusions

The use of spin-echo small angle neutron scattering for the study of structure in fine powders captures the structural differences in terms of the correlation function between loose and dense packings. The SESANS correlation function can be calculated from molecular dynamics simulations and compared with experiments. For the dense packing, we obtain a good quantitative agreement between measurements and simulations, whereas a qualitative agreement is obtained for the loose-packed system. In the loose packing we see no saturation of the correlations at larger length scales both in simulation and in experiment.

The SESANS correlation function is directly related to the density-density distribution function of the sample, through the projection along the neutron beam path. SESANS captures the transition between a loosely packed powder and a dense packing via a hard-core repulsion (excluded volume) feature in the correlation as well as in the correlation length and the overall curve-shape. The average size of the inhomogeneities can be extracted from the correlation function in the form of correlation length, ξ . The experiments show that the dense packing carries lower correlation length when compared to the loosely packed sample. This is expected, since the loose packed sample would mean a higher degree of clustering, giving rise to inhomogeneities and voids at larger length scale (this can also be concluded by visual inspection and by the fact that no saturation is observed). Interestingly, the correlations do not extend beyond the size of a grain in the dense packing. One expects the dense case to carry so called force networks, these networks (if they are present in the packing) do not create correlations in the density distribution.

The lognormal size distribution, used in the simulation, leads to the loss of excluded volume effects and nearest-neighbour peaks in the correlation function, thus contributing to the agreement between measurement and the simulation.

We acknowledge that the structure of the loose packed sample was not reproduced in our simulation. A stronger clustering mechanism than used in the simulation is needed, possibly by introducing an attractive potential. The simulation predicts a higher correlation length for the uncompressed state, which is expected for a more open and porous system. The total amount of neutron scattering and the correlation length is over-estimated when compared to our experiment. We argue that in the loose packed experiment we have a two-phase system with large voids and large dense-clusters of particles (sub-millimeter sized). The dense clusters of particles would, in this case, contribute to a low correlation length and the voids give rise to the low packing fraction seen in the experiment.

We believe to have made a valuable connection between simulations and experiments, showing that in dense sphere packings with wide size distributions, the proposed MD model is in excellent agreement with the experiment. For loose cohesive powders,

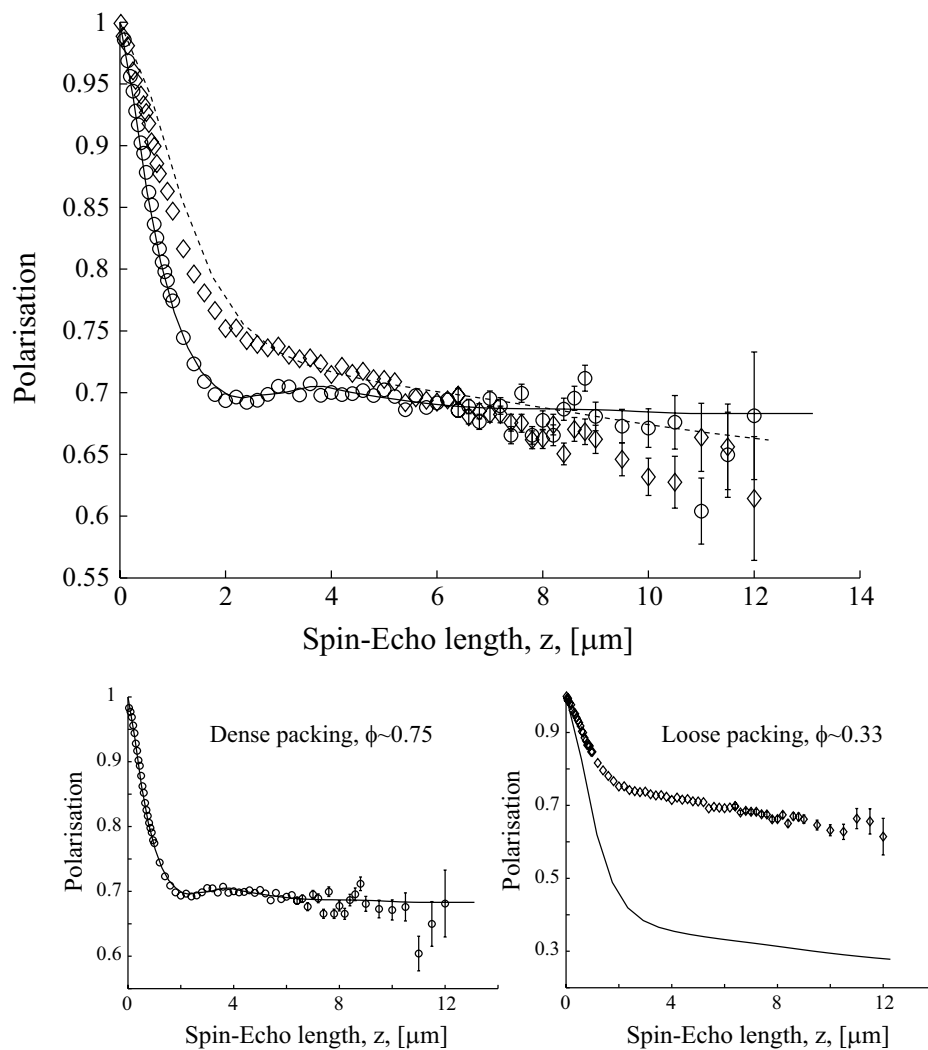


Figure 4.6: Experimental and MD-simulation results. The top figure represents all measured and simulated results. Note that in the clustered case (diamonds) the simulation result (dashed line) is re-scaled to collapse on the measured points. We separate the two cases at the bottom and note only a qualitative agreement, on the shape, between the simulation and experiment for the loose-packed sample (rightmost figure). On the *dense*-packing we see a good quantitative agreement between measurement and simulations (leftmost figure). If not shown, all errors fall within the markers.

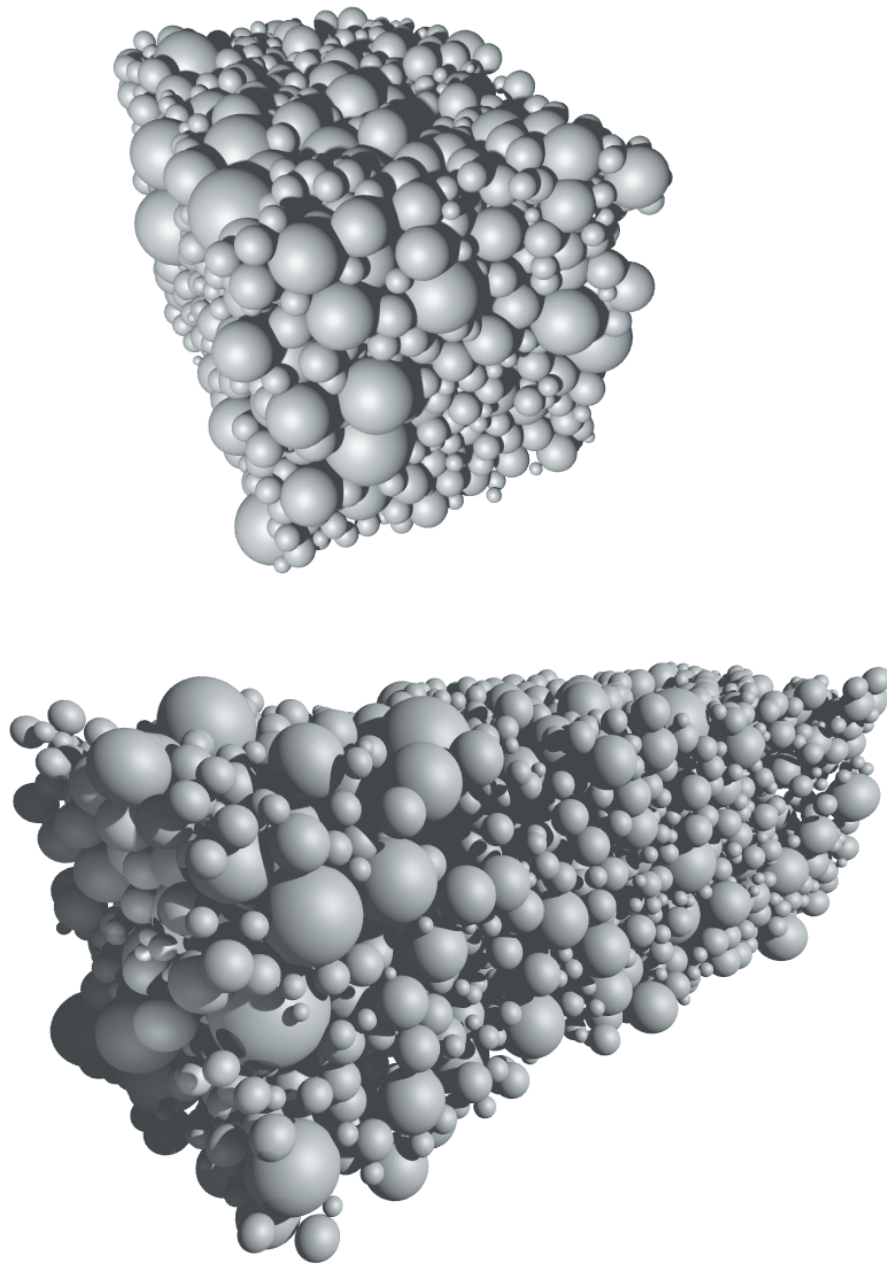


Figure 4.7: Visualisation of: Top, the final compressed packing ($\phi = 0.75$) and bottom, the initial loosely packed state ($\phi = 0.33$).

we need new models and larger simulations if we want capture the structure seen in real experiments.

Acknowledgements

We thank Chris Duif at the Reactor Institute Delft for valuable discussions and help with performing the experimental part of this work. The authors would like to thank Sander Brouwer at DelftChemTech for performing the N₂ porosimetry measurement on our silica powder. This work is part of the research programme of the 'Stichting voor Fundamenteel Onderzoek der Materie (FOM)', which is financially supported by the 'Nederlandse Organisatie voor Wetenschappelijk Onderzoek (NWO)'.

Summary

Microstructure in powders

Spin-echo small-angle neutron scattering measurements

By Robert Andersson

Industrial relevance, fundamental interest, and a curiosity sparked by a very rich phenomenology, have turned the scientists towards the study of powders and granular materials. Also, next to water, granular matter is the most manipulated and processed state of matter found. The basic unit of a granular material is the grain –in the same way as the water molecule is the basic unit of water –the gold atom is for the gold ring, and so on. The grains in a granular material interact through the action of force. Forces can have their origin in gravity, meaning that the mass of the grain give rise to a body force acting on other grains, which acts on other grains and so on. Other forces are electrostatic in nature, for example, the van der Waals force which is, essentially, related to surfaces in contact. For powders made up of smaller grains, e.g., less than $100\mu\text{m}$ in diameter, the van der Waals force becomes the dominant one (i.e., its strength exceeds that of gravity). A liquid capable of wetting the grains is another important source of grain-grain attraction, and such capillary forces can cluster truly macroscopic sized grains; for example, millimeter sized particles. When the attractive forces dominate the grain-grain interaction the powder is classified as being cohesive. The grains are otherwise impenetrable and their mutual arrangement, size and shapes makes up what is called the microstructure of the granular material.

This thesis presents a series of bulk microstructural experiments made on cohesive powders alongside with phenomenological modelling and molecular dynamics simulations. The modelling serves as explanations of the experimental observations. The measurements were carried out with neutrons, using their penetrating capability to see the powders from the inside; and this in a spin-echo small angle neutron scattering (SESANS, spin-echo small-angle neutron scattering) setup at the Reactor Institute Delft at Delft University of Technology –the Netherlands. This particular scattering technique uses the Larmor precession of neutrons in magnetic fields in order to ‘determine’ the scattering ‘angles’. The instrument, which uses a polarised neutron beam, contains two identical magnetic field regions situated before and after the sample position. Any neutron scattering at the sample breaks this symmetry, and this gives rise to depolarisation of the neutron beam. The SESANS machine measures the projection of the autocorrelation function of the density distribution of the sample, i.e., it measures its microstructure. The motivation of constructing a SESANS instrument is to increase the momentum resolution so that the study of micron sized domains is possible. This thesis shows SESANS applicability on realistic samples –samples for which it was built for.

Many of the correlation functions, phenomenological or theoretical, describing a variety of density distributions, particle types etc. were investigated and, finally, their

corresponding SESANS formalism was developed. These calculations yielded, when possible, an analytical result or were carried out as a numerical calculation or method. All together, a toolbox for the analysis of SESANS data was developed during this thesis work.

The powders used in the experiments were mainly made of silicone dioxide (SiO_2), carrying a broad distribution of grain sizes. From the experiments it was concluded that the density distribution is disordered at a wide range of packing fractions. No ordering was observed in the microstructure and a single length scale was enough to attribute a size to the microstructure. This is the typical size of the density fluctuations and it was shown that this does not exceed the average particle size; the only exception was observed for the very loose packed samples, where particle clustering extends the density correlations. Compressing the powders leads to a decrease in the range of correlations, i.e., the typical size of the density fluctuations decreases. In particular in one experiment, the evolution of the microstructure was followed during a stress versus (compressive) strain experiment. The non linear behavior of the macroscopic stress versus strain could be traced back to the similar microscopic relationship, since the measured correlation length was observed experimentally as a function of strain.

A relatively simple phenomenological correlation function could be used to fit many experiments. This model is based on a self-affine description of the density distribution; a model parameterised by the so called Hurst exponent and with a finite size, related to the typical size of the density fluctuations. This model provides an analytical solution to the measured SESANS projection, the correlation function itself, and also to the corresponding wavenumber-domain spectrum.

Anisotropy in the density distribution of a uniaxial compressed powder was investigated too. This concluded that when grains are isotropic in their geometry, the uniaxial compressed powder remains isotropic in the overall density distribution. A similar experiment was carried out using anisotropic primary grains (nanotube powder), which resulted in an anisotropic density distribution in the final uniaxially compressed state.

Molecular dynamics computer simulations were carried out to model a uniaxial compression of a 'isotropic' cohesive powder. The simulation showed good agreement on the dense packing fraction, i.e., after compression of the powder. A quantitative agreement was seen between the simulation and the experiment at a packing fraction above 70%. The lower unperturbed, uncompressed and loosely packed powder saw a qualitative agreement in terms of the curve shape. Stronger attraction between grains in the model would enable the creation of fractal aggregates, which would have lead to better agreement. The study shows that improvements in models are needed.

Sammanfattning

Microstruktur i pulver

Spin-echo small-angle neutron scattering mätningar

Av Robert Andersson

Industriell relevans, fundamentalt intresse och en nyfikenhet, väckt av en rik fenomenologi, har vänt vetenskapens blickar mot studiet av pulver och andra granulära material. Också, vid sidan av vatten så är de granulära materialen de mest manipulerade och bearbetade materialen på jorden. Den grundläggande enheten som beskriver ett granulärt material är kornet (den mikroskopiska partikeln), på samma sätt som H_2O är vattnets grundläggande enhet, guldatomen är guldringens osv. Partiklarna som bygger upp det granulära materialet växelverkar genom utövandet av kraft. Krafter kan ha sitt ursprung i gravitationen, vilket betyder att partikelns massa ger upphov till en volymkraft som verkar på angränsande partiklar vilka i sin tur verkar på andra partiklar osv. Krafter kan också ha sitt ursprung i elektrostatiske växelverkan, t.ex. van der Waals kraften, vilken är mer eller mindre relaterad till ytor i kontakt. För pulver material som består av mindre partiklar ($100\mu m$ eller mindre) kan van der Waals kraften bli den mer dominant (dvs. dess styrka överkommer gravitationen). En annan viktig källa för interaktion mellan makroskopiska partiklar är kapillärkrafter. Kapillärkrafter uppstår då en vätska som kan väta partikelns yta ansamlas i gränssnittet mellan partiklar. Kapillärkraften kan aggregera verkligt makroskopiska partiklar, t.ex. millimeter stora korn. Då attraktiva krafter dominerar interaktionen mellan partiklar i ett pulvermaterial talar man om ett kohesivt pulver (cohesive powders). Partiklarna är annars openetrerbara och deras ömsesidiga arrangemang, storlek och form bygger upp vad som kallas mikrostrukturen av det granulära materialet eller pulvret.

Denna avhandling behandlar mikrostrukturella under-sökningar av kohesiva pulver och med fenomenologisk modellering och 'molecular-dynamics' datorsimuleringar. Modelleringen och simuleringarna har för avsikt att förklara de experimentella observationerna. Experimenten utfördes med hjälp av neutroner, där deras penetrerande egenskaper använts för att se materialen från 'insidan'. Tekniken kallas spin-echo small-angle neutron scattering (SESANS, spin-echo small-angle neutron scattering) och instrumentet finns på Reactor Institute Delft vilket är en del av Technische Universiteit Delft. Denna neutron spridnings teknik använder neutronens förmåga att rotera (Larmor precession) i ett magnetfält. Instrumentet använder polariserade neutroner och består av två identiska magnetiska fält, formade som parallelogram, placerade före och efter prov-miljön. I det fall då provet ger upphov till neutronspridning registreras detta som depolarisering av neutronstrålen. SESANS mäter provmaterialets mikrostruktur genom projektionen av autokorrelationen av provets densitets-distribution (eller autokorrelationen av materialets projekterade densitetsdistribution). SESANS är utvecklad för att möjliggöra studier av strukturer i mikrometer domänen och uppåt, alltså relativt stora strukturer. SESANS är ett sätt att öka momentum-resolutionen i small-

angle neutron scattering. Denna avhandling visar SESANS tillämplighet för studier av realistiska material – material som SESANS var byggt för att kunna studera.

Flera av de korrelationsfunktioner, fenomenologiska och teoretiska, som beskriver en rad densitets distributioner, partikel typer etc. har undersökts i detta arbete, och en korresponderande SESANS formalismen har utvecklats. Beräkningarna gav många gånger ett analytiskt resultat men då det inte var möjligt så undersöktes resultaten numeriskt. Sammantaget så har en “verktygslåda” för SESANS dataanalys utvecklats under detta arbete.

De pulver som använts i experimenten var av kiseldioxid (SiO_2) och oftast hållande en bred distribution av partikelstorlekar. Experimenten visade att densitetsdistributionen är oordnad över en rad volymfraktioner. Ingen organisering av partiklar kunde påvisas och endast en längd var tillräckligt för att tillskriva mikrostrukturen dess storlek. Detta är den karakteristiska storleken på densitets-fluktuationerna och denna storlek överstiger inte storleken på partiklarna som bygger upp pulver materialet. Endast i särskilda fall observerades korrelationer över längder som översteg storleken på pulver partiklarna, detta återfanns vid låga volymfraktioner där kluster av partiklar förlänger korrelationen. Då pulvret komprimeras genom tryck så leder detta till en minskning av korrelationernas räckvidd, storleken på densitetsfluktuationerna avtar då volymfraktionen material ökar. Speciellt i ett experiment så följdes mikrostrukturens evolution under ett kompressivt-dragprov. Det icke-linjära makroskopiska beteendet mellan tryck och kompression som observerades kunde spåras till en liknande mikroskopisk relation. Korrelationslängden följdes alltså i SESANS experimentet som funktion av kompression.

En relativt enkel fenomenologisk modell och funktion kunde användas för att anpassa de mätta punkterna. Modellen beskriver ett s.k. ‘self-affine material’, en modell parametriserad med en Hurst-exponent och en längd som beskriver den karakteristiska storleken av mikrostrukturen. Funktionen som beskriver autokorrelationen av densitets distributionen leder också till en analytisk lösning av dess projektion såväl. Också distributionens spectrum i reciprokal rymd är analytisk.

Anisotropi i densitetsdistributionen av uniaxialt komprimerade pulver studerades också. Experimenten konkluderade att i de fall då pulver-partiklarna var isotropiska då förblir också den totala densitetsdistributionen isotropisk efter uniaxial kompression. Ett liknande experiment utfördes på ett pulver av anisotropiska partiklar (nanotube powder), detta resulterade i en anisotropisk densitetsdistribution efter uniaxial kompression.

Datorsimuleringar baserade på Molecular Dynamics utfördes med syftet att modellera en uniaxiell kompression av ett ‘isotropiskt’ kohesivt pulver. Simuleringen visade god överensstämmelse med experimentella observationer vid högre volymfraktioner – alltså efter kompression. En kvantitativ överensstämmelse sågs mellan simulering och experiment vid en volymfraktion över 70%. Vid lägre volymfraktion, okomprimerad, ostörd och löst packat pulver återfanns endast en kvalitativ överensstämmelse. Starkare attraktion mellan partiklarna i datormodellen skulle leda till ett bättre resultat. Stu-

dien visar att datormodeller måste förbättras.

Samenvatting

Microstructuur in poeders

Spin-echo small-angle neutron scattering metingen

Door Robert Andersson

Industriële toepasbaarheid, fundamentele interesse, en nieuwsgierigheid die gevoed wordt door een rijke fenomenologie, hebben wetenschappers tot het bestuderen van poeders en granulaire materialen aangezet. Bovendien is na water, granulaire materie de meest voorkomende gemanipuleerde en bewerkte toestand van materie. De basis eenheid van granulair materiaal is de korrel - op dezelfde manier als het water molecuul de basis eenheid van water is - het goud atoom dat voor de gouden ring is, enzovoort. De korrels in een granulair materiaal wisselwerken door het optreden van krachten. Een van de krachten wordt veroorzaakt door de zwaartekracht, hetgeen betekent dat de massa van de korrel aanleiding geeft tot een kracht van de korrel op andere korrels, welke weer op andere korrels krachten uitoefent, enzovoort. Andere krachten zijn elektrostatisch van aard, bijvoorbeeld de van der Waals krachten, welke, in essentie, evenredig zijn met de contactoppervlakken tussen de korrels. Voor poeders die uit kleinere korrels bestaan, d.w.z., minder dan $100\ \mu\text{m}$ in diameter, is de van der Waalskracht de dominante kracht (dat betekent dat deze kracht sterker is dan die van de zwaartekracht). De aanwezigheid van een vloeistof die de korrels bevochtigt, is een andere belangrijke bron van aantrekking tussen korrels, en zulke capillaire krachten kunnen de korrels doen clusteren tot werkelijk macroscopische afmetingen, bijvoorbeeld tot deeltjes met een grootte in de orde van enkele millimeters. Wanneer de aantrekkende krachten de korrel-korrel interactie domineren, wordt het poeder geclassificeerd als zijnde cohesief. De korrels zijn verdere onvervormbaar en hun wederzijdse rangschikking, grootte en vorm bepalen de microstructuur van het granulaire materiaal.

Dit proefschrift presenteert een serie microstructuur experimenten van cohesieve poeders, samen met het fenomenologisch modelleren en simuleren met zgn. moleculaire dynamica simulaties. Het modelleren dient om verklaringen te vinden voor de experimentele waarnemingen. De metingen zijn uitgevoerd met neutronen, waarbij hun doordringende vermogen gebruikt is om de poeders van binnenuit te bekijken. Meer specifiek heeft dit plaatsgevonden in een spin-echo kleine hoek neutron verstrooiingsapparaat (SESANS, spin-echo small-angle neutron scattering) op het Reactor Instituut Delft van de Technische Universiteit Delft. Deze bijzondere verstrooiingstechniek gebruikt de Larmor precessie van neutronen in magnetische velden om 'de verstrooiingshoeken te bepalen'. Het instrument, waarin gepolariseerde neutronen worden gebruikt, bevat twee identieke magnetische veld gebieden, waarvan er zich n voor en één voor en een achter het te onderzoeken sample bevindt. Elke verstrooiing van een neutron in het sample verbreekt de symmetrie van de afgelegde paden en veroorzaakt depolarisatie van de neutronen bundel. De SESANS machine meet de projectie van de autocorrelatie functie van de dichtheidsdistributie van het sample, d.w.z., het meet zijn microstruc-

tuur. De motivatie om een SESANS instrument te ontwikkelen lag in de wens om de impuls resolutie te vergroten, zodat de studie van domeinen in de orde van een micrometer mogelijk zou worden. Dit proefschrift toont de toepasbaarheid van SESANS voor realistische samples - samples waarvoor het was ontwikkeld.

Veel van de correlatiefuncties, fenomenologisch en theoretisch, die een veelheid van dichtheidsverdelingen, deeltjes typen, etc., beschrijven, werden onderzocht en uiteindelijk werd hun corresponderende SESANS expressie ontwikkeld. Waar mogelijk leverden deze berekeningen analytische resultaten op of ze werden uitgevoerd als numerieke berekening of methode. Al met al werd gedurende deze promotietijd een gereedschapskist voor de analyse van SESANS gegevens ontwikkeld.

De poeders die in de experimenten zijn gebruikt, bestonden hoofdzakelijk uit silicium dioxyde (SiO_2), over een groot bereik van korrel groottes. Uit de experimenten werd geconcludeerd dat de dichtheidsverdeling niet-geordend is in een groot gebied van pakkingsfracties. Er werd geen ordening waargenomen in de microstructuur en een enkele lengteschaal was genoeg om een grootte toe te kennen aan de microstructuur. Dit is de kenmerkende grootte van de dichtheid fluctuaties en het werd aangetoond dat deze de gemiddelde deeltjes grootte niet overschrijdt; de enige uitzondering werd waargenomen voor zeer luchtig opeengestapelde samples, waar het klonteren van deeltjes de dichtheidscorrelaties groter maakt. Het samendrukken van de poeders leidt tot een afname van de correlaties, d.w.z., de typische afmetingen van de dichtheidsfluctuaties neemt af. In één experiment in het bijzonder werd de evolutie van de microstructuur gevolgd tijdens een spanning versus (compressieve) vervorming experiment. Het niet-lineaire gedrag van de macroscopische spanning tegen vervorming kon teruggevoerd worden naar de gelijkwaardige microscopische relatie, omdat de gemeten correlatielengte experimenteel waargenomen was als een functie van de vervorming.

Er kon een betrekkelijk eenvoudige fenomenologische correlatiefunctie gebruikt worden voor het fitten van veel van de experimenten. Dit model is gebaseerd op een zelfbevestigende beschrijving van de dichtheidsdistributie; een model dat geparametriseerd is door de zgn. Hurst exponent en met een eindige grootte, gerelateerd aan de typische grootte van de dichtheidsfluctuaties. Dit model verschaft een analytische oplossing voor de gemeten SESANS projectie, de correlatiefunctie zelf, en ook voor het corresponderende golfnummer-domein spectrum.

De anisotropie in de dichtheidsdistributie van een uniaxiaal samengepersd poeder werd ook onderzocht. Hieruit werd de conclusie getrokken dat wanneer de korrels in alle richtingen dezelfde geometrie hebben (isotroop zijn), de uniaxiaal samengepersde korrels isotroop blijven in de globale dichtheidsdistributie. Een vergelijkbaar experiment is uitgevoerd waarin anisotrope korrels werden gebruikt (nanotube poeder), wat resulteerde in een anisotrope dichtheidsdistributie in de uiteindelijke uniaxiaal samengepersde toestand.

Moleculaire dynamica computersimulaties werden uitgevoerd om de uniaxiale compressie van een 'isotroop' cohesief poeder te modelleren. De simulatie vertoonde een goede overeenkomst voor de hoge vullingsverhouding, d.w.z., na compressie van het

poeder. Een kwantitatieve overeenkomst werd gevonden tussen simulatie en experiment in geval van een vullingsverhouding boven de 70%. Het lagere onverstoorde, niet samengedrukte en luchtig gestapelde poeder leverde een kwalitatieve overeenkomst op in termen van de vorm van de grafiek. Sterkere aantrekking tussen korrels in het model zouden de vorming van fraktale aggregaten mogelijk moeten maken, hetgeen tot een betere overeenkomst zou moeten leiden. Het onderzoek toont aan dat de modellen verbetering behoeven.

References

- [1] R. Andersson, W. G. Bouwman, and I. M. de Schepper. Superfine powders of silica studied with spin-echo small-angle neutron scattering. In *Powders and Grains*, pages 13–15, Stuttgart, Germany, 2005.
- [2] R. Andersson, W. G. Bouwman, S. Luding, and I. M. de Schepper. Stress, strain and bulk microstructure in a cohesive powder. *Physical Review E*, 77(051303):1–8, 2008.
- [3] R. Andersson, W. G. Bouwman, J. Plomp, F. M. Mulder, H. G. Schimmel, and I. M. de Schepper. Structure, anisotropy and fractals in compressed cohesive powders. submitted, 2008.
- [4] T. Aste, M. Saadatfar, A. Sakellariou, and T.J. Senden. Investigating the geometrical structure of disordered sphere packings. *Physica A*, 339:16–23, 2004.
- [5] T. Aste, M. Saadatfar, and T. J Senden. Geometrical structure of disordered sphere packings. *Physical Review E*, 71:061302, 2005.
- [6] A. S Balankin, O Susarrey, and A Bravo. Self-affine nature of the stress-strain behavior of thin fiber networks. *Physical Review E*, 64:066131, 2001.
- [7] J.D. Bernal and J. Mason. Packing of spheres: Co-ordination of randomly packed spheres. *Nature*, 188:910–911, 1960.
- [8] Arjen Bot, Franck P. Duval, and Wim G. Bouwman. Effect of processing on droplet cluster structure in emulsion gels. *Food Hydrocolloids*, 21:844–854, 2007.
- [9] W. G. Bouwman, T. Krouglov, J. Plomp, S. V. Grigoriev, W. H. Kraan, and M. T. Rekveldt. Sesans studies of colloid phase transitions, dairy products and polymer fibers. *Physica B*, 350(1–3):140–146, 2004.
- [10] W. G. Bouwman, J Plomp, V. O. de Haan, W. H. Kraan, A. A. van Well, K Habicht, T Keller, and M. T. Rekveldt. Real-space neutron scattering methods. *Nucl. Instr. Meth. Phys. Res. A*, 586:9–14, 2008.
- [11] W. G. Bouwman and M. T. Rekveldt. Spin-echo small-angle neutron scattering calculations. *Physica B*, 276-278:126–127, 2000.

- [12] W. G. Bouwman, Oktay Uca, Serguei V. Grigoriev, Wicher H. Kraan, Jeroen Plomp, and M. Theo Rekveldt. First quantitative test of spin-echo small-angle neutron scattering. *J. Appl. Phys. A*, 74:S115–S117, 2002.
- [13] Wim G. Bouwman, Timofei V. Krouglov, Jeroen Plomp, and M. Theo Rekveldt. Spin-echo methods for sans and neutron reflectometry. *Physica B*, 357:66–72, 2005.
- [14] R.B. Bracewell. *The Fourier Transform and its Applications*. McGraw-Hill, New York, 2000.
- [15] M.W. Coffey. Self reciprocal fourier functions. *J. Opt. Soc. Am. A*, 11:2453–2455, 1994.
- [16] T. W. Darling, J. A. TenCate, D. W. Brown, B Clausen, and S. C. Vogel. Neutron diffraction study of the contribution of grain contacts to nonlinear stress-strain behavior. *Geophysical Research Letters*, 31(16):L16604, 2004.
- [17] V. O. de Haan, J Plomp, W. G. Bouwman, M Trinker, M. T. Rekveldt, C. P. Duif, E Jericha, H Rauch, and A. A. van Well. Phase-object approximation in small-angle neutron scattering experiments on silicon gratings. *J. Appl. Cryst.*, 40:151–157, 2007.
- [18] P. Debye. Molecular-weight determination by light scattering. *J. Phys. Coll. Chem.*, 51:18–32, 1947.
- [19] P. Debye, H. R. Andersson, and H. Brumberger. Scattering by an inhomogeneous solid. ii. the correlation function and its application. *J. Appl. Phys.*, 28(6):679–683, 1957.
- [20] P. Debye and A. M. Bueche. Scattering by an inhomogeneous solid. *J. Appl. Phys.*, 20:518–525, 1949.
- [21] Wei-Fang Du, L. Wilson, J. Ripmeester, R. Dutrisac, B. Simard, and S. Dénommée. Investigation of the pore structure of As-prepared and purified HiPco single-walled carbon nanotubes by N₂/Ar adsorption—implication for H₂ storage. *Nano Letters*, 2(4):343–346, 2002.
- [22] S.F. Edwards. Theory of powders. *Physica A*, 157(3):1080–1090, June 1989.
- [23] L.A. Feigin and D.I. Svergun. *Structure Analysis by Small-Angle X-Ray and Neutron Scattering*. Plenum Press, 1987.
- [24] R. Gähler, R. Golub, K. Habicht, T. Keller, and J. Felber. Space-time description of neutron spin echo spectrometry. *Physica B*, 229:1–17, 1996.
- [25] R. Garcia-Pelayo. Distribution of distance in the spheroid. *Journal of Physics A*, 38(16):3475–3482, 2005.

- [26] W. Gille. The small-angle scattering correlation function of the cuboid. *J. Appl. Cryst.*, 32:1100–1104, 1999.
- [27] W. Gille. The small-angle scattering correlation function for packages of hard long parallel homogeneous circular cylinders. *Powder Technology*, 149(1):42–50, 2004.
- [28] Otto Glatter. Computation of distance distribution functions and scattering functions of models for small angle scattering experiments. *Acta Physica Austriaca*, 52:243–256, 1980.
- [29] Otto Glatter and O. Kratky. *Small-angle X-ray scattering*. Academic Press, New York, 1982.
- [30] C. Goddeeris, F. Cuppo, H. Reynaers, W. G. Bouwman, and G. Van den Mooter. Light scattering measurements on microemulsions: Estimation of droplet sizes. *Int. J. Pharm.*, 312:187–195, 2006.
- [31] J. Goodisman and N. Coppa. Models for x-ray scattering from random-systems. *Acta Cryst. A*, 37:170–180, 1981.
- [32] H.C. Hamaker. The london van der waals attraction between spherical particles. *Physica*, (4):1058–1072, 1937.
- [33] V. Hauk. *Structural and Residual Stress Analysis by Nondestructive Methods*. Elsevier, Amsterdam, 1997.
- [34] H. Hinrichsen and D.E. Wolf. *The Physics of Granular Media*. Wiley-VCH, Weinheim, 2004.
- [35] M. Hunter, V. Backman, G. Popescu, M Kalashnikov, C. W Boone, A. Wax, V. Gopal, K. Badizadegan, G. D Stoner, and M. S Feld. Tissue self-affinity and polarized light scattering in the born approximation: A new model for precancer detection. *Physical Review Letters*, 97:138102, 2006.
- [36] H. M. Jaeger and S. R. Nagel. Physics of the granular state. *Science*, 255(5051):1523–1531, 1992.
- [37] Erwin Jericha, Matthias Baron, Martin Hainbuchner, Rudolf Loidl, Mario Villa, and Helmut Rauch. Ultra-small-angle neutron scattering studies of artificial lattices. *J. Appl. Cryst.*, 36:778–782, 2003.
- [38] L. P. Kadanoff. Built upon sand: Theoretical ideas inspired by granular flows. *Reviews of Modern Physics*, 71(1):435–444, 1999.
- [39] H. Kaya. On the guinier law for spin-echo small-angle neutron scattering. *J. Appl. Cryst.*, 38:340–345, 2005.

- [40] E. S. Kikkinides and V. N. Burganos. Structural and flow properties of binary media generated by fractional brownian motion models. *Physical Review E*, 59:7185–7194, 1999.
- [41] L. Klimes. Correlation functions of random media. *Pure and Applied Geophysics*, 159:1811–1831, 2002.
- [42] J. B. Knight, C. G. Fandrich, C. N. Lau, H. M. Jaeger, and S. R. Nagel. Density relaxation in a vibrated granular material. *Physical Review E*, 51:3957 – 3963, 1995.
- [43] M.M. Kohonen, D. Geromichalos, M. Scheel, C. Schier, and S. Herminghaus. On capillary bridges in wet granular materials. *Physica A*, 339(1-2):7–15, 2004.
- [44] T. Krouglov, W. G. Bouwman, J. Plomp, M. T. Rekveldt, G. J. Vroege, A. V. Petukhov, and D. M. E. Thies-Weesie. Structural transitions of hard-sphere colloids studied by spin-echo small-angle neutron scattering. *J. Appl. Cryst.*, 36(6):1417–1423, Dec 2003.
- [45] T. Krouglov, I. M. de Schepper, W. G. Bouwman, and M. T. Rekveldt. Real-space interpretation of spin-echo small-angle neutron scattering. *J. Appl. Cryst.*, 36(1):117–124, 2003.
- [46] T. Krouglov. Spin-echo small-angle neutron scattering for dense systems of spheres. *J. Appl. Cryst.*, 38:721–726, 2005.
- [47] S. Luding. Anisotropy in cohesive, frictional granular media. *Journal of Physics: Condensed Matter*, 17:2623–2640, 2005.
- [48] S. Luding. Structure and cluster formation in granular media. *Pramana-Journal of Physics*, 64(6):893–902, 2005.
- [49] S. Luding. Cohesive, frictional powders: contact models for tension. *Granular Matter*, 10(4):235–246, 2008.
- [50] T.S. Majmudar and R.P. Behringer. Contact force measurements and stress-induced anisotropy in granular materials. *Nature*, 435(7045):1079–1082, 2005.
- [51] Benoit B. Mandelbrot. *The Fractal Geometry of Nature*. W.H. Freeman and Company, San Fransisco, 1982.
- [52] P. Meakin, I Majid, S. Havlin, and H. E. Stanley. Topological properties of diffusion limited aggregation and cluster cluster aggregation. *J. Phys. A*, 17(18):L975–L981, 1984.
- [53] Y. B. Melnichenko and G. D. Wignall. Small-angle neutron scattering in materials science: Recent practical applications. *J. Appl. Phys.*, 102(021101), 2007.

- [54] F. Mezei. Neutron spin echo: A new concept in polarised thermal neutron techniques. *Z. Physik*, 255:146, 1972.
- [55] D.M. Mueth, G.F. Debregeas, G.S. Karczmar, P.J. Eng, S.R. Nagel, and H.M. Jaeger. Signatures of granular microstructure in dense shear flows. *Nature*, 406:385–389, 2000.
- [56] E.R. Nowak, J.B. Knight, E Ben-Naim, H.M. Jaeger, and S.R. Nagel. Density fluctuations in vibrated granular materials. *Physical Review E*, 57(2):1971–1982, February 1998.
- [57] E.R. Nowak, J.B. Knight, M.L. Povinelli, H.M. Jaeger, and S.R. Nagel. Reversibility and irreversibility in the packing of vibrated granular material. *Powder Technology*, 94(1):79–83, November 1997.
- [58] J. Skov Pedersen. Analysis of small-angle scattering data from colloids and polymer solutions: modeling and least squares fitting. *Adv. coll. int. sci.*, 70:171–210, 1997.
- [59] J. K. Percus and G. J. Yevick. Analysis of classical statistical mechanics by means of collective coordinates. *Physical Review*, 110(1):1–13, 1958.
- [60] J. Plomp, V.O. de Haan, R.M. Dalgliesh, S. Langridge, and A.A. van Well. Neutron spin-echo labelling at offspec, an isis second target station project. *Thin solid films*, 515:5732–5735, 2007.
- [61] T. Pöschel and T. Schwager. *Computational Granular Dynamics*. Springer, Berlin, 2005.
- [62] R. Pynn, M. R. Fitzsimmons, H. Fritzsche, and M. Gierlings J. Major A. Jason. Neutron spin echo scattering angle measurement (sesame). *Rev. Sci. Instr.*, 76:053902, 2005.
- [63] M. T. Rekveldt. Novel SANS instrument using neutron spin echo. *Nucl. Instr. Meth. Phys. Res. B*, 114:366–370, 1996.
- [64] M. T. Rekveldt. Neutron reflectometry and sans by neutron spin echo. *Physica B*, 234:1135–1137, Jun 1997.
- [65] M. T. Rekveldt, Wim G. Bouwman, Wicher H. Kraan, Oktay Uca, Serguei Grigoriev, S.Habicht, and T. Keller. *Neutron Spin Echo*, volume 601 of *Lecture Notes in Physics*, chapter Elastic neutron scattering measurements using Larmor precession of polarised neutrons, pages 87–99. Springer, Berlin, 2003. Ed. by F. Mezei, C. Pappas and T. Gutberlet.
- [66] M.T. Rekveldt, Jeroen Plomp, Wim G. Bouwman, Wicher H. Kraan, Serguei Grigoriev, and Menno Blaauw. Larmor precession applications: magnetised foils as spin flippers in spin-echo sans with varying wavelength. *Rev. Sci. Ins.*, 76:033901, 2005.

- [67] P. Richard, P. Philippe, F. Barbe, S. Bourlès, X. Thibault, and D. Bideau. Analysis by x-ray microtomography of a granular packing undergoing compaction. *Physical Review E*, 68:020301R, 2003.
- [68] J. Schelten and W. Schmatz. Multiple-scattering treatment for small-angle scattering problems. *J. Appl. Cryst.*, 13:385–390, 1980.
- [69] P. W. Schmidt. Small-angle scattering studies of disordered, porous and fractal systems. *J. Appl. Cryst.*, 24:414–435, 1991.
- [70] A.J. Sederman, P. Alexander, and L.F. Gladden. Structure of packed beds probed by magnetic resonance imaging. *Powder Technology*, 117:255–269, 2001.
- [71] G. T Seidler, G. Martinez, L. H Seeley, K. H Kim, E. A Behne, S. Zaranek, B. D Chapman, S. M Heald, and D. L Brewé. Granule-by-granule reconstruction of a sandpile from x-ray microtomography data. *Physical Review E*, 62:8175 – 8181, 2000.
- [72] S. K. Sinha. Scattering from fractal structures. *Physica D*, 38:310–314, 1989.
- [73] *Neutron News*. 3(3):29–37, 1992.
- [74] E Thiele. Equation of state for hard spheres. *J. Chem. Phys.*, 39(2):474–479, 1963.
- [75] M. Toiya, J. Stambaugh, and W. Losert. Transient and oscillatory granular shear flow. *Physical Review Letters*, 93(8):088001, 2004.
- [76] J. Tomas. Fundamentals of cohesive powder consolidation and flow. *Granular Matter*, 6:75–86, 2004.
- [77] J Török, S Krishnamurthy, J Kertész, and S Roux. Shearing of loose granular materials: A statistical mesoscopic model. *Physical Review E*, 67:021303, 2003.
- [78] M. Trinker, E. Jericha, W. G. Bouwman, R. Loidl, and H. Rauch. Analysis of artificial silicon microstructures by ultra-small-angle and spin-echo small-angle neutron scattering. *Nucl. Instr. Meth. Phys. Res. A*, 579:1081–1089, 2007.
- [79] H. Tromp and W. G. Bouwman. A novel application of neutron scattering on dairy products. *Food Hydrocolloids*, 21:154–158, 2007.
- [80] O. Uca, W.G. Bouwman, and M.T Rekveldt. Model calculations for the spin-echo small-angle neutron-scattering correlation function. *J. Appl. Cryst.*, 36:109–116, 2003.
- [81] B. Vigolo, A. Péénicaud, C. Coulon, C. Sauder, R. Paillet, C. Journet, P. Bernier, and P. Poulin. Macroscopic fibers and ribbons of oriented carbon nanotubes. *Science*, 290:1331–1334, 2000.

- [82] J. Visser. Van der waals and other cohesive forces affecting powder fluidization. *Powder Technology*, 58(1):1–10, 1989.
- [83] J Šaroun. Evaluation of double-crystal sans data influenced by multiple scattering. *J. Appl. Cryst.*, 33:824–828, 2000.
- [84] P. Z Wong and Q. Z Cao. Correlation-function and structure factor for a mass fractal bounded by a surface fractal. *Physical Review B*, 45(14):7627–7632, 1992.
- [85] M Zaiser, F. M. Grassett, V Koutsos, , and E. C. Aifantis. Self-affine surface morphology of plastically deformed metals. *Physical Review Letters*, 93(19):195507, 2004.

Acknowledgements

My final words are words of gratitude. Countless people made this thesis work possible in countless ways. My *handledare*¹, Wim Bouwman, did not only lend-his-hand (as the Swedish word for supervisor suggest), but he shaped my professional character and made me become a scientist. This work would never have been completed without Wim. My promotor, Ignatz de Schepper, always had time for a discussion. Discussions that always increased my understanding of physics and mathematics, and indeed enabling a thesis about physics to be written by a chemist. Stefan Luding was the expert that we all leaned on. Stefan, thanks to your warm friendship and intellectual support this thesis is now finished. I was hired by Menno Blaauw, who also initiated the entire project and raised the funds. Thank you, Menno, for believing in me, and giving me the opportunity to come to the Netherlands for, perhaps, the most challenging work one can take on. The friendship and tireless support, both technical and intellectual, that I got from Chris Duif makes me most grateful.

My work was essentially experimental. There were numerous technical and design challenges that needed to be solved. The solutions saw the light much thanks to: Piet van der Ende, Rene Gommers with staff at the design office, René den Oudsten with staff at the center for mechanical development and, finally, Jeroen Plomp for help, lessons and inspiration in doing my own designing and construction work. The SESANS instrument would not exist without the brainwork of Theo Rekveldt, nor would it work without the neutron precession devices thought-up by Wicher Kraan. Niels van Dijk, thank you for all the input and interest you showed in this work.

Working as a Ph.D. candidate is often frustrating and sometimes a sorrow task. It is due to the friendship of friends, fellow Ph.D. candidates and colleagues that I came through, and also had a lot of fun. Leon van Heijkamp, my office mate, is a great friend and through our many discussions Leon also made a great contribution to this thesis.

To My father Håkan, my sister Anna, my brother in law Sebastian, niece Emelie and nephew Hugo, and of course to my lovely Joselia –I express my deepest gratitude for all generosity and love. I dedicate this thesis to my late mother Inga-Lill Andersson.

¹Swedish for a person that helps someone during studies/work. English translation: supervisor.

About the author

Robert Andersson was born on the 11th of August 1976 in Askim, Sweden. After primary school and gymnasium he studied Chemical Engineering at Chalmers University of Technology (2000), which was finalised in a Magisterexamen (M.Sc.) in Chemistry at the University of Gothenburg (2003). The master thesis was titled: *Polymer-induced depletion interactions in model microemulsions*². The switch from colloids to powders, another soft matter, was natural, and he decided to pursue a Ph.D. in physics by studying powders with spin-echo small-angle neutron scattering at the Reactor Institute Delft at Delft University of Technology, the Netherlands. The result of this research is presented in the thesis. Beginning from August 2008, Robert will continue his professional career as a Management Consultant at Accenture in Amsterdam, where he will work within the chemicals practice.

²M. Zackrisson, R. Andersson and J. Bergenholtz, *Depletion Interactions in Model Microemulsions*, *Langmuir*, 20 (8), 3080 -3089, 2004

